UNIVERSIDAD DE EXTREMADURA

TESIS DOCTORAL

Métodos paralelos áltamente escalables para modelado electromagnético de problemas a gran escala

Víctor Francisco Martín Martínez

Programa de Doctorado Interuniversitario en Tecnología Aeroespacial:
Ingenierías Electromagnética, Electrónica, Informática y Mecánica

Conformidad del director y codirector:

Fdo. Dr. D. José Manuel Taboada Varela

Fdo. Dr. D. Luis Landesa Porras

Esta tesis cuenta con la autorización del director/a y coodirector/a de la misma y de la Comisión Académica del programa. Dichas autorizaciones constan en el Servicio de la Escuela Internacional de Doctorado de la Universidad de Extremadura

2022

UNIVERSIDAD DE EXTREMADURA

TESIS DOCTORAL

Métodos paralelos áltamente escalables para modelado electromagnético de problemas a gran escala

(Parallel multisolver methods for very long-scale electromagnetic modelling)

Víctor Francisco Martín Martínez

Programa de Doctorado Interuniversitario en Tecnología Aeroespacial:
Ingenierías Electromagnética, Electrónica, Informática y Mecánica

Memoria para optar al Grado de Doctor con Mención Internacional

2022

A mi abuelo.

*"There is a driving force more powerful tham
steam, electricity and atomic energy: the will."*

- Albert Einstein -

Agradecimientos institucionales

- Ministerio de Ciencia, Innovación y Universidades, proyectos FPU00550/17 y EST21/00590.
- Ministerio de Economía y Competitividad y Fondos FEDER, proyectos MAT2014-58201-C2-1-R, MAT2014-58201-C2-2-R, TEC2017-85376-C2-X-R.
- Ministerio de Ciencia e Innovación, proyecto PID2020-116627RB-C2X.
- Junta de Extremadura y fondos FEDER, proyectos IB13185, IB18073, GR15052, GR18055 y GR21072.

GOBIERNO
DE ESPANA

MINISTERIO
DE ECONOMIA
Y COMPETITIVIDAD

GOBIERNO
DE ESPAÑA

MINISTERIO
DE CIENCIA, INNOVACIÓN
Y UNIVERSIDADES

European Union
European Regional
Development Fund

JUNTA DE EXTREMADURA
Consejería de Economía e Infraestructuras

Resumen

Los métodos de ecuación integral de superficie (SIE) basados en el método de momentos (MoM) se han convertido en una herramienta indispensable en electromagnetismo computacional (CEM) en la fase de diseño de una amplia gama de aplicaciones. El uso de este tipo de herramientas puede suponer un reto en aplicaciones de vanguardia como la compatibilidad electromagnética (EMC) o la nanotecnología en aplicaciones plasmónicas, donde el elevado tamaño de los sistemas y la problemática multiescala, presente en el nivel de detalle geométrico requerido en estas aplicaciones, y la problemática multifísica, en el sentido de que se combinan diversos materiales con respuestas electromagnética muy diferentes, complica sobremanera la obtención de resultados precisos en tiempos razonables. Las técnicas de precondicionamiento basadas en el método de descomposición de dominios (DDM) se presentan como una de las mejores alternativas para hacer frente al mal condicionamiento que domina estos sistemas.

En este contexto, esta tesis doctoral combina los últimos avances y explora nuevas soluciones en algoritmos SIE, hardware informático y habilidades de paralelización para abordar la solución eficiente y robusta de problemas extremadamente grandes y mal condicionados. En primer lugar, se ha desarrollado e integrado un método de descomposición de dominios altamente eficiente con las tecnologías del grupo de investigación que avala la tesis. A continuación, se han incorporado los nuevos avances en algoritmos SIE para mejorar la versatilidad del método propuesto, proporcionando un verdadero conjunto de herramientas multipropósito para la simulación electromagnética de problemas extremadamente complejos con aplicaciones en la vida real.

Abstract

Surface integral equation (SIE) methods based on the method of moments (MoM) have emerged as a powerful and indispensable tool in computational electromagnetics (CEM) for the simulation and engineering of a wide range of applications. The use of this type of simulation tools can be critical in cutting-edge applications such as EMC engineering or the field of nanoplasmonics, where extremely large-scale problems that also suffer from problematic multiscale and multiphysics issues that complicate the accurate analysis of challenging systems. Schwarz preconditioners based on the domain decomposition method (DDM) are presented as one of the best alternatives to deal with the ill-conditioning of such systems.

In this context, this doctoral thesis combines the latest breakthroughs and devises new methodologies in SIE algorithms, computing hardware, and parallelization skills to address the efficient and robust solution of the extremely large and ill-conditioned problems. First, a highly efficient domain decomposition method is developed and integrated with the advanced SIE technologies of the research group that endorses this thesis. Next, novel SIE advances in non-conformal discretization and preconditioning of deep multiscale and multiphysics problems are incorporated to improve the versatility of the proposed methods, providing a truly multipurpose methodology for the electromagnetic simulation of extremely challenging problems with real-life application.

List of publications

International journals

[1] J. Kumar, H. Eraña, E. López-Martínez, N. Claes, **V. F. Martín**, D. M. Solís, S. Bals, A. L. Cortajarena, J. Castilla and L. M. Liz-Marzán, “Detection of amyloid fibrils in Parkinson’s disease using plasmonic chirality”,*Proceedings of the National Academy of Sciences*, vol. 115, pp. 3225-3230, 2018.
DOI: 10.1073/pnas.1721690115.

[2] D. M. Solís, **V. F. Martín**, M. G. Araújo, D. Larios, F. Obelleiro and J. M. Taboada, “Accurate EMC Engineering on Realistic Platforms Using an Integral Equation Domain Decomposition Approach”,*IEEE Transactions on Antennas and Propagation*, vol. 68, no. 4, pp. 3002-3015, April 2020, DOI: 10.1109/TAP.2019.2950862.

[3] **V. F. Martín**, D. Larios, D. M. Solís, J. M. Taboada, L. Landesa and F. Obelleiro, “Tear-and-Interconnect Domain Decomposition Scheme for Solving Multiscale Composite Penetrable Objects”,*IEEE Access*, vol. 8, pp. 107345-107352, 2020, DOI: 10.1109/ACCESS.2020.3000650.

[4] D. García-Lojo, S. Gómez-Graña, **V. F. Martín**, D. M. Solís, J. M. Taboada, J. Pérez-Juste and I. Pastoriza-Santos, “Integrating Plasmonic Supercrystals in Microfluidics for Ultrasensitive, Label-Free, and Selective Surface-Enhanced Raman Spectroscopy Detection”,*ACS Applied Materials & Interfaces*, vol. 12, no. 41, pp. 46557-46564, 2020, DOI: 10.1021/acsami.0c13940.

[5] S. Gullace, V. Montes-García, **V. F. Martín**, D. Larios, V. Girelli-Consolaro, F. Obelleiro, G. Calogero, S. Casalini and P. Samori, “Universal Fabrication of Highly Efficient Plasmonic Thin-Films for Label-Free SERS Detection”,*Small*, vol. 17, no. 33, pp. 2100755, 2021, DOI: 10.1002/smll.202100755.

[6] **V. F. Martín**, L. Landesa, F. Obelleiro and J. M. Taboada, “A Discontinuous Galerkin Combined Field Integral Equation Formulation for Electromagnetic Modeling of Piecewise Homogeneous Objects of Arbitrary Shape”,*IEEE Transactions on Antennas and Propagation*, vol. 70, no. 1, pp. 487-498, Jan 2022, DOI: 10.1109/TAP.2021.3098549.

[7] D. M. Solís, **V. F. Martín**, J. M. Taboada and F. Vipiana, “Multiresolution Preconditioners for Solving Realistic Multi-Scale Complex Problems”,*IEEE Access*, vol. 10, pp. 22038-22048, 2022, DOI: 10.1109/ACCESS.2022.3153034.

Submissions pending publication

[1] **V. F. Martín**, J. M. Taboada and F. Vipiana, “A Multi-Resolution Preconditioner for Non-Conformal Meshes in the MoM Solution of Large Multi-Scale Structures”, submitted to *IEEE Transactions on Antennas and Propagation.*

[2] **V. F. Martín**, M. Gómez-Araújo, D. M. Solís, L. Landesa, F. Obelleiro and J. M. Taboada, “A Discontinuous Galerkin Integral Equation Approach for Electromagnetic Modeling of Realistic and Complex Radiating Systems”, submitted to *IEEE Transactions on Antennas and Propagation.*

[3] **V. F. Martín**, D. M. Solís, D. Jericó, L. Landesa, F. Obelleiro and J. M. Taboada, “Discontinuous Galerkin Integral Equation Method for Light Scattering from Complex Nanoparticle Assemblies”, submitted to *Optics Express.*

National and international conferences

[1] **V. F. Martín**, D. Larios, J. M. Taboada, L. Landesa and D. M. Solís, "Fast Solution of Large Multi-Scale Electromagnetic Problems with MLFMA and Schwarz Domain Decomposition preconditioners," *XXXII Simposium Nacional de la Unión Científica Internacional de Radio (URSI 2017)*, Cartagena (Spain), 6-8 September, 2017.

[2] D. Larios, **V. F. Martín**, Y. Campos-Roca and J. M. Taboada, "Design of UWB Antennas for Communications in the VHF and UHF Frequency Bands," *XXXII Simposium Nacional de la Unión Científica Internacional de Radio (URSI 2017)*, Cartagena (Spain), 6-8 September, 2017.

[3] J. M. Taboada, D. M. Solís, **V. F. Martín**, D. Larios, F. Obelleiro and J. L. Rodríguez, "Surface Integral Equation-Domain Decomposition Scheme for Solving Multi-Scale Radiation and Scattering Problems," *International Conference on Electromagnetics in Advanced Applications (ICEAA 2017)*, Verona (Italy), 11-15 September, 2017. **Invited talk**.

[4] D. M. Solís, **V. F. Martín**, D. Larios, J. M. Taboada, J. L. Rodríguez and F. Obelleiro, "DDM-Assisted Analysis of Large Scale Radiating Structures," *XII European Conference on Antennas and Propagation (EuCAP 2018)*, London (United Kingdom), 9-13 April, 2018. **Invited talk**.

[5] D. Larios, **V. F. Martín**, F. Obelleiro, J. L. Rodríguez and J. M. Taboada, "Topside Electromagnetic Compatibility (EMC) of Communication Systems in the V/UHF Frequency Band," *XXXIII Simposium Nacional de la Unión Científica Internacional de Radio (URSI 2018)*, Granada (Spain), 5-7 September, 2018.

[6] **V. F. Martín**, D. Larios, J. M. Taboada, L. Landesa, F. Obelleiro and D. M. Solís, "Aceleración de Problemas Electromagnéticos Multiescala mediante el Método de Descomposición de Dominios," *XXXIII Simposium Nacional de la Unión Científica Internacional de Radio (URSI 2018)*, Granada (Spain), 5-7 September, 2018.

[7] **V. F. Martín**, D. M. Solís, D. Larios, J. M. Taboada, L. Landesa, J. L. Rodríguez and F. Obelleiro, "DDM-Assisted Analysis of Large Scale Composite Problems," *XIII European Conference on Antennas and Propagation (EuCAP 2019)*, Krakow (Poland), 31 March-5 April, 2019. **Invited talk**.

[8] **V. F. Martín**, D. M. Solís, D. Larios, J. M. Taboada, J. L. Rodríguez and F. Obelleiro, "Solving Realistic Multiscale and Composite Problems using an Integral Equation Domain Decomposition Approach," *2019 IEEE International Symposium on Antennas and Propagation and USNC-URSI Radio Science Meeting (AP-S/URSI 2019)*, Atlanta (USA), 7-12 July, 2019.

[9] **V. F. Martín**, J. M. Taboada, D. M. Solís, D. Larios and Fernando Obelleiro, “Tear and Interconnect Domain Decomposition Analysis of Piecewise Penetrable Structures,” *International Conference on Electromagnetics in Advanced Applications (ICEAA 2019)*, Granada (Spain), 9-13 September, 2019. **Invited talk**.

[10] J. M. Taboada, D. M. Solís, **V. F. Martín**, D. Larios, L. Landesa, J. L. Rodríguez and Fernando Obelleiro, “Fast Maxwell’s Simulation of New Real-World Problems at the Nanoscale,” *International Conference on Electromagnetics in Advanced Applications (ICEAA 2019)*, Granada (Spain), 9-13 September, 2019. **Invited talk**.

[11] D. Larios, M. Gómez-Araújo, D. M. Solís, **V. F. Martín**, J. M. Taboada and Fernando Obelleiro, “Electromagnetic Analysis and Design of Radiating Systems on Board Real Platforms Via Domain Decomposition Method,” *International Conference on Electromagnetics in Advanced Applications (ICEAA 2019)*, Granada (Spain), 9-13 September, 2019. **Invited talk**.

[12] **V. F. Martín**, D. M. Solís, D. Larios, J. M. Taboada, L. Landesa and F. Obelleiro, “Toward extremely scalable IE-DDM for distributed computing,” *XIV European Conference on Antennas and Propagation (EuCAP 2020)*, Copenhaguen (Danmark), Virtual, 15-20 March, 2020. **Invited talk**.

[13] **V. F. Martín**, D. Larios, J. M. Taboada, L. Landesa and F. Obelleiro, “DG-JMCFIE Formulation for the Simulation of Composite Objects,” *International Applied Computational Electromagnetics Society Symposium (ACES 2021)*, Virtual, 1-5 August, 2021. **Invited talk**.

[14] **V. F. Martín**, D. Larios, D. M. Solís, L. Landesa, J. L. Rodríguez, Fernando Obelleiro and J. M. Taboada, “Distributed Hybrid MPI/OpenMP IE-DDM for Electromagnetic Modeling of Large Platforms,” *International Conference on Electromagnetics in Advanced Applications (ICEAA 2021)*, Hawai (USA), Virtual, 9-13 August, 2021. **Invited talk**.

[15] **V. F. Martín**, D. Larios, D. M. Solís, L. Landesa, J. L. Rodríguez, F. Obelleiro and J. M. Taboada, “An interior penalty DG-JMCFIE Formulation for Piecewise Homogeneous Objects with multimaterial junctions,” *XXXVI Simposium Nacional de la Unión Científica Internacional de Radio (URSI 2021)*, Vigo (Spain), Virtual, 20-24 September, 2021.

[16] J. M. Taboada, **V. F. Martín**, D. M. Solís, D. Larios, L. Landesa and F. Obelleiro, “Fast Integral-Equation Simulation of Plasmonic and Photonic Problems at the Nanoscale,” *XXXIV General Assembly and Scientific Symposium (GASS) of the International Union of Radio Science (Union Radio Scientifique Internationale-URSI)*, Rome (Italy), 28 August-4 September, 2021. **Invited talk**.

[17] F. Vipiana, A. Serna, J. Tobon, **V. F. Martín**, Z. Peng, "A Local Mesh Refinement Scheme for Multi-scale Problems via Huygens' Surfaces," *XXXIV General Assembly and Scientific Symposium (GASS) of the International Union of Radio Science (Union Radio Scientifique Internationale-URSI)*, Rome (Italy), 28 August-4 September, 2021. **Invited talk**.

[18] **V. F. Martín**, D. M. Solís, D. Larios, J. M. Taboada, J. L. Rodríguez and F. Obelleiro, "DG-JMCFIE Formulation for Composite Multimaterial Objects," *2021 IEEE International Symposium on Antennas and Propagation and USNC-URSI Radio Science Meeting (AP-S/URSI 2021)*, Singapore (Singapore), 4-10 December, 2021.

[19] A. Serna, J. Tobon, **V. F. Martín**, Z. Peng, F. Vipiana, "Applying Huygen's Equivalence Surfaces in the Local Mesh Refinement of Multiscale Problems," *2021 IEEE International Symposium on Antennas and Propagation and USNC-URSI Radio Science Meeting (AP-S/URSI 2021)*, Singapore (Singapore), 4-10 December, 2021.

[20] **V. F. Martín**, D. Larios, L. Landesa, F. Obelleiro and J. M. Taboada, "Discontinuous Galerkin JMCFIE Formulation for Solving Multimaterial Composite Objects," *XVI European Conference on Antennas and Propagation (EuCAP 2022)*, Madrid (Spain), 27 March-1 April, 2022. **Invited talk**.

[21] **V. F. Martín**, D. Larios, J. M. Taboada, L. Landesa and F. Obelleiro, "DG-JMCFIE-EFIE Formulation for Multi-material Complex Radiation Problems," *XIV Iberian Meeting on Computational Electromagnetics (EIEC 2022)*, Nuria (Spain), 24-27 May, 2022. **Invited talk**.

[22] **V. F. Martín**, D. Larios, J. M. Taboada, L. Landesa and F. Obelleiro, "Discontinuous Galerkin JMCFIE-EFIE Formulation for Solving Multi-material Complex Antennas," *III Atlantic, Asia-Pacific Radio Sscience Conference (AT-AP-RASC 2022)*, Gran Canaria (Spain), 29 May-3 June, 2022. **Invited talk**.

Acronyms

CAD computer-aided design. 4

CEM computational electromagnetics. 1

CFIE combined field integral equation. 84

CSR compressed sparse row. 43

DD domain decomposition. 21

DDM domain decomposition method. 4

DG Discontinuous Galerkin. 5

DP diagonal preconditioner. 40

EFIE electric field integral equation. 10

EMC/EMI electromagnetic compatibility and interference. 3

FDTD finite difference in the time domain. 1

FEM finite element method. 1

FFT fast Fourier transform. 17

FMM fast multipole method. 16

GMRES generalized minimal residual method. 26

GPU graphics processing unit. 111

gRWG generalized Rao-Wilton-Glisson. 38

h-RWG half Rao-Wilton-Glisson. 46

HPC high performance computing. 26

ILU incomplete lower unitriangular upper triangular preconditioner. 3

IPO iterative physical optics. 111

JMCFIE electric and magnetic combined field integral equation. 13

LSPR localized surface plasmon resonance. 97

MB-MR multibranch-multiresolution. 63

MB-RWG multibranch Rao-Wilton-Glisson. 71

MFIE magnetic field integral equation. 10

MKL Intel Math Kernel Library. 41

MLFMA multilevel fast multipole method. 2

MLFMA-FFT multilevel fast multipole method-fast Fourier transform. 5

MoM method of moments. 3

MPI message passing interface. 29

MR Multiresolution. 71

MVP matrix-vector-product. 25

NR nanorod. 97

NUMA non uniform memory architecture. 29

PARDISO parallel sparse direct and multi-recursive iterative linear solver. 43

PEC perfect electric conductor. 22

PS polystyrene. 97

RAM random access memory. 29

RCS radar cross section. 32

RHS right hand side. 99

RWG Rao-Wilton-Glisson. 47

SERS surface enhanced Raman spectroscopy. 102

SIE Surface Integral Equation. 13

SpMVP sparse matrix-vector-product. 41

SVD Singular Value Decomposition. 68

UHF Ultra High Frequency. 77

VHF Very High Frequency. 81

Contents

List of Tables

List of Figures

Chapter 1

Introduction

Contenido

1.1 Motivations of the thesis

Surface integral equation (SIE) methods based on the method of moments (MoM) [1] have emerged as a powerful and indispensable tool in computational electromagnetics (CEM) for the simulation and engineering of a wide range of applications [2–6], from advanced antenna design [7–9], enhancement of antennas by plasmon resonances [10–12], electromagnetic compatibility and interference (EMC/EMI) [13], radar cross section (RCS) [14] and stealth technologies [15, 16] to integrated circuits [17].

SIE methods provide significant advantages over volumetric approaches such as the finite difference in the time domain (FDTD) [18] or the frequency domain finite element methods (FEMs) [19,20]. Although the latter benefit from relatively simple parameterizations of the electromagnetic fields and are much easier to implement, the application of SIE methods to Maxwell's equations raises much smaller solution subspaces, since they only require the parameterization of the two-dimensional (2D) boundary surfaces and interfaces, rather than the three-dimensional (3D) structure and embedding space. They also eliminate the requirement for absorbing boundary conditions to terminate open problems. These advantages, combined with outstanding accuracy and versatility, make SIE-MoM a preferred choice when it comes to solving many real-life applications dealing with complex large-scale structures.

The use of this type of simulation tools can be critical in some of the applications mentioned. Specially, it is critical to effectively address the design and management of the EMC and EMI issues (commonly termed EMC engineering) as early as possible in the platform design stage, trying to assure the overall system performance. The EMC engineering entails the need of solving electrically large EM radiation problems, which are challenging problems.

Another really challenging cutting-edge field that has ignited intense research in recent years is nanotechnology. Among the many multidisciplinary challenges posed by this revolutionary science, the unprecedented ability of subwavelength confinement, enhancement, and spatio-temporal control of light and electron beams in the vicinity of metal/dielectric interfaces have stimulated an intense research in the field of plasmonics. SIE methods have been extended to the field of nanoplasmonics [21–27]. Nanoplasmonics is a flourishing branch of optical engineering concerned with the study of the interaction of light with sub-wavelength metallic nanoparticles or devices at the nanometer scale. It has numerous scientific and technological applications, e.g. in telecommunication [28], energy production [29], biomedicine and biosensing [30, 31], among many others [32–38]. In the last years, nanoplasmonics has become a very active research topic, increasingly demanding numerical simulation to theoretically explain and/or provide guidance to experimental studies. The light scattering from plasmonic nanoparticles is well described by classical electrodynamic equations. Until recently, the dominant simulation techniques in nanoplasmonics were those based on volumetric methods, partly because of the availability of commercial software such as COMSOL `http://www.comsol.com/`.

Nevertheless, SIE Maxwell solvers bring important advantages when it comes to large-scale systems and nanoparticle assemblies spanning a large number of wavelengths. Although these methods pose dense matrices that may be too large for direct solution in the case of large problems, iterative fast solvers such as the multilevel fast multipole algorithm (MLFMA) or the parallel MLFMA-fast Fourier transform (MLFMA-FFT) are available [39–44].

However, despite the great advances achieved up to now, there are still a lot of challenges that need to be faced in order to be able to simulate and design cutting-edge real-life applications. The systems needed to adequately model the behaviour of these plasmonic particles results in extremely large-scale problems that further suffer from problematic multi-scale issues associated to the detailed description of the geometry or even from the multiphysics resulting from the combination of drastically different materials. These issues yield extremely ill-conditioned matrix equations, impinging a dramatic deterioration of convergence and performance of the SIE solution, which often makes the problem even impossible to be solved [45–53].

In previous cases, where the ill-conditioning of the system dominates the simulation scenario, the preconditioning techniques can be applied to improve iterative convergence. Those physics-based that use quasi-Helmholtz decompositions [54–56] or the Calderon identities [57–61] have proven good success, but those based on algebraic techniques, such as the incomplete lower unitriangular upper triangular (ILU), or block-Jacobi preconditioners [62–64] also improve considerably the convergence. But one of the best alternative is the use of Schwarz preconditioners based on the domain decomposition method (DDM) [65–70], which can be categorized as an algebraic preconditioner but also as a physic-based preconditioner, since it allows to separate the physics of the different subsystems that make up the whole problem to adequately solve each one using the appropriate method based on its properties.

Additionally, the mesh generation and computer-aided design (CAD) processes required to correctly define the problem became really complicated, especially in the case of using domain decomposition techniques, challenging due to the complexity of the partitions and connections in the geometry. An important advance that has recently been brought to the SIE based methodology is the technique known as Discontinuous Galerkin (DG),that allow different parts of a larger, more complex assembly to be modeled and meshed independently and assembled back to form a whole connected body, without caring about mesh conforming or slight miss-placement at the tear contours. Other SIE non-conforming scheme alternative to DG is the very recently presented Multibranch Rao-Wilton-Glisson (MB-RWG) [71]. The MB-RWG basis functions can be easily integrated into existing MoM codes without need of penalty terms, additional volumetric integrals or artificial surfaces. They are very convenient for h-refinement techniques and are div-conforming basis functions, allowing the construction of solenoidal basis as linear combination of them.

In this context, this thesis combine the latest breakthroughs in SIE algorithms, computing hardware, and parallelization skills to address the efficient and robust solution of the extremely large and ill-conditioned problems rendered by real-life EMC/EMI and nanotechnology applications, by first developing a high efficient multipurpose domain decomposition framework, which is the cornerstone of the method and subsequent developments. Among the different possibilities, the additive Schwarz domain decomposition preconditioner is integrated with the advanced SIE technologies of the research group that endorses the thesis. Next, novel SIE advances are devised for the use of non-conformal discretizations and preconditioning in deep multiscale and multiphysics problems. A collection of extremely challenging problems in EMC/EMI and nanoplasmonics with real life applications is also presented at the end of this memory to illustrate the advanced capabilities of the methodology developed in this thesis.

1.2 Objectives

The main objectives of this work are detailed below.

- Development of a general-purpose DDM implementation for composite multi-material homogeneous problems.
- Efficient implementation of shared-memory parallelism using OpenMP at the local solvers and mixed-memory MPI/OpenMP parallelism at the mutual coupling interaction.
- Development of non-conformal MoM implementations of the SIE methods based on Discontinuous Galerking (DG) and multibranch-RWG basis functions (MB-RWG) to improve the CAD processes required in DDM.
- Development of high scalability preconditioners capable of solving complex multi-scale problems including non-conformal meshes to improve the convergence of the iterative local solvers.
- Application of the developed algorithms to the solution of real-life multi-scale systems in EMC/EMI and plasmonics, focusing especially on surface enhanced Raman spectroscopy (SERS) applications.

1.3 Contribution of the thesis

The main contribution of this thesis is the development of general-purpose methodologies to perform the electromagnetic analysis of large-scale complex problems including deeply multi-scale and multi-physics features with application in real-life systems in plasmonics and EMC/EMI engeneering within the SIE-MoM developed by the research group where this work was carried out. This can be described through the following lines:

- Development of a truly multisolver overlapping Schwarz domain decomposition method with a library module of solvers for composite multi-material homogeneous problems using the electric and magnetic combined field integral equation (JMCFIE) formulation. The proposed algorithm uses the tear-and-interconnect transmission conditions to solve local open penetrable problems independently without need of artificial surfaces to make the problem closed. The implementation is designed to allow the easy inclusion of new methodologies in the local solver or mutual coupling, and can benefit from the existence of a large number of geometric repetitions and symmetry patterns.

- Efficient parallelization of the DDM implementation delivered in the previous point by applying a two-stage parallelization strategy: shared memory OpenMP parallelization of the local solvers to be applied inside each subdomain; and hybrid memory MPI/OpenMP parallelization of the DDM framework, including fast subdomain mutual couplings and the global Krylov iterative solver. This strategy enables unprecedented efficiency and flexibility in distributing the DDM workload among large mixed-memory computers made up of a number of distributed shared-memory nodes with large numbers of parallel processors and cores inside. The second stage of parallelization includes an extension of the MLFMA-FFT to achieve a distributed global coupling calculation in both domains and materials. Furthermore, the proposed algorithm is able to take advantage of the global contributions contained in the local matrix of MoM domains to drastically reduce the neccesary computational resources.

- Development of an RWG-based implementation of the SIE methods integrated in the toolkit of the research group for solving non-conformal and quasi-non-conformal discretized problems, in order to facilitate the handling of subdomains and surfaces in the DDM proposed scheme. The ability to independently model, combine and assemble the different subsystems of a large complex problem enhances the versatility of the domain decomposition preconditioner, without caring about mesh conforming or the presence of spurious slits and overlaps due to slight missplacement between subsystems at the tear contours. This is addressed by two different procedures: the equivalent electric and magnetic currents at the tear lines and junctions are expanded in terms of half-RWG (h-RWG) basis functions, and their continuity is enforced in the weak sense through the use of an interior penalty (IP) term in the case of Discontinuous Galerking; and by the use of the novel multibranch-RWG basis functions, which are div-conforming functions defined on quasi-non-conformal discretizations. In addition, new advances in DG methodology are devised and applied for the first time with the JMCFIE formulation to greatly simplify the treatment of piecewise-homogeneous composite objects including arbitrary connections between multi-material regions (which poses the well-known multi-material junction problem). The use of DG and non-conformal discretizations with the JMCFIE allows the seamless solution of these awkward problems without any specific treatment of the junctions (neither within the solver nor by the user), which greatly simplifies the procedure for dealing with multiscale and multiphysics problems. This proposal allows to easily manage the CAD generation and tessellation procedures for multiscale problems and to simplify the resolution process in the DDM scheme.

- Development of an efficiently parallelized combination of a multilevel quasi-Helmholtz decomposition preconditioner in synergy with the MLFMA-FFT for the solution of complex problems exhibiting deep multi-scale features. The inclusion of the novel multibranch functions in this process enables for the first time the application of a quasi-Helmholtz decomposition to a problem discretized by non-conformal meshes. The physical properties of the different parts of the geometry in a really complex system play a fundamental role in the selection of the optimal DDM domains to improve the outer convergence of the method. However, the optimization of the outer iterative method in the DDM scheme results in a complexity shift towards local solvers, which must lead with inner strong interactions and multi-scale features like cavities or arrays of antennas. In these cases, the inclusion of efficient preconditioners such as those developed in this thesis allows to speed-up the convergence of the fast local solvers while optimizing the outer interactions and the general performance of the method.

1.4 Structure of the thesis

This document has been structured in five chapters. The first, and present, introduces formally the scope of the thesis, the objectives and the contributions of the work.

The second chapter is a detailed review of the SIE backgound supporting the methods developed in this work. In particular, fundamental theory and computational algorithmic are described for the full-wave solution of the JMCFIE by the Method of Moments and its acceleration via the multilevel fast multipole algorithm.

In the third chapter, the tear-and-interconnect DDM is developed for PEC and extended to composite piecewise homogeneous objects. Then, the MR preconditioner is combined with the MLFMA-FFT to develop a high efficient local solver to include in the DDM framework.

In chapter fourth, non-conformal techniques based on DG and MB-RWG basis functions are introduced. The previously developed MR preconditioner is also extended to the solution of non-conformal problems.

Chapter fifth introduces the application of the methods developed in this thesis to the solution of extremely multiscale and very challenging problems in EMC engineering and nanoplasmonics with application in biosensing.

Finally, the sixth chapter summarizes the main conclusions of the thesis and some future lines.

Chapter 2

Surface Integral Equation Methods

Contenido

This chapter describes the SIE formulation, which constitutes the background of the procedures developed in this thesis, and establishes the foundation of the notation that will be applied in the rest of the document.

The chapter is structured as follows. First, the electric and magnetic field integral equations and their combinations are formulated for the general case of arbitrary composite PEC and piecewise-homogeneous penetrable objects. Then, the method of moments (MoM) is introduced to transform the integral equations into a matrix system. Finally, the multilevel fast multipole method (MLFMA) is described as an efficient acceleration for the solution of the dense matrix system posed by the MoM.

2.1 Surface Integral equation formulation for composite objects

An arbitrarily shaped piecewise homogeneous penetrable object situated in an unbounded homogeneous medium (free-space for the sake of clarity) is considered, as is shown in figure 2.1. In the following, a time harmonic variation $\exp(jwt)$ is assumed

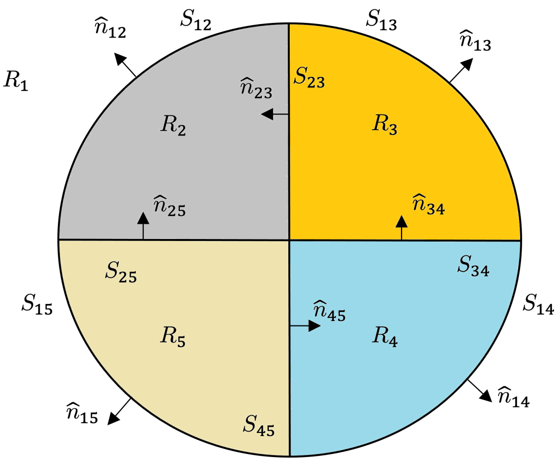

Figure 2.1: Arbitrarily shaped 3-D piecewise homogeneous object. Notation used for the statement of the surface integral equation formulation.

and suppressed from the formulation. Each region R_i is characterized by its electromagnetic properties $\epsilon_i = \epsilon_{ri}\epsilon_0$ and $\mu_i = \mu_{ri}\mu_0$, where ϵ_i is the electric permittivity, μ_i is the magnetic permeability, ϵ_{ri} and μ_{ri} are the relative permittivity and permeability in region R_i and ϵ_0 and μ_0 are the constitutive vacuum parameters. S_{ij} is the interface between regions R_i and R_j. $\hat{\mathbf{n}}_{ij}$ are normal unit vectors to S_{ij} pointing towards R_i, with $\hat{\mathbf{n}}_{ij} = -\hat{\mathbf{n}}_{ji}$. $\mathbf{E}_i^{inc}$ and $\mathbf{H}_i^{inc}$ are the electric and the magnetic incident fields, respectively.

In region R_i, the electric field integral equation (EFIE) and the magnetic field integral equation (MFIE) can be formulated in two alternative ways, depending on the method applied to project the fields onto the surfaces. Let us introduce the equivalent electric and magnetic currents $\mathbf{J}_{ij}(\mathbf{r}')$ and $\mathbf{M}_{ij}(\mathbf{r}')$ on the interfaces S_{ij} that surround R_i, which are related to the fields on this region by $\mathbf{J}_{ij}(\mathbf{r}') = \hat{n}_{ij} \times \mathbf{H}_i(\mathbf{r}')$ and $\mathbf{M}_{ij}(\mathbf{r}') = -\hat{n}_{ij} \times \mathbf{E}_i(\mathbf{r}')$ respectively.

Applying the equivalence principle to the total electric and magnetic fields $\mathbf{E}_i(\mathbf{r}')$ and $\mathbf{H}_i(\mathbf{r}')$ in R_i, the tangential (T) EFIE and MFIE equations are obtained as follows:

$$\begin{aligned}\text{T-EFIE}_i\text{:} \sum_{j' \in G_i} &\left(\eta_i \mathcal{L}_i(\mathbf{J}_{ij'}) - \mathcal{K}_i(\mathbf{M}_{ij'})\right)_{\tan} \\ +\frac{1}{2}\hat{n}_{ij} \times \mathbf{M}_{ij}(\mathbf{r}) &= \left(\mathbf{E}_i^{\text{inc}}(\mathbf{r})\right)_{\tan}, \mathbf{r} \in S_{ij}, \forall j \in G_i \end{aligned} \tag{2.1}$$

$$\begin{aligned}\text{T-MFIE}_i\text{:} \sum_{j' \in G_i} &\left(\mathcal{K}_i(\mathbf{J}_{ij'}) + \frac{1}{\eta_i}\mathcal{L}_i(\mathbf{M}_{ij'})\right)_{\tan} \\ -\frac{1}{2}\hat{n}_{ij} \times \mathbf{J}_{ij}(\mathbf{r}) &= \left(\mathbf{H}_i^{\text{inc}}(\mathbf{r})\right)_{\tan}, \mathbf{r} \in S_{ij}, \forall j \in G_i. \end{aligned} \tag{2.2}$$

In a similar way, the twisted or normal (N) equations in S_{ij} throughout R_i can be written as

$$\begin{aligned} \text{N-EFIE}_i : \hat{n}_{ij} \times \sum_{j' \in G_i} \left(\eta_i \mathcal{L}_i(\mathbf{J}_{ij'}) - \mathcal{K}_i(\mathbf{M}_{ij'}) \right) \\ -\frac{1}{2}\mathbf{M}_{ij}(\mathbf{r}) = \hat{n}_{ij} \times \mathbf{E}_i^{\text{inc}}(\mathbf{r}), \mathbf{r} \in S_{ij}, \forall j \in G_i \end{aligned} \tag{2.3}$$

$$\begin{aligned} \text{N-MFIE}_i : \hat{n}_{ij} \times \sum_{j' \in G_i} \left(\mathcal{K}_i(\mathbf{J}_{ij'}) + \frac{1}{\eta_i}\mathcal{L}_i(\mathbf{M}_{ij'}) \right) \\ +\frac{1}{2}\mathbf{J}_{ij}(\mathbf{r}) = \hat{n}_{ij} \times \mathbf{H}_i^{\text{inc}}(\mathbf{r}), \mathbf{r} \in S_{ij}, \forall j \in G_i. \end{aligned} \tag{2.4}$$

In Eqs. (2.1-2.4) G_i denotes the set of indices of the regions surrounding region R_i (for example, in Fig. 1, $G_2 = \{1, 3, 5\}$), η_i is the intrinsic impedance in medium R_i, $\mathbf{E}_i^{\text{inc}}(\mathbf{r})$ and $\mathbf{H}_i^{\text{inc}}(\mathbf{r})$ are the incident fields due to the sources located inside R_i, and the integro-differential operators $\mathcal{L}$ and $\mathcal{K}$ are defined as

$$\begin{aligned} \mathcal{L}_i(\mathbf{X}_i) = jk_i \int_S \mathbf{X}_i(\mathbf{r}') g_i(\mathbf{r}, \mathbf{r}') dS' \\ +\frac{1}{jk_i}\nabla \int \mathbf{X}_i(\mathbf{r}')\nabla' g_i(\mathbf{r}, \mathbf{r}') dS' \end{aligned} \tag{2.5}$$

$$\mathcal{K}_i(\mathbf{X}_i) = PV \int_S \mathbf{X}_i(\mathbf{r}') \times \nabla g_i(\mathbf{r}, \mathbf{r}') dS' \tag{2.6}$$

with $\mathbf{r}$ the observation points approaching to S_{ij} from the interior of region R_i and with $\mathbf{r}' \in S_{ij'}$ the source points at the boundaries surrounding R_i. ∇' denotes the gradient in the primed (source) coordinates, PV denotes the Cauchy principal value of the integral in Eq. (2.6), k_i is the wavenumber in R_i, and

$$g_i(\mathbf{r}, \mathbf{r}') = \frac{e^{-jk_i|\mathbf{r}-\mathbf{r}'|}}{4\pi|\mathbf{r}-\mathbf{r}'|} \tag{2.7}$$

is defined as the homogeneous Green's function in R_i. The summations in equations (2.1) to (2.4) account for all the interfaces $S_{ij'}$ surrounding R_i (including S_{ij}). $\mathbf{X}_i$ stands for any electric ($\mathbf{J}_i$) or magnetic ($\mathbf{M}_i$) current radiating in R_i. At this point, fulfilling the procedure of [72] to derive a set of stable and well-tested SIEs, the above integral equations are combined in region R_i, leading to the two following combined field integral equations on S_{ij} [73]

$$\text{JCFIE}_i\text{:}\ a_i \frac{1}{\eta_i}\text{T-EFIE}_i + b_i\text{N-MFIE}_i \tag{2.8}$$

$$\text{MCFIE}_i\text{:}\ -c_i\text{N-EFIE}_i + d_i\eta_i\text{T-MFIE}_i \tag{2.9}$$

with a_i, b_i, c_i and d_i the appropriate complex combination coefficients. The next step is to combine Eq. (2.8) for regions R_i and R_j into a single integral equation for each interface S_{ij} as follows:

$$\text{JCFIE}_{ij}\text{:}\ a_i \frac{1}{\eta_i}\text{T-EFIE}_i + a_j \frac{1}{\eta_j}\text{T-EFIE}_j + b_i\text{N-MFIE}_i + b_j\text{N-MFIE}_j \tag{2.10}$$

which substituting (2.1) and (2.4) can be expressed as

$$\begin{aligned}\text{JCFIE}_{ij}\text{:}\ & a_i \sum_{j'\in G_i}\left(\mathcal{L}_i(\mathbf{J}_{ij'}) - \frac{1}{\eta_i}\mathcal{K}_i(\mathbf{M}_{ij'})\right)_{\tan} \\ & + a_j \sum_{j''\in G_j}\left(\mathcal{L}_j(\mathbf{J}_{jj''}) - \frac{1}{\eta_j}\mathcal{K}_j(\mathbf{M}_{jj''})\right)_{\tan} \\ & + b_i\hat{n}_{ij} \times \sum_{j'\in G_i}\left(\mathcal{K}_i(\mathbf{J}_{ij'}) + \frac{1}{\eta_i}\mathcal{L}_i(\mathbf{M}_{ij'})\right) \\ & + b_j\hat{n}_{ji} \times \sum_{j''\in G_j}\left(\mathcal{K}_j(\mathbf{J}_{jj''}) + \frac{1}{\eta_j}\mathcal{L}_j(\mathbf{M}_{jj''})\right) \\ & + \frac{1}{2}\left(\frac{a_i}{\eta_i}\hat{n}_{ij} \times \mathbf{M}_{ij}(\mathbf{r}) + \frac{a_j}{\eta_j}\hat{n}_{ji} \times \mathbf{M}_{ji}(\mathbf{r})\right) \\ & + \frac{1}{2}\left(b_i\mathbf{J}_{ij}(\mathbf{r}) + b_j\mathbf{J}_{ji}(\mathbf{r})\right) \\ & = a_i\frac{1}{\eta_i}\left(\mathbf{E}_i^{\text{inc}}(\mathbf{r})\right)_{\tan} + a_j\frac{1}{\eta_j}\left(\mathbf{E}_j^{\text{inc}}(\mathbf{r})\right)_{\tan} \\ & + b_i\hat{n}_{ij} \times \mathbf{H}_i^{\text{inc}}(\mathbf{r}) + b_j\hat{n}_{ji} \times \mathbf{H}_j^{\text{inc}}(\mathbf{r}), \mathbf{r} \in S_{ij}.\end{aligned} \tag{2.11}$$

In a similar way, Eq. (2.9) is combined for regions R_i and R_j to obtain another single integral equation on S_{ij}:

$$\text{MCFIE}_{ij}\text{:}\ -c_i\text{N-EFIE}_i - c_j\text{N-EFIE}_j + d_i\eta_i\text{T-MFIE}_i + d_j\eta_j\text{T-MFIE}_j \tag{2.12}$$

which applying (2.3) and (2.2) can be expressed as

$$\begin{aligned}
\text{MCFIE}_{ij}\colon\ & -c_i\hat{n}_{ij}\times\sum_{j'\in G_i}\left(\eta_i\mathcal{L}_i(\mathbf{J}_{ij'})-\mathcal{K}_i(\mathbf{M}_{ij'})\right)\\
& -c_j\hat{n}_{ji}\times\sum_{j''\in G_j}\left(\eta_j\mathcal{L}_j(\mathbf{J}_{jj''})-\mathcal{K}_j(\mathbf{M}_{jj''})\right)\\
& +d_i\sum_{j'\in G_i}\left(\eta_i\mathcal{K}_i(\mathbf{J}_{ij'})+\mathcal{L}_i(\mathbf{M}_{ij'})\right)_{\tan}\\
& +d_j\sum_{j''\in G_j}\left(\eta_j\mathcal{K}_j(\mathbf{J}_{jj''})+\mathcal{L}_j(\mathbf{M}_{jj''})\right)_{\tan}\\
& +\frac{1}{2}\left(c_i\mathbf{M}_{ij}(\mathbf{r})+c_j\mathbf{M}_{ji}(\mathbf{r})\right)\\
-\frac{1}{2}\left(d_i\eta_i\hat{n}_{ij}\times\mathbf{J}_{ij}(\mathbf{r})+d_j\eta_j\hat{n}_{ji}\times\mathbf{J}_{ji}(\mathbf{r})\right) &= -c_i\hat{n}_{ij}\times\mathbf{E}_i^{\text{inc}}(\mathbf{r})-c_j\hat{n}_{ji}\times\mathbf{E}_j^{\text{inc}}(\mathbf{r})\\
& +d_i\eta_i\left(\mathbf{H}_i^{\text{inc}}(\mathbf{r})\right)_{\tan}+d_j\eta_j\left(\mathbf{H}_j^{\text{inc}}(\mathbf{r})\right)_{\tan},\mathbf{r}\in S_{ij}.
\end{aligned}\tag{2.13}$$

thereby constituting the JMCFIE formulation.

In the last equations, summations in j' account for all the interfaces $S_{ij'}$ surrounding each region R_i (including S_{ij}), while summations in j'' account for all the interfaces $S_{jj''}$ surrounding each region R_j (including S_{ij}).

The boundary conditions ensuring the continuity of the tangential component of the fields can be enforced in the previous expressions at every interface and wired to the SIE formulation as follows:

$$\mathbf{X}_{ij}(\mathbf{r}')=-\mathbf{X}_{ji}(\mathbf{r}'),\mathbf{r}'\in S_{ij}\tag{2.14}$$

where $\mathbf{X}_{ij}$ stands for $\mathbf{J}_{ij}$ or $\mathbf{M}_{ij}$ on S_{ij}. Equation (2.14) implies that surface currents on opposite sides of an interface are equal in magnitude but have opposite directions.

2.2 Method of Moments

To obtain the equivalent currents $\mathbf{J}_{ij}$ and $\mathbf{M}_{ij}$ on the surfaces S_{ij}, the MoM procedure [1] is applied to the previous equations (2.11) and (2.13). First, for the sake of clarity, the total currents on the surfaces of the whole body are collected as

$$\mathbf{J}(\mathbf{r})=\mathbf{J}_{ij}(\mathbf{r}),\mathbf{r}\in\bigcup_{\substack{i=1..M\\ j\in G_i}}S_{ij}\tag{2.15}$$

$$\mathbf{M}(\mathbf{r})=\mathbf{M}_{ij}(\mathbf{r}),\mathbf{r}\in\bigcup_{\substack{i=1..M\\ j\in G_i}}S_{ij}.\tag{2.16}$$

Then, the currents on the whole body are expanded in a sum of known vector basis functions $\mathbf{f}_n$ in the form

$$\mathbf{J} = \sum_n J_n \mathbf{f}_n \tag{2.17}$$

$$\mathbf{M} = \sum_n M_n \mathbf{f}_n. \tag{2.18}$$

J_n and M_n are the unknown expansion complex coeficientes. Substituting Eqs. (2.17) and (2.18) into Eqs. (2.11) and (2.13) and applying the Galerking testing procedure, a system of linear equations is derived from the integral equations and can be expressed as a dense matrix system as follows:

$$\begin{bmatrix} \overline{\mathbf{Z}}_{ij,ij} & \overline{\mathbf{Z}}_{ij,kl} & \dots & \overline{\mathbf{Z}}_{ij,pq} \\ \overline{\mathbf{Z}}_{kl,ij} & \overline{\mathbf{Z}}_{kl,kl} & \dots & \overline{\mathbf{Z}}_{kl,pq} \\ \vdots & \vdots & \ddots & \vdots \\ \overline{\mathbf{Z}}_{pq,ij} & \overline{\mathbf{Z}}_{pq,kl} & \dots & \overline{\mathbf{Z}}_{pq,pq} \end{bmatrix} \begin{bmatrix} I_{ij} \\ I_{kl} \\ \vdots \\ I_{pq} \end{bmatrix} = \begin{bmatrix} V_{ij} \\ V_{kl} \\ \vdots \\ V_{pq} \end{bmatrix} \tag{2.19}$$

where each block of the impedance matrix is given by

$$\overline{\mathbf{Z}}_{ij,i'j'} = \begin{bmatrix} \overline{\mathbf{Z}}^{1J}_{ij,i'j'} & \overline{\mathbf{Z}}^{1M}_{ij,i'j'} \\ \overline{\mathbf{Z}}^{2J}_{ij,i'j'} & \overline{\mathbf{Z}}^{2M}_{ij,i'j'} \end{bmatrix} \tag{2.20}$$

with

$$\begin{aligned} \overline{\mathbf{Z}}^{1J}_{ij,ij}(m,n) &= a_i A^i_{mn} + a_j A^j_{mn} + b_i B'^i_{mn} - b_j B'^j_{mn} \\ &\quad + \frac{1}{2}\left(b_i + b_j\right) I_{mn} && (2.21) \\ \overline{\mathbf{Z}}^{1M}_{ij,ij}(m,n) &= -\frac{a_i}{\eta_i} B^i_{mn} - \frac{a_j}{\eta_j} B^j_{mn} + \frac{b_i}{\eta_i} A'^i_{mn} - \frac{b_j}{\eta_j} A'^j_{mn} \\ &\quad + \frac{1}{2}\left(\frac{a_i}{\eta_i} - \frac{a_j}{\eta_j}\right) I'_{mn} && (2.22) \\ \overline{\mathbf{Z}}^{2J}_{ij,ij}(m,n) &= d_i \eta_i B^i_{mn} + d_j \eta_j B^j_{mn} - c_i \eta_i A'^i_{mn} + c_j \eta_j A'^j_{mn} \\ &\quad - \frac{1}{2}\left(d_i \eta_i - d_j \eta_j\right) I'_{mn} && (2.23) \\ \overline{\mathbf{Z}}^{2M}_{ij,ij}(m,n) &= d_i A^i_{mn} + d_j A^j_{mn} + c_i B'^i_{mn} - c_j B'^j_{mn} \\ &\quad + \frac{1}{2}\left(c_i + c_j\right) I_{mn} && (2.24) \end{aligned}$$

for the self-coupling of surface S_ij,

$$\overline{\mathbf{Z}}^{1J}_{ij,ij'}(m,n) = a_i A^i_{mn} + b_i B'^i_{mn} \tag{2.25}$$

$$\overline{\mathbf{Z}}^{1M}_{ij,ij'}(m,n) = -\frac{a_i}{\eta_i} B^i_{mn} + \frac{b_i}{\eta_i} A'^i_{mn} \tag{2.26}$$

$$\overline{\mathbf{Z}}^{2J}_{ij,ij'}(m,n) = d_i \eta_i B^i_{mn} - c_i \eta_i A'^i_{mn} \tag{2.27}$$

$$\overline{\mathbf{Z}}^{2M}_{ij,ij'}(m,n) = d_i A^i_{mn} + c_i \eta_i B'^i_{mn} \tag{2.28}$$

for the mutual coupling between surfaces S_{ij} and $S_{ij'}$ sharing region R_i, and

$$\overline{\mathbf{Z}}^{1J}_{ij,jj''}(m,n) = -a_j A^j_{mn} + b_j B'^j_{mn} \tag{2.29}$$

$$\overline{\mathbf{Z}}^{1M}_{ij,jj''}(m,n) = \frac{a_j}{\eta_j} B^j_{mn} + \frac{b_j}{\eta_j} A'^j_{mn} \tag{2.30}$$

$$\overline{\mathbf{Z}}^{2J}_{ij,jj''}(m,n) = -d_j \eta_j B^j_{mn} - c_j \eta_j A'^j_{mn} \tag{2.31}$$

$$\overline{\mathbf{Z}}^{2M}_{ij,jj''}(m,n) = -d_j A^j_{mn} + c_j \eta_j B'^j_{mn} \tag{2.32}$$

for the mutual coupling between surfaces S_{ij} and $S_{jj''}$ sharing region R_j. On the previous equations some integral terms are defined:

$$A^i_{mn} = \int_{\Delta_m} \mathbf{f}_m \cdot \mathcal{L}_i(\mathbf{f}_n) dS \tag{2.33}$$

$$B^i_{mn} = \int_{\Delta_m} \mathbf{f}_m \cdot \mathcal{K}_i(\mathbf{f}_n) dS \tag{2.34}$$

$$A'^i_{mn} = \int_{\Delta_m} \mathbf{f}_m \cdot \hat{n}_m \times \mathcal{L}_i(\mathbf{f}_n) dS \tag{2.35}$$

$$B'^i_{mn} = \int_{\Delta_m} \mathbf{f}_m \cdot \hat{n}_m \times \mathcal{K}_i(\mathbf{f}_n) dS \tag{2.36}$$

$$I^i_{mn} = \int_{\Delta_m} \mathbf{f}_m \cdot \mathbf{f}_n dS \tag{2.37}$$

$$I'^i_{mn} = \int_{\Delta_m} \mathbf{f}_m \cdot \hat{n}_m \times \mathbf{f}_n dS \tag{2.38}$$

where Δ_m is the subdomain where function $\mathbf{f}_m$ is defined.

2.3 Multilevel Fast Multipole Algorithm - Fast Fourier Transform

The standard MoM procedure and the Galerkin's testing method provide an $N \times N$ dense matrix whose solution are the N unknown coefficients I_n of the expansion of the equivalent currents density in terms of basis functions.

To reduce the otherwise prohibitive computational cost of the MoM for the case of large-scale geometries, we apply the MLFMA-FFT. This is an extension of MLFMA to speed-up the matrix-vector-product (MVP) in the framework of an iterative resolution of the problem. Assuming an octree spatial decomposition of the geometry into a set of groups, the MVP in group p can be obtained using FMM as

$$\begin{aligned}\sum_{n=1}^{N} Z_{mn} I_n = \sum_{q\in B_p}\sum_{n\in G_q} Z_{mn} I_n + \left(\frac{-jk}{4\pi}\right)^2 \\ \int_{S^2} \mathbf{V}_{mp} \sum_{q\notin B_p} \alpha_{pq}(k,\mathbf{r}_{pq}) \sum_{n\in G_q} \mathbf{V}_{qn}(\hat{k}) I_n d^2\hat{k}, m\in G_p \end{aligned} \tag{2.39}$$

where B_p is the set of indexes for the nearby (adjacent) groups of group p, G_p is the set of indexes corresponding to the testing functions of group p, G_q is the set of indexes corresponding to the basis functions of group q, and S^2 is the Ewald unit sphere. In Eq. (2.39), the near interactions between basis and testing functions belonging to adjacent groups are calculated using the direct MoM procedure. The far (non-adjacent) group contributions are accounted for using the standard FMM [74] by (i) aggregating the radiation of the basis functions within each group q to the center of their groups

$$\mathbf{V}_{qn}(\hat{k}) = \int_{\Delta_n} (\bar{\mathbf{I}} - \hat{k}\hat{k}) \cdot \mathbf{f}_n(\mathbf{r}) e^{-j\mathbf{k}\cdot(\mathbf{r}_q-\mathbf{r})} dS \tag{2.40}$$

where $\mathbf{r}_q$ is the center of the qth group and with $\bar{\mathbf{I}}$ the 3-D unit dyad; (ii) Translating the aggregated radiations between the different groups using the translator operator

$$\alpha_{pq}(k,\mathbf{r}_{pq}) = \sum_{l=0}^{L} (-j)^l (2l+1) h_l^{(2)}(kr_{pq}) P_l(\hat{k}\cdot\hat{r}_{mn}) \tag{2.41}$$

where $h_l^{(2)}$ is the spherical Hankel function of the second kind, P_l is the Legendre polynomial of degree l, and L is the number of multipole expansion terms [41]; And (iii), disaggregating the receiving patterns to the testing functions within each receiving group p

$$\begin{aligned}\mathbf{V}_{mp}(\hat{k}) = \alpha \int_{\Delta_m} (\bar{\mathbf{I}} - \hat{k}\hat{k}) \cdot \mathbf{f}_m(\mathbf{r}) e^{-j\mathbf{k}\cdot(\mathbf{r}-\mathbf{r}_p)} dS \\ -(1-\alpha)\hat{k} \times \int_{\Delta_m} \mathbf{f}_m \times \hat{n}_m(\mathbf{r}) e^{-j\mathbf{k}\cdot(\mathbf{r}-\mathbf{r}_p)} dS \end{aligned} \tag{2.42}$$

With this algorithm, the computational cost is reduced from $O(N_{it}N^2)$ to $O(N_{it}N^{1.5})$, with N_{it} the number of iterations required to obtain a prescribed residual error.

Using MLFMA the computational cost of the MVP can be further reduced to $O(N_{it}N\log N)$, using exponential translation, interpolation and adjoint interpolation (or anterpolation) of the fields, in the framework of a multilevel octree decomposition of the geometry. Additionally, to benefit from the availability of multicore distributed computers, the MLFMA-FFT extension is applied. This algorithm implements the translation between groups at the coarsest level of the octree decomposition by performing a 3-D circular convolution per sample of the Ewald sphere. This operation is efficiently done in the transformed domain applying the FFT. MLFMA-FFT avoids inter-process communication and equally distributes the workload among parallel processes, posing a highly scalable parallel implementation. Solutions of surface integral equation with up to one billion unknowns have been obtained using this method [75,76].

Chapter 3

Domain Decomposition Method

Contenido

After introducing background and notation for the SIE in the previous chapter, the present chapter focuses on the detailed description of the DDM implementation, which is one of the main developments of this thesis and constitutes the framework for further contributions that have been devised. A multilevel *tear-and-interconnect* DDM approach is developed and combined with the methods presented in Chapter 2 to address the solution of composite multimaterial objects. Highly scalable preconditioners are described for the acceleration of the local solvers in the DDM scheme. Several validation examples are also included to illustrate the capabilities of the proposed methods.

3.1 Introduction

Domain decomposition methods based on transmission conditions have been successfully used for the resolution of electromagnetic scattering from complex penetrable and non-penetrable problems with different electromagnetic properties and multiscale features. The idea is to decompose the original problem into a collection of smaller subdomains which are solved separately and coupled back together, thus reducing the iteration count and abling the solution of challenging problems with a good degree of success.

The DD paradigm was initially conceived for the preconditioning of finite element methods [77, 78], but it was finally extended to conventional SIE approaches, first applied to non-penetrable bodies [48]– [79] and later on extended to penetrable and composite objects [49], [80]– [52]. They provide the preconditioning necessary to overcome the problems of ill-conditioning of the dense matrix system of linear equations that results from the conventional SIE-method of moments formulation, and the subsequent problems of slow convergence of the accelerated iterative solution. DDM takes advantage of natural partitioning rules given by the scale and/or physics of each block of the global geometry to split the entire problem into subdomains. Therefore, subdomains are coupled together taking into account the proper transmission conditions between them and iterating in an external Krylov loop (GMRES [39]).

A possible drawback of the usual DDM approach is that it implies the introduction of auxiliary unknowns on artificial interfaces to close the subdomains and enforce the transmission conditions, which in some cases results in a significant computational cost overhead [45]. In this thesis, we propose an alternative tear-and-interconnect SIE-DDM approach which can be applied to non-penetrable and penetrable bodies, which does not require the use of artificial surfaces between adjacent domains to get them closed. The transmission conditions preventing unphysical reflections from the subdomain interfaces are enforced along the tearing contours between subdomains, avoiding the effects of charge accumulations along the artificial cuts. Additionally, this scheme greatly simplifies the algorithm, which indeed can be more easily embedded into existing SIE codes, and it has a good propensity for parallelization over distributed computers.

3.2 Tear-and-Interconnect Additive Schwarz DDM Formulation

In this thesis, a multilevel additive Schwarz DDM preconditioner [62, 81] is applied for the solution of the matrix system in (2.19). The procedure starts by applying a partition of the geometry according to the geometrical features, materials and the particularities of the different blocks and subsystems of the overall problem. The naturally splitting properties of the systems under study (perfect electric conductor surfaces, antennas, etc.) can be exploited to avoid the introduction of artificial subdivisions and interfaces. This results in a DD of the objects boundary surfaces into a collection of non-overlapping touching and/or non-touching subdomains. The matrix equation in (2.19) can be then left-preconditioned throughout the solutions of the individual subdomains, as follows:

$$\mathbf{P} \cdot \mathbf{Z} \cdot I = \mathbf{P} \cdot V \tag{3.1}$$

where $\mathbf{P}$ is the DDM block diagonal preconditioner, which can be written as:

$$\mathbf{P} = \begin{bmatrix} \mathbf{P}_1 & & & 0 \\ & \mathbf{P}_2 & & \\ & & \ddots & \\ 0 & & & \mathbf{P}_p \end{bmatrix} \tag{3.2}$$

with p the number of subdomains in the DDM. Each $\mathbf{P}_i$ block is the inverse of the impedance matrix block $\mathbf{Z}_i$ governing the local problem enclosed in subdomain i (denoted as D_i). The subdomain matrix $\mathbf{Z}_i$ can be obtained as:

$$\mathbf{Z}_i = \mathbf{R}_i \cdot \mathbf{Z} \cdot \mathbf{R}_i^T \tag{3.3}$$

where $\mathbf{R}_i$ is a restriction matrix that maps the complete vector of unknowns to the sub-vector of unknowns corresponding to subdomain D_i $(I_i = \mathbf{R}_i \cdot I)$, and where the transpose $\mathbf{R}_i^T$ is the prolongation matrix that extends a sub-vector I_i into the whole domain. The DDM block diagonal preconditioner can be then built as:

$$\mathbf{P} = \sum_{i=1}^{p} \mathbf{R}_i^T \cdot \mathbf{Z}_i^{-1} \cdot \mathbf{R}_i \tag{3.4}$$

The rightmost MVP in the left-hand side of (3.1), $\tilde{V} = \mathbf{Z} \cdot I$, corresponds to the global (outer) MVP, coupling the different subdomain solutions with one another. Meanwhile, the leftmost product by the matrix $\mathbf{P}$ provides the preconditioner individual subdomain solutions, which can be written as $\tilde{I}_i = \mathbf{P}_i \cdot \tilde{V}_i$, with $\tilde{V}_i = \mathbf{R}_i \cdot \tilde{V}$. Though formally written in (3.4) with the inverses of the subdomain matrices, the individual solutions imply solving the following independent subdomain matrix systems by the method deemed appropriate in each case:

$$\mathbf{Z}_i \cdot \tilde{I}_i = \tilde{V}_i \tag{3.5}$$

Once these "inner" subproblems are solved, their solutions are assembled together yielding the whole solution of currents at the actual global iteration, as:

$$\tilde{I} = \sum_{i=1}^{p} \mathbf{R}_i^T \cdot \tilde{I}_i \tag{3.6}$$

Different SIE formulations can be applied to derive the matrix system of linear equations. We use in this thesis the JMCFIE formulation described in Chapter 2, as it poses a well-conditioned system of linear equations for both the equivalent electric and magnetic currents. Initially, for the discretization of the integral equations the so-called multiregion piecewise vector basis functions [73] are used, which implicitly satisfy the boundary conditions for the currents on the boundary surfaces and line junctions where different material regions intersect.

3.2.1 Transmission Conditions

In order to achieve good convergence with the above preconditioner, it is essential to enforce the so-called transmission conditions among touching subdomains. In [48], artificial PEC surfaces are defined in order to close the open regions that arise from the splitting phase, while the approach of [82] utilizes the information of the near-range couplings. To impose the transmission conditions that guarantee the continuity between domains connected in the original problem, in this thesis we apply a procedure consisting of enlarging the subdomains to incorporate the near-field current flowing across the tearing contours. Thus, instead of solving equation (3.5), the following equation for the augmented (overlapping) subdomains is solved:

$$\mathbf{Z}'_i \cdot \tilde{I}'_i = \tilde{V}'_i \tag{3.7}$$

where $\mathbf{Z}'_i = \mathbf{R}'_i \cdot \mathbf{Z} \cdot \mathbf{R}'^T_i$ is the impedance matrix block of the augmented subdomain D'_i, $\tilde{V}'_i = \mathbf{R}'_i \cdot \tilde{V}$ and $\mathbf{R}'_i$ and $\mathbf{R}'^T_i$ are the restriction and prolongation matrices for the augmented subdomain D'_i respectively. Once these systems are solved, their solutions are restricted-back to the original non-overlapped subdomains, as $\tilde{I}_i = \mathbf{R}_i \cdot \mathbf{R}'^T_i \cdot \tilde{I}'_i$, and assembled together to provide the whole solution of currents at the actual stage using (3.6).

In the implementation developed in this thesis, the enlargement to build the augmented subdomains is done by including "flaps" of a quarter to a half wavelength width belonging to the adjacent (touching) subdomain(s). Otherwise, the restriction and prolongation matrices are not explicitly implemented. Instead, the subdomains are constructed following an orderly sequence from the meshed CAD models, which are generated specifically to facilitate the application of the domain decomposition.

Each subdomain is an independent CAD model composed of two components: First, a *reduced* domain, which could be made of one or more surfaces; second, one or more inner flap surfaces. The inner flaps of one domain are intended to be part of the outer flaps of the adjacent domains. The union of reduced domain and inner flap(s), constitutes the *actual* or *restricted* domain, while the union of restricted domain and the outer flaps is named as *augmented* domain.

The components of each domain are assembled and meshed together. Far from constituting a problem, this way of working is common in the current CAD packages. Different entities can be composed and meshed together, providing subsequent access separately to the mesh (or specific sub-mesh) portion corresponding to each entity.

In the first instance, conformal meshes are applied to guarantee the current flow across touching subdomains. In the next chapter, an alternative paradigm is presented to deal with non-conformal discretizations, which is much more amenable to deal with highly complex structures. However, here we need that the different subdomains have conformal discretizations at the *tear* contours, defined as the touching lines between inner flaps of adjacent domains (that is, between adjacent restricted domains). Nevertheless, this operation is still available in most of the current meshing packages, usually just by specifying the number of edges in which a contour must be discretized. The multiregion basis functions are subsequently calculated within each subdomain. Noticeably, all the required degrees of freedom are present at this stage except those defined at the tearing contours, which will be defined during the DDM assembly stage.

As a result, a complete set with the different meshed components of each subdomain is obtained. The generation of the DDM framework is an user-friendly process that takes as input the conformal but independent meshes of each restricted subdomain (reduced domain and flaps). The DDM structure of the entire problem is subsequently obtained by automating the assembly of the subdomain components, leading to the global geometry structure (ordered according to the spatial DD) and indexing lists to the different restricted and augmented subdomains. With this scheme, applying the restriction operator simply corresponds to picking the vector elements belonging to a specific subdomain (restricted or augmented). Similarly, applying the prolongation operator corresponds to putting the elements back in their correct positions of the global structure. Remarkably, the multiregion basis functions guaranteeing current flow across the tearing contours are generated at this stage and, importantly, assigned only to one of the two touching subdomains, in each case.

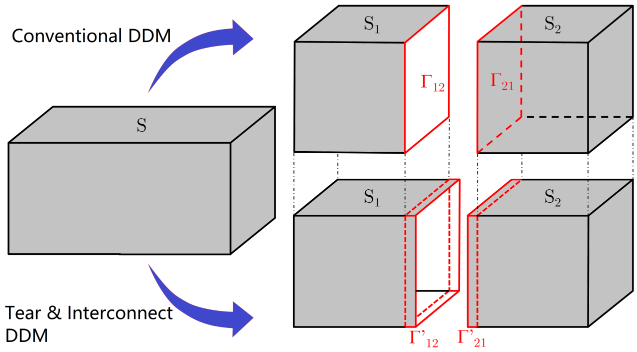

Figure 3.1: Sketch of the geometry decomposition into subdomains using conventional and T&I approaches

The procedure is illustrated in Fig. 3.1, compared to the conventional approach using artificial closing surfaces. The original (penetrable or non-penetrable) domain, whose boundary surface is denoted as S, is split into two subdomains, D_1 and D_2, made up as $D_1 = S_1 \cup \Gamma_{12}$ and $D_2 = S_2 \cup \Gamma_{21}$ in the conventional DD partition, and $D_1 = S_1 \cup \Gamma'_{12}$ and $D_2 = S_2 \cup \Gamma'_{21}$ in the tear-and-interconnect approach. Using this last approach, D_1 and D_2 are not the subdomains really solved in each global iteration, but the augmented subdomains are solved instead, build up as $D'_1 = S_1 \cup \Gamma'_{12} \cup \Gamma'_{21}$ and $D'_2 = S_2 \cup \Gamma'_{21} \cup \Gamma'_{12}$. Once the local solutions of the augmented subdomains are found, these solutions are restricted back to the original subdomains, D_1 and D_2, and assembled to provide the global solution. The portions of the solutions belonging to the enlargement flaps in each case (Γ'_{21} and Γ'_{12}, respectively) are discarded, thus paving the way to the global iterative solver, which will not have to deal with the cancellation of the electric potentials produced by the charges accumulated along the contours. Remarkably, the size of the quarter to a half wavelength width enlargement flaps, Γ'_{12} and Γ'_{21}, as required by the tear-and-interconnect approach, is usually much smaller than the auxiliar (artificial) surfaces Γ_{12} and Γ_{21} required to close the subdomains in the conventional DDM approach.

It is important to point out that this formulation is valid for all kinds of non-penetrable and piecewisely homogenous penetrable composite materials. This, together with the previously mentioned ability to deal with both closed and open surfaces, extends its applicability to the pursued real-life EMC/EMI and plasmonics problems.

3.2.2 Multisolver step and Acceleration of Mutual Coupling Calculation

Solving the preconditioned problem stated in (3.1) involves the resolution of the subdomain matrix systems in (3.5). For small subdomains, e.g. those containing small antennas, the quickest way to proceed is to apply the direct resolution of the MoM, by calculating and storing the factorization of the impedance matrices in (3.5). The resolution of these subdomains in each global iteration is thus calculated in negligible time. Even for subdomains with several tens of thousands of unknowns, this can compensate for a longer setup time, especially if several right-hand parts are to be solved (for example during calculation of mutual coupling between several antennas). Conversely, accelerated iterative methods are preferred for electrically medium or large subdomains to reduce the computational time and memory. In the proposed scheme, independent and highly scalable MLFMA-FFT algorithms [75] are applied tailored to the specific features and materials of each subdomain and using their own local octrees. Any other SIE fast algorithms could be employed easily, however, without changes in the proposed DDM framework.

Additionally, solving (3.1) also requires the calculation of the rightmost MVP in the left hand side of that expression. This is the global MVP that couples the different subdomain solutions with one another in each iteration. Two alternatives are considered at this stage. The first and more straightforward consists of applying the hybrid MLFMA-FFT algorithm to directly compute this MVP, using a global octree partitioning of the entire computational domain. This, however, results in a large memory footprint. A more efficient approach consists of recycling the local octrees and MLFMA frameworks of the individual subdomains to calculate the self-coupling terms of the MVP, as well as to accelerate the near-field radiation of electric and magnetic fields to all other (observation) subdomains [83]. At the observation subdomains, the incoming radiation patterns are summed-up and projected into the testing functions, thus completing the MVP. Special treatment is required at the tearing basis and testing functions to account for the Cauchy singular terms bound to identity terms in overlapping zones between subdomains. This approach reduces the memory burden while providing an implementation with a high parallel propensity. In addition, it impacts favorably on other important issue related with composite material problems. The presence of materials with different physical properties complicates the optimal choice of setup configuration parameters of the MLFMA such as the cell size or the number of multipoles to achieve good convergence. Using accelerated near-field radiation between domains allows to avoid this critical point and reinforces the multisolver character of the implementation.

3.2.3 MPI/OpenMP parallel implementation

Regarding the code implementation, the object-oriented programming language C++ is used. The use of C++ provides a clear, readable and modular code and also a precise low-level control of the memory management. It should be noted that each solver used to address the inner problems is defined as object oriented class dynamic library independently compiled and linked to the DDM framework. In that way, each solver class is instantiated when creating as much objects of that class as subdomains that are going to use that solver. Static initialization of the inner solvers is used to avoid the repetition of the subdomain solver setup for each external iteration. Each subdomain solver object is instantiated only once at the very beginning of the simulation. This programming strategy takes the DDM "divide and conquer" approach one step further, by being applied to the implementation of the code itself. New solvers (general or ad-hoc for certain subdomains) can be straightforwardly included into the DDM framework by building the proper shared libraries after defining the extern interface data structures and methods. The iterative solver used in each Krylov loop is the GMRES implementation from the book of SIAM Templates [39], adapting the code for complex arguments and parallelizing it using the OpenMP standard.

Simultaneously to these algorithmic advances, there has been a sustained growth in computer technology, leading to massively parallel high performance computing (HPC) computers, whose computing capabilities are constantly growing. Nevertheless, for this to result in a real advance in simulation capacity, thus getting closer to the real industrial necessities, it is very important that solvers can benefit from the large amount of parallel computing resources of the new architectures. In this context, the efficient parallelization of the available fast solvers becomes a priority task.

A hybrid MPI/OpenMP parallel implementation of the DDM in distributed mixed memory computers is proposed for the simulation of extremely large scale and complex problems. In this section, the details of its efficient parallel implementation are presented, describing the different stages of the parallel algorithm.

Solving the DDM preconditioned problem stated in (3.1) involves the local (independent) resolution of the subdomain matrix systems involved in (3.2) at each stage of the external iterative Krylov algorithm. At a first glance, as the DDM is a "divide and conquer" approach, this property could be applied for simple parallel implementation on shared memory computers. However, supporting shared-memory parallelization in the domain decomposition might not be the best option, since the load balance would be strongly conditioned by the partition of the problem, which is done at the user level. A much more advantageous option is to include the shared memory parallelization into the local solvers of each subdomain, decoupling the load balance among processors from the domain decomposition of the geometry (see Fig. 3.2). With this scheme, the domain decomposition depends only on the problem nature and the user preferences. An arbitrary number of subdomains can be send to each distributed computing node, depending on the computing resources available. For small subdomains, shared-memory parallel implementations of the direct method of moments can be applied, by calculating and storing the factorization of the impedance matrices in (3.2). The resolution of these subdomains in each global iteration can be then calculated in negligible time. For electrically larger subdomains, a shared-memory parallel implementation of

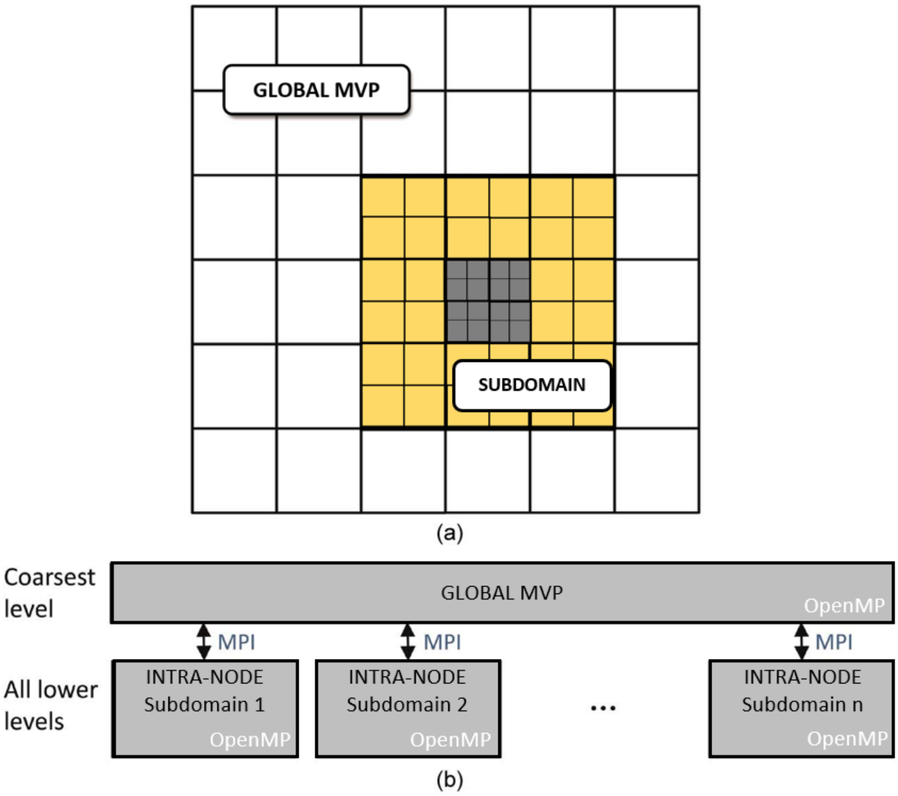

Figure 3.2: (a) Multilevel octree partition of the geometry; (b) Global coupling calculation.

MLFMA is applied to reduce computational time and memory.

Remarkably, solving (3.1) also requires the calculation of the rightmost matrix-vector-product (MVP) in the left hand side of that expression. This is the global MVP that couples the different subdomain solutions with one another in each iteration. As the domain decomposition subdomains are distributed among different (distributed) computing nodes, its calculation will necessarily involve communications at the network level.

The high-scalability MLFMA-FFT algorithm [75] was adapted in this thesis to compute this distributed MVP using a global (locally compatible) octree partition of the entire computational domain. The global MVP calculation can be decomposed in the following three steps:

- At the first step, the near-field couplings are computed at the process level by recycling the local frameworks of each subdomains. In the case of MLFMA subdomains, the near-field interaction contained in the local MLFMA solvers are applied. And in the case of subdomains solved by MoM, the DDM scheme takes advantage of these MoM matrices to avoid the calculation (and memory requirements) of some blocks of the near-field interactions present in the global near-field coupling.

- At the second step, the far-field interactions of lower levels of the octree are computed for the source octree cells and the interaction belonging to other process is communicated to the corresponding process using an ALL to ALL scheme.
- And at the third step, the far-field interactions at the coarsest level are computed with FMM-FFT through a distributed transpose of source interactions that allow the local parallelization at the directions level, combining with an ALLtoALLw scheme that avoid the build of a global FFT translation matrix.

The above parallelization approach is very efficient when dealing with PEC problems or large homogeneous dielectric objects. However, in the case of problems that combine large dielectric objects with large assemblies of composite multi-region objects, it is necessary to develop a different algorithm that takes advantage of the geometrical and physical features of each domains at the global MVP level to reduce unnecessary calculations.

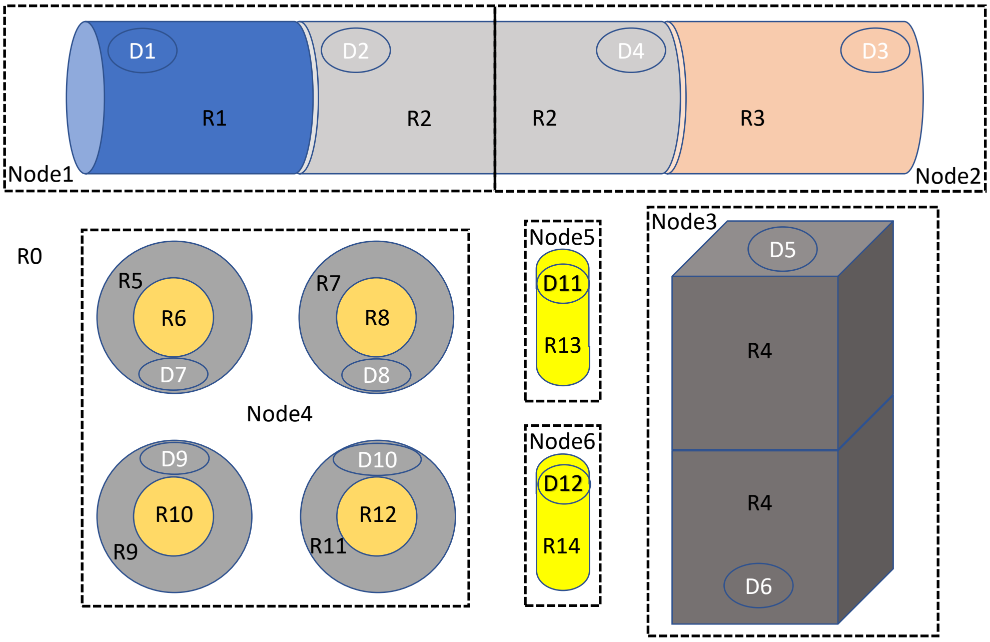

Figure 3.3: Domain and region distribution of a composite multi-material object analyzed with DDM.

At this point, different coupling schemes are proposed to compute the global couplings depending on the kind of dielectric region. It will be explained with the example shown in Fig. 3.3. In this theoretical example, the DDM strategy is applied to a collection of geometric canonical forms, providing eight structures subdomains (shown in

Fig. 3.3). The problem is decomposed into 12 subdomains that are distributed along 6 mpi processes. At this point, the particularities of each region are taking into account, depending on where the belonging domains are distributed, to the efficient solution of the global coupling interaction:

- External global regions that are shared by all processes (such as region 0 in the above example) are computed by the procedure described previously in this section.
- Regions shared by several subdomains corresponding to different MPI processes (such as region 2) are computed by MLFMA-FFT but only with communications between the involved computing nodes, without synchronization with other processes.
- Regions shared by several subdomains corresponding to the same MPI process (such as region 4) are computed by a conventional MLFMA framework without communications.
- Regions corresponding to only one subdomain are computed using the framework of the local solvers, taking advantage of the MLFMA structures (regions 1 and 3) or extracting these interactions from the MoM matrix (regions 5 to 14), recycling the matrix in the case of linked subdomains with repetition patterns (matrix interactions recycled from inner regions of D7 to inner regions of D8 to D10).

Finally, the proposed implementation also takes advantage of the Non Uniform Memory Architecture (NUMA) nodes distribution, reducing the inter-core communications. Importantly, to avoid large memory footprints, the global octree must be compatible with the local ones, so the (persistent) data stored in the local MLFMA frameworks of the individual subdomains is recicled to calculate the self- and mutual-coupling terms of the global MVP. At the observation subdomains, the incoming radiation patterns are summed-up and projected into the testing functions using their local MLFMA frameworks, thus completing the MVP. The proposed approach greatly reduces the memory burden, providing an extremely scalable implementation both in time and, especially, in memory.

3.2.4 Validation and application

In this section, the effectiveness of the proposed SIE-DDM implementation is illustrated for the solution of EM radiation and scattering problems. All the simulations shown in this section were performed in a cluster with 4× Xeon E7-8867v3@2.5GHz (4×16 cores = 64 cores) and 1 TB of RAM memory.

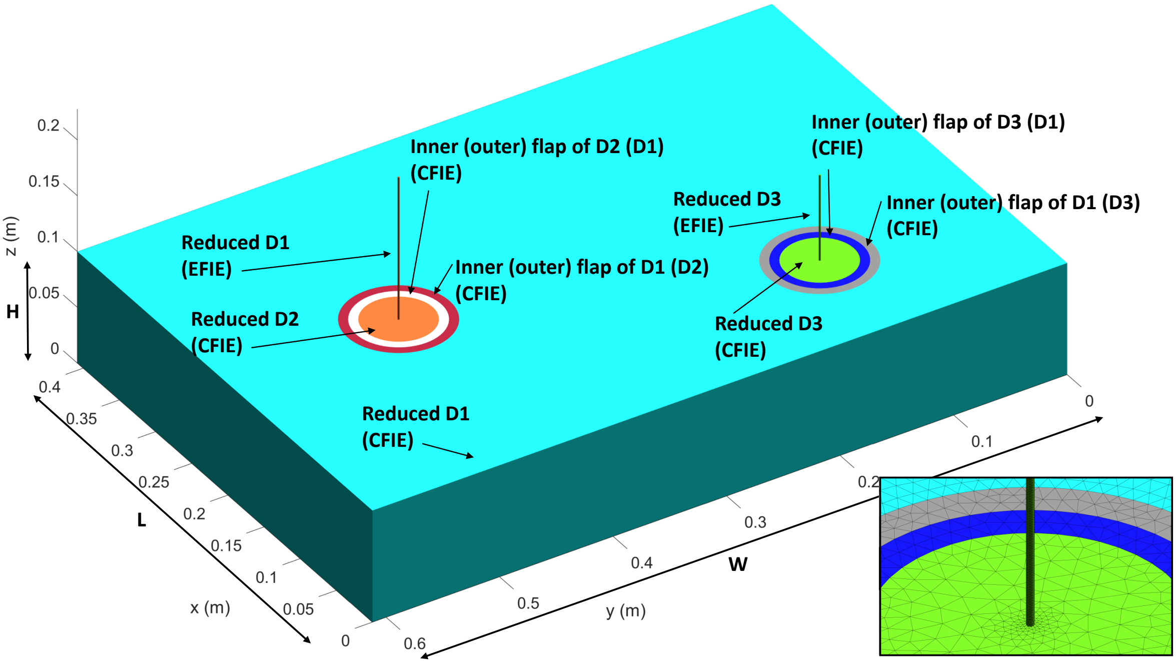

Figure 3.4: Set of the geometry surfaces which make up the subdomains and detail of the multiscale.

To begin with, the coupling between two monopole mounted on a finite ground plane (for which measurements are available in [84]) is studied [85]. The dimensions (W×L×H) of the ground plane are 612 × 408 × 100 mm and the diameter of the monopoles is 1.5748 mm, while their lengths are 765 mm (long monopole) and 127.5 mm (short monopole). Further details can be looked up in [84]. The geometry is subdivided into 3 subdomains: D_1 contains the ground plane, D_2 includes the long monopole antenna and D_3 the short one. The surfaces that form the subdomains are shown in Figure 3.4. It can also be observed in the inset of this figure the multiscale features present in this geometry.

The computed S_{11} parameter of the larger monopole and the S_{12} parameter, representing the isolation between the two monopoles, are shown versus frequency in Figure 3.5. A good agreement between the computed results and the measurements can be observed.

Next, two additional validation examples are considered to illustrate the ability and accuracy of the proposed procedure to decompose the simulation of fully homogeneous dielectric objects. A dielectric polytetrafluoroethylene (Teflon) cylinder is considered first, with 12.5 m in length, 2.5 m radius, and a relative permittivity and permeability of $\epsilon_r = 2.1 - j0.00042$ and $\mu_r = 1$. A $\hat{\theta}$ polarized plane wave impinging on the cylinder with $\theta_{inc} = 45°$ and $\phi_{inc} = 0°$ at a frequency of 300 MHz is considered as the excitation. Following the tear-and-interconnect procedure, the cylinder is decomposed into three open subdomains, as illustrated in Fig. 3.6, where the overlapping flaps to construct the

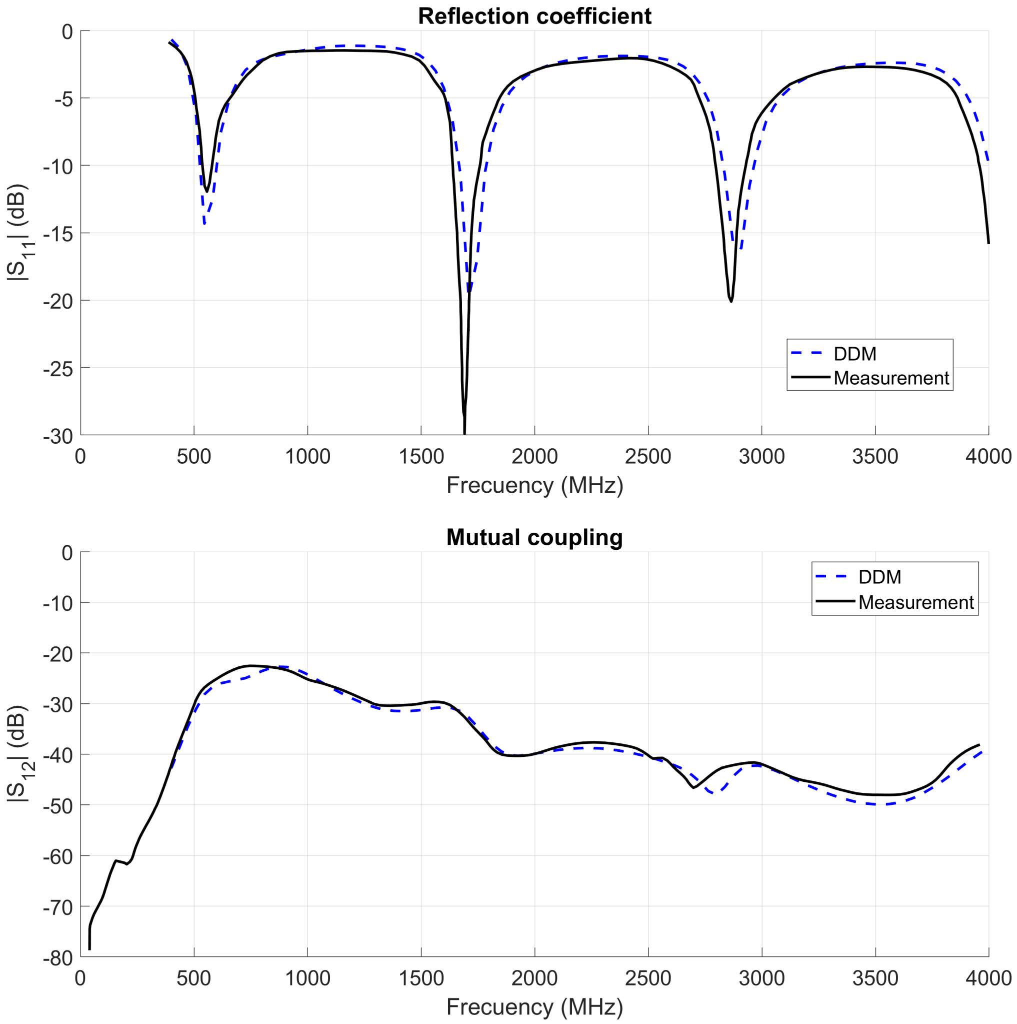

Figure 3.5: S parameters. Simulations versus measurements. (a) S_{11} of the long monopole; (b) Coupling S_{12} of the two monopoles on the ground plane.

augmented subdomains are also shown (using the notation of Fig. 3.1). A fairly dense discretization was applied to benefit iterative convergence, posing 1 615 392 unknowns for the equivalent electric and magnetic currents. Fig. 3.7 shows the equivalent electric and magnetic current distributions on the surface for the DDM solution, calculated with the JMCFIE formulation for penetrable bodies.

The parallel MLFMA-FFT algorithm was applied to speed-up both the reference (single-domain) solution, as well as the local solutions and the global MVP within the DD method. Looking at Fig. 3.7, it can be seen that no artifacts are observed around the tearing lines, with the current perfectly flowing between subdomains. Additionally, the DDM current solution does not show appreciable differences with the reference solution calculated with conventional MLFMA-FFT (not shown as they are identical).

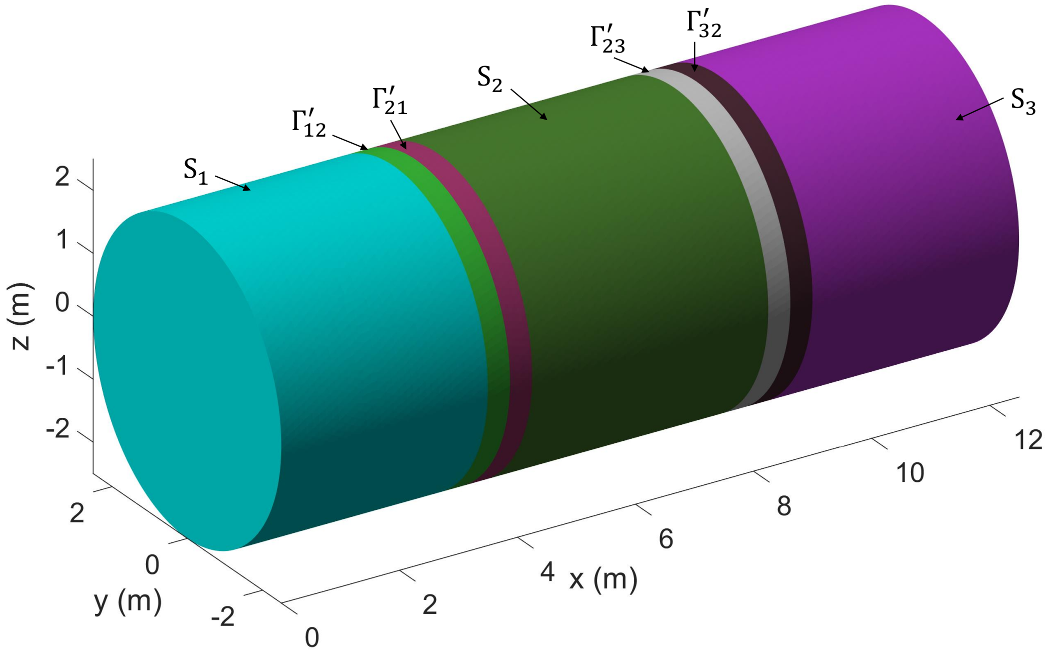

Figure 3.6: Dielectric cylinder and partition into subdomains.

Bistatic radar cross sections (RCS) at $\theta = 45$ were also calculated for the previous impinging wave, and shown in Fig. 3.8. An excellent agreement between the DDM and the reference MLFMA-FFT solution is observed. Iterative count and time to solve (wall-clock time) convergences are gathered in Fig. 3.9 for both the DD and the reference solution. A strong reduction of the iteration number required to attain an iterative Krylov residual error below 10^{-6} is observed for the case of the DDM solution, where only 48 iterations were required. This contrasts with the more than 1 400 iterations required for the the reference solution. Nevertheless, despite the sharp reduction of the iterative count, it is important to note that the application of the DDM preconditioner poses a significant increase in the cost per iteration. Indeed, the better convergence rates are reached if a high precision is ascribed to the inner solvers making up the preconditioner (consequently, the same iteration tolerances have been prescribed for inner problems as for the external solver).

A better figure of merit to compare both solutions in terms of computational cost is the wall-clock time required to complete the calculations. Looking at Fig. 3.9 (down), it can be observed that the wall-clock convergence is much faster in the reference MFLMA-FFT solution. This is as expected, considering that this is a well-conditioned homogeneous example, without multiscale features or multiple materials, which was entirely solved on a shared-memory computing node. Using DDM approaches for this kind of well-conditioned problems does not report any benefit, as the reduction in the number of Krylov iterations does not compensate the much higher cost per iteration. Such well-conditioned and "medium-sized" problems can be solved faster

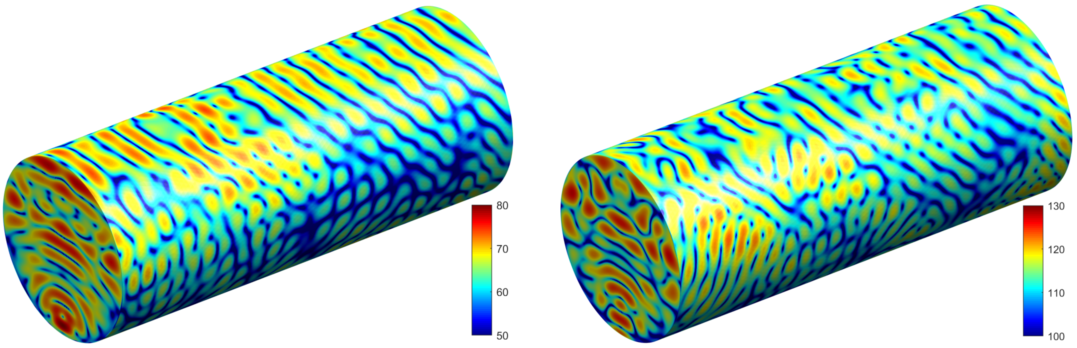

Figure 3.7: Equivalent electric (left) and magnetic (right) currents ($dB\mu A/m$) induced on the surfaces of the domain decomposed dielectric cylinder.

using MLFMA or MLFMA-FFT, provided they are properly parallelized to benefit from the availability of many parallel cores.

Next, a dielectric slab is considered with 12 x 12 x 0.25 m^3 and a relative permittivity and permeability of $\epsilon_r = 2$ and $\mu_r = 1$. The excitation is an oblique plane wave with incident angles $\theta_{inc} = 45°$ and $\phi_{inc} = 0°$ and $\hat{\theta}$ polarized at the frequency 300 MHz. A total of 7 381 344 unknowns are applied to model the equivalent electric and magnetic currents on the slab surfaces. The dielectric slab is divided into nine mosaic-like subdomains, as shown in Fig. 3.10. Also in this case the subdomains are open, which is not an inconvenience to obtain proper local solutions through the JMCFIE formulation. As an example, consider the first subdomain, in the upper right corner, which is represented in more detail in the inset. The subdomain is build up as $D_1 = S_1 \cup \Gamma'_{12} \cup \Gamma'_{14} \cup \Gamma'_{15}$, while the augmented (actually solved) subdomain is $D'_1 = S_1 \cup \Gamma'_{12} \cup \Gamma'_{21} \cup \Gamma'_{14} \cup \Gamma'_{41} \cup \Gamma'_{15} \cup \Gamma'_{51} \cup \Gamma'_{24} \cup \Gamma'_{42}$. The other subdomains and augmented subdomains are constructed similarly. The induced electric and magnetic current densities are shown in Fig. 3.7, where no artifacts are observed around the tearing lines, with the current density flowing perfectly across the different subdomains. Regarding convergences, in Fig. 3.12, conclusions similar to those of the previous example can be drawn: with the DDM solution the number of iterations is drastically reduced, although the wall-clock time is higher for these homogeneous, well-conditioned problems. Nevertheless, the above two examples demonstrate the validity of the tearing-and-interconnect approach to subdivide the solution of homogeneous dielectrics without need of defining artificial surfaces to close the subdomains. Several challenging problems with extremely multiscale features are shown in Chapter 5 to illustrate the capability of the proposed domain decomposition method.

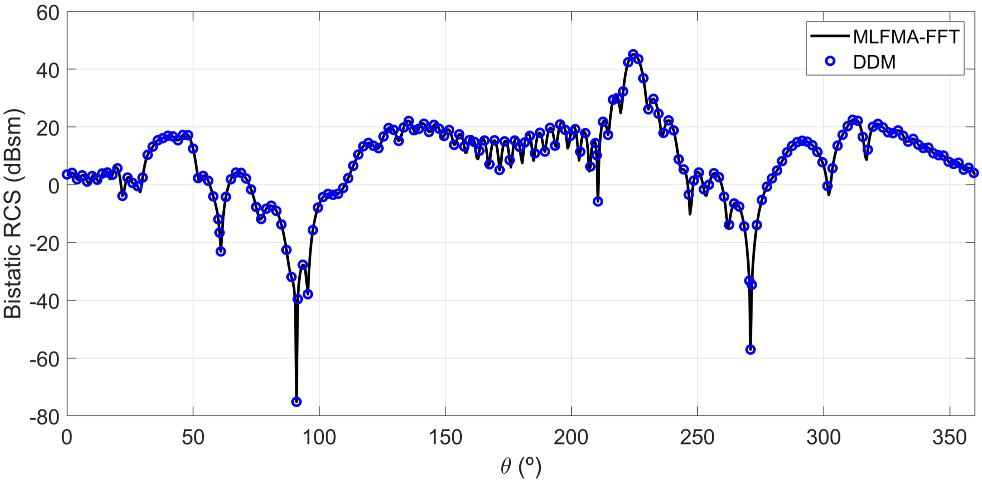

Figure 3.8: Radar cross section of the domain decomposed dielectric cylinder.

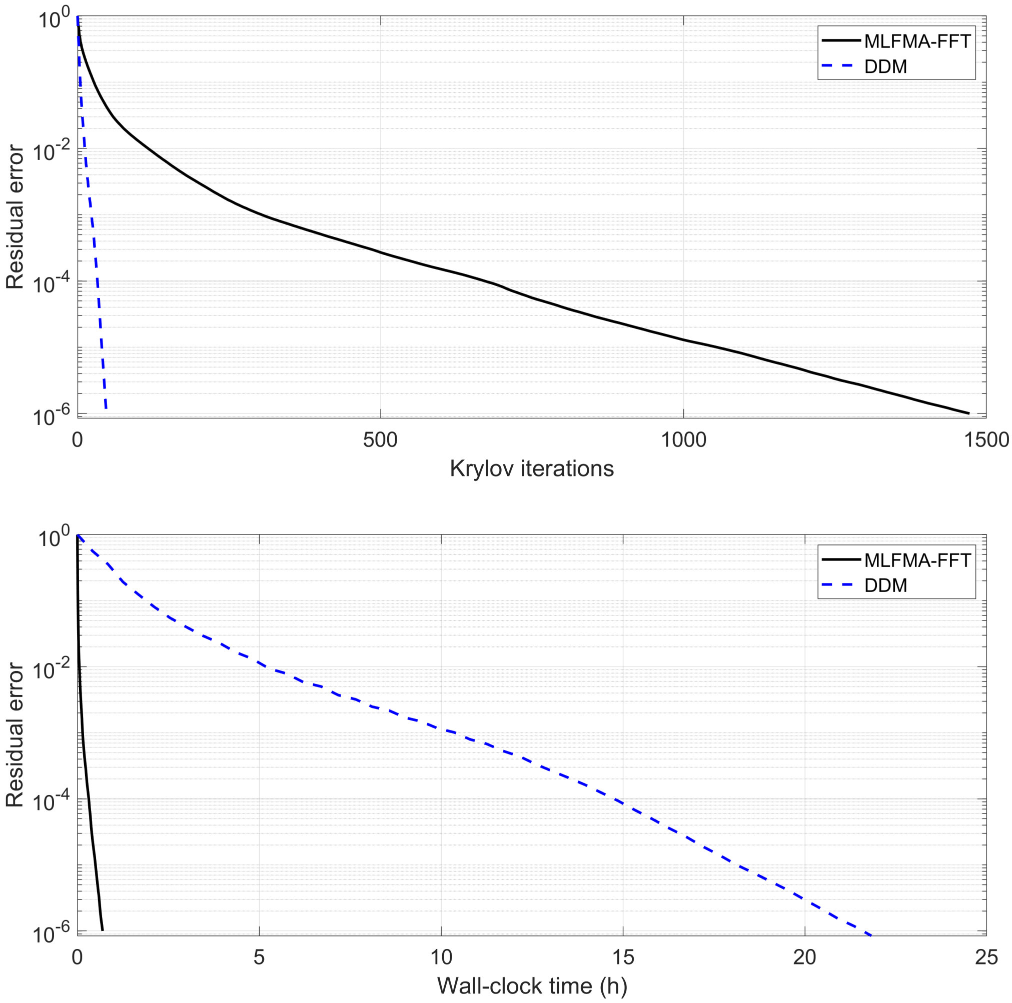

Figure 3.9: Iteration count and wall-clock time for the dielectric cylinder.

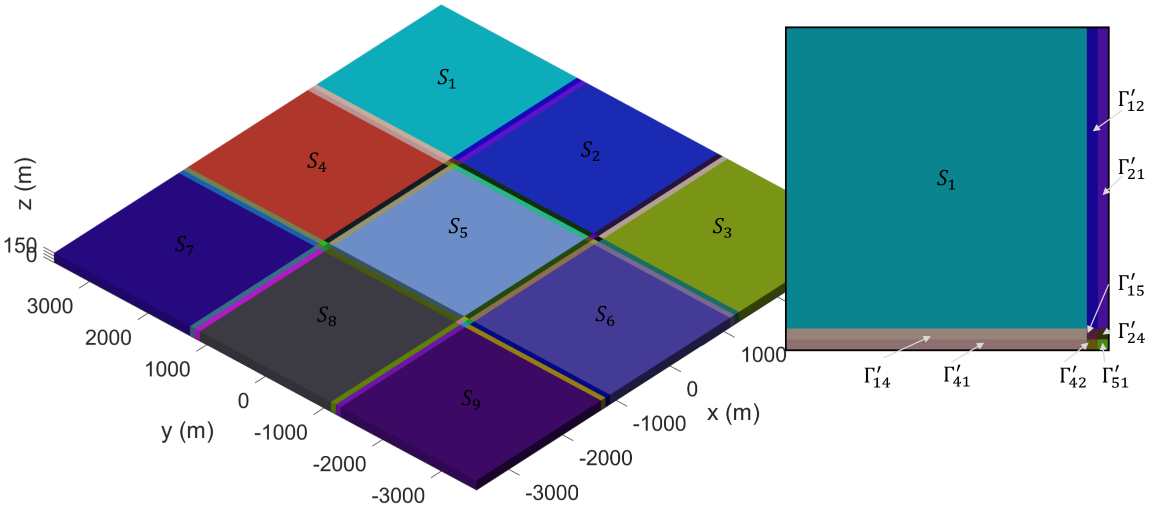

Figure 3.10: Partition of a dielectric plate into subdomains.

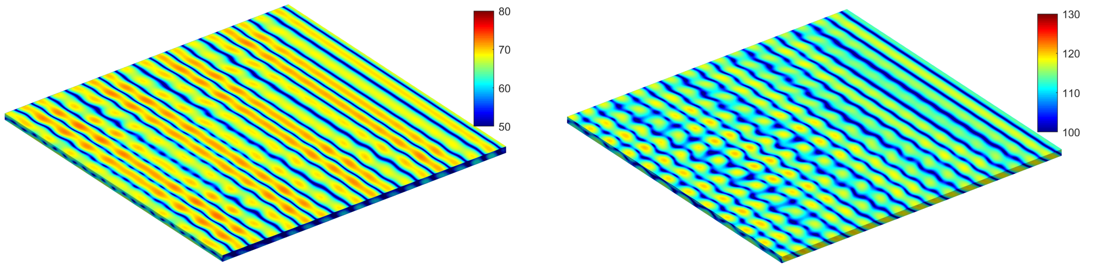

Figure 3.11: Equivalent electric (up) and magnetic (down) currents ($dB\mu A/m$) induced on the surfaces of the domain decomposed dielectric plate.

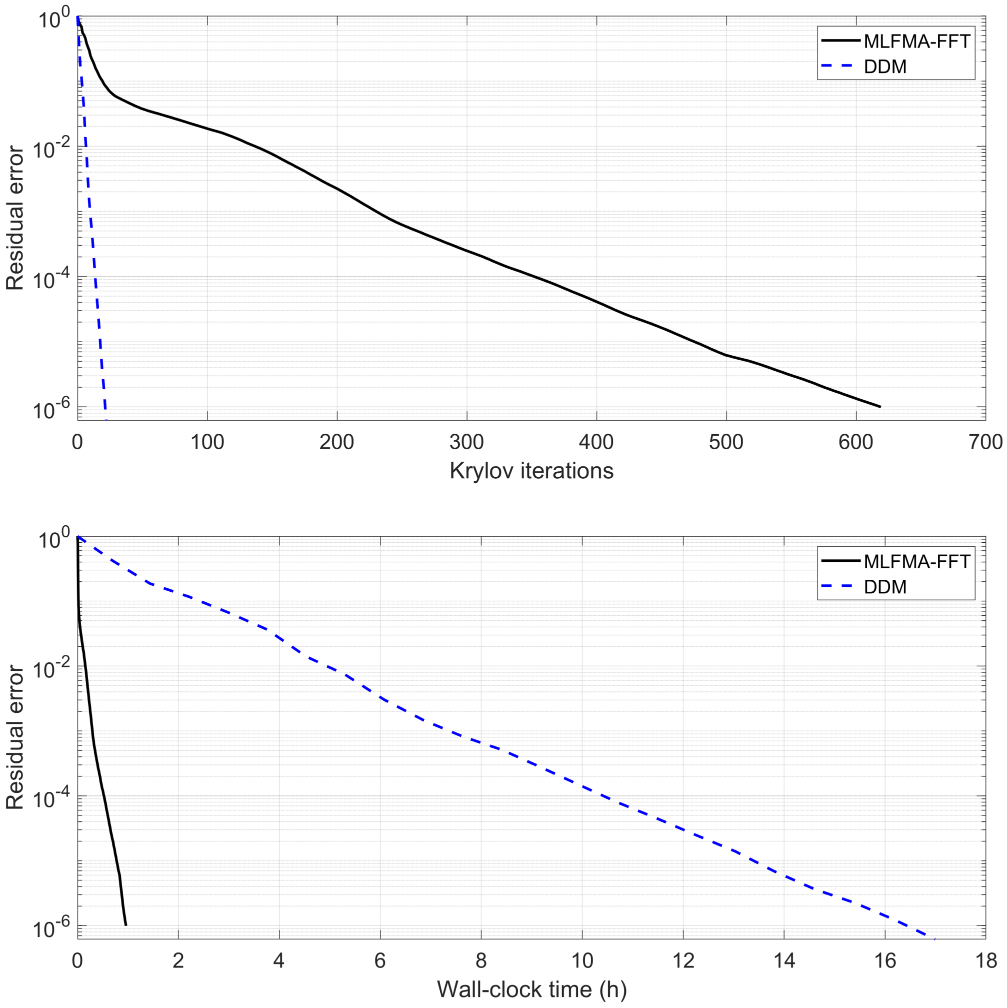

Figure 3.12: Iteration count and wall-clock time for the dielectric plate.

3.3 Highly Scalable Preconditioners

As previously mencioned, solving the DDM preconditioned problem stated in involves the resolution of the subdomain matrix systems. The physical properties of the different parts of the geometry in a really complex system plays a fundamental role in the selection of the optimal DDM domains to improve the outer convergence of the method. However, the optimization of the outer iterative method in the DDM scheme results in a complexity shift towards local solvers, which must lead with inner strong interactions and multi-scale features like cavities or arrays of antennas. In this cases, the inclusion of a efficient preconditioner to improve the fast solvers in the local step improve the general performance of the method or even is needed to achieve the correct results in really challenging methods.

In this section, a high scalability implementation of the MR preconditioner is developed in combination with the MLFMA-FFT in order to build a local solver able to address complex multi-scale domains exhibiting deep multi-scale nature. The MR preconditioner, alone and combined with LU preconditioner, is then judiciously embedded into the formulation described in Chapter 2, rendering a vast improvement of the matrix system conditioning by accurately handling multi-scale mesh features in different levels of detail. A novel and more versatile formulation of the hierarchical MR preconditioner using non-conformal meshes is included in the next sections.

3.3.1 The Multiresolution preconditioner

The multiresolution (MR) preconditioner [56] improves the spectral properties of the original MoM matrix system by splitting the unknown current into solenoidal and non-solenoidal parts. The procedure is divided into different steps. First, the input triangular mesh, supporting the discretization of the problem in terms of standard RWG basis functions, is rearranged until getting a set of meshes with different mesh-element (cell) sizes. This is done via a multilevel algorithm in which the adjacent cells of the previous level, starting from level-0 triangular facets, are aggregated giving rise to macro-cells. The generalized RWG (gRWG) functions are then defined on each pair of adjacent macro-cells, and the associated unknown current is divided into solenoidal and non-solenoidal parts as detailed in [56, 86]. This process poses the MR basis functions of each level. The above scheme is applied recursively down to the quasi-Nyquist (coarsest) cell-size level, where gRWGs are defined completing the set of multilevel basis functions.

The above MR functions at the intermediate (detail) levels and gRWG functions at the coarsest level can be described as linear combinations of the initial underlying RWG functions. Thereby, the MoM system matrix $\mathbf{Z}$ in the space of the initial RWG basis functions can be expressed in the new functions by simply applying a change-of-basis matrix $\mathbf{T}$, as follows:

$$\hat{\mathbf{Z}} = \mathbf{T} \cdot \mathbf{Z} \cdot \mathbf{T}^T = \begin{pmatrix} \hat{\mathbf{Z}}_{MR} & \hat{\mathbf{Z}}_{MR,gRWG} \\ \hat{\mathbf{Z}}_{gRWG,MR} & \hat{\mathbf{Z}}_{gRWG} \end{pmatrix} \tag{3.8}$$

where the matrix $\mathbf{T}$ is made up of two different blocks:

$$\mathbf{T} = [\mathbf{T}_{MR}, \mathbf{T}_{gRWG}]^T \tag{3.9}$$

being $\mathbf{T}_{MR}$ the sub-matrix describing the set of N_{MR} basis functions defined at detail levels, and $\mathbf{T}_{gRWG}$ the sub-matrix with the set of N_{gRWG} functions at the coarsest level, where $N_{MR} + N_{gRWG} = N$, i.e. the total number of unknowns.

Next, a diagonal preconditioner (DP) $\mathbf{D}$ is applied to the MoM matrix in the new multilevel basis, whose elements are given by:

$$D_{ii} = \frac{1}{\sqrt{\hat{Z}_{ii}}}, \quad i = 1, \ldots, N \tag{3.10}$$

The matrix block corresponding to the gRWG functions at the coarsest level ($\hat{\mathbf{Z}}_{gRWG}$ in Eq. (3.8)) is further preconditioned in terms of its incomplete LU factorization [53], which can be denoted as:

$$\mathbf{D}_{gRWG} \cdot \hat{\mathbf{Z}}_{gRWG} \cdot \mathbf{D}_{gRWG} \approx \mathbf{L} \cdot \mathbf{U} \tag{3.11}$$

where $\mathbf{D}_{gRWG}$ is the portion of $\mathbf{D}$ corresponding to the gRWG functions at the coarsest level and $\hat{\mathbf{Z}}_{gRWG}$ is the gRWG matrix block of $\hat{\mathbf{Z}}$.

It is worth mentioning that a naive implementation of the above LU preconditioner would compromise the scalability on mixed-memory architectures, burdening the communications between distributed processes and drastically reducing efficiency. In this thesis, a very efficient implementation of this operation is proposed taking advantage of the highly localized and hierarchic nature of the new set of basis functions.

At this point, the MR preconditioner is applied to the MLFMA method described in Chapter 2 in order to accelerate the solution (convergence) of the dense matrix system resulting in the MoM (2.19). The application of the MR preconditioner can be achieved through a change of basis matrix properly applied to the MoM system. This change of bases can be efficiently applied through two sparse matrix vector products

(SpMVP) before and after the MLFMA main MVP as

$$\begin{aligned}
&\sum_{n=1}^{N}\sum_{i=1}^{N}\sum_{j=1}^{N} T'_{mi} Z_{ij} T'^{T}_{nj} \hat{J}_n \\
&= \sum_{i=1}^{N} T'_{mi} \sum_{q\in B_p}\sum_{j\in G_q} Z_{ij} \sum_{n=1}^{N} T'^{T}_{nj} \hat{J}_n + \sum_{i=1}^{N} T'_{mi} \\
&\cdot \left(\frac{-jk}{4\pi}\right)^2 \int_{S^2} \mathbf{V}_{ip} \sum_{q\notin B_p} \alpha_{pq}(k, \mathbf{r}_{pq}) \sum_{j\in G_q} \mathbf{V}_{qj}(\hat{k}) \\
&\sum_{n=1}^{N} T'^{T}_{nj} \hat{J}_n d^2\hat{k}, m \in G_p
\end{aligned} \tag{3.12}$$

where $\mathbf{T}' = \mathbf{D} \cdot \mathbf{T}$ is the sparse change-of-basis matrix including the DP of Eq. (3.10).

The integration of the MR preconditioner with the MLFMA must be addressed carefully, as operating with large sparse matrices, such as those involved in the MR approach, could create a significant computational bottleneck in parallel deployment.

A simplified notation for the accelerated MVP in (2.39) is consided as:

$$\mathbf{y} = \left(\mathbf{Z}^{near} + \mathbf{Z}^{far}\right) \cdot \mathbf{I} \tag{3.13}$$

where the product by $\mathbf{Z}^{near}$ on the right hand side (RHS) denotes the near-field contributions (adjacent groups) to the MVP, and the product by $\mathbf{Z}^{far}$ denotes the far (non adjacent groups) contributions calculated via MLFMA-FFT as explained in Chapter 2. These contributions correspond to the first and second terms of the RHS in (2.39) respectively. $\mathbf{I}$ is the vector with the N unknown coefficients of the expansion of the current density $\mathbf{J}$ (in the original RWG space), and $\mathbf{y}$ is the vector resulting from the MVP.

The above MVP is called in the framework of the parallel iterative solving of the dense matrix system. Applying the MR preconditioner requires GMRES to operate in the subspace of the new set of MR basis functions, where the MVP in (3.12) should be applied instead of (2.39). Considering that MR hierarchical bases can spread beyond the boundaries of individual MLFMA octree groups at the finest level, a naive implementation of (3.12) could easily burden the parallel numerical computation. The inclusion of the preconditioner was resolved in this thesis by incorporating two additional SpMVPs in (3.13), as follows:

$$\hat{\mathbf{y}} = \mathbf{T}' \cdot \left(\mathbf{Z}^{near} + \mathbf{Z}^{far}\right) \cdot \mathbf{T}'^{T} \cdot \hat{\mathbf{I}} \tag{3.14}$$

where $\hat{\mathbf{I}}$ is the vector with the unknown coefficients of the expansion of the current density $\mathbf{J}$ in the new set of (MR+gRWG) bases, and where

$$\hat{\mathbf{y}} = [\hat{\mathbf{y}}_{MR}, \hat{\mathbf{y}}_{gRWG}]^T \tag{3.15}$$

is the resulting MVP in the MR subspace, with $\hat{\mathbf{y}}_{MR}$ the part corresponding to the MR functions defined at the detail levels and $\hat{\mathbf{y}}_{gRWG}$ the part corresponding to the gRWG functions at the coarsest level.

Next, the LU preconditioner defined in Eq. (3.11) is applied to the gRWG part of the MVP resulting from Eq. (3.14), as

$$\hat{\mathbf{y}}_{gRWG}^{\mathrm{ILU}} = (\mathbf{L} \cdot \mathbf{U})^{-1} \cdot \hat{\mathbf{y}}_{gRWG}. \tag{3.16}$$

Only the gRWG bases contained in the original MLFMA near-field matrix are considered, by applying (3.8) to $\mathbf{Z}^{near}$, which is calculated for the initial RWG basis functions at the finest level of the MLFMA octree (i.e., $\hat{\mathbf{Z}}^{near} = \mathbf{T} \cdot \mathbf{Z}^{near} \cdot \mathbf{T}^T$). Subsequently, (3.11) is applied to the gRWG block of $\hat{\mathbf{Z}}^{near}$ ($\hat{\mathbf{Z}}^{near}_{gRWG}$). This maximizes data locality and the efficiency of the parallel implementation, albeit at the expense of limiting the interactions between gRWG functions to those available in MLFMA, resulting in incomplete LU (ILU) factorization. In the proposed implementation, this implies that there may even be pairs of gRWG functions that are partially computed in the LU preconditioner, since not all the partial contributions of the RWGs that make up these macrobases are available in $\mathbf{Z}^{near}$.

The above formulation has the advantage of applying MLFMA-FFT in the initial RWG subspace, where its parallel performance is optimized, while GMRES operates in the preconditioned MR subspace. Importantly, the two additional SpMVPs involved in Eq. (3.14) and subsequent application of the ILU preconditioner have been accelerated and judiciously embedded into the MLFMA-FFT parallel implementation. All the required sparse matrices ($\mathbf{T}'$, $\mathbf{Z}^{near}$ and $\hat{\mathbf{Z}}^{near}_{gRWG}$) are stored in compress sparse row (CSR) format. Efficient algorithms have been developed for the SpMVP parallel computation using OpenMP (this also applies to the near-field calculation of the MVP in the RWG subspace in Eq. (3.14), i.e., $\mathbf{Z}^{near} \cdot (\mathbf{T}'^T \cdot \hat{\mathbf{I}})$. Instead of the usual octree-group parallelization, a SpMVP is used to avoid memory overlapping, so only the CSR sparse version of this matrix is stored). Additionally, $\hat{\mathbf{Z}}^{near}$ is never fully calculated, as only the diagonal and the gRWG block of this matrix are needed. Effective parallel algorithms have been developed for the calculation of both elements.

The efficient implementation of the ILU preconditioner is, however, somewhat more cumbersome, as the ILU preconditioner is not naturally prone to parallelization. Naive implementations generally suffer from heavy inter-process communication overhead, resulting in very inefficient parallel performance. This lack of scalability can be overcome in the present case by applying the parallel sparse direct and multi-recursive iterative linear solver (PARDISO), available in the Intel Math Kernel Library (MKL) [87]. The pipelining parallelism of this implementation combined with the strong sparsity and local dependencies of the new set of hierarchical functions with respect to the initial RWGs, allow efficient parallel computation of $(\mathbf{L} \cdot \mathbf{U})^{-1}$ in multicore computers, avoiding the bottleneck normally involved when applying the ILU preconditioner in large-scale parallel calculations.

3.3.2 Validation and application

In this section, the effectiveness of the multiresolution preconditioner implementation is illustrated for solving realistic large-scale radiation problems to demonstrate the capability of this efficient preconditioner to solve extremely complex local problems in a DDM scheme.

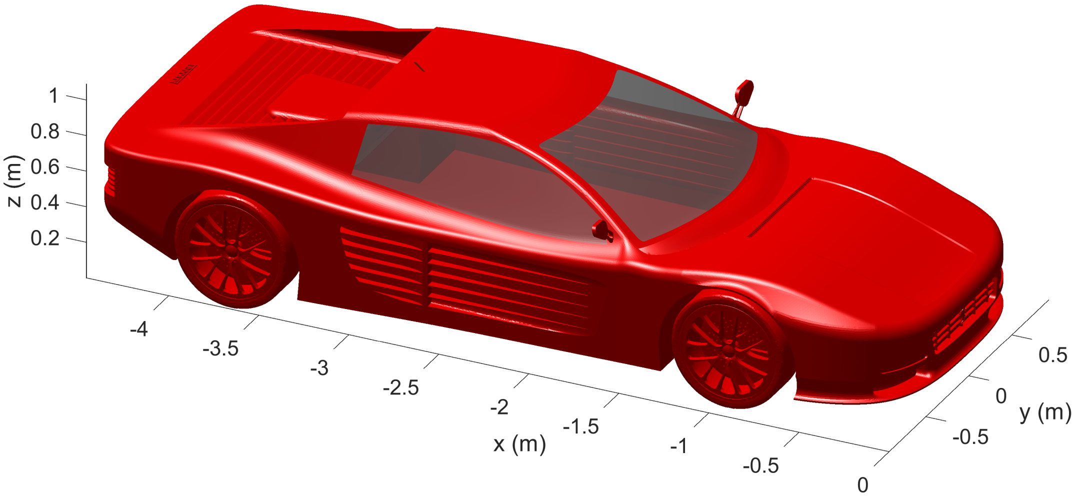

Figure 3.13: Ferrari Testarossa CAD model with a shark monopole strip antenna.

A challenging structure consisting of a Ferrari Testarossa is considered next, as shown in Fig. 3.13. This structure exhibits deep multi-scale nature, combining smooth surfaces with different levels of details distributed throughout the structure: on the sides of the doors, front and rear grills, rear cover, wheels, shock absorbers, and the exhaust pipes. To test the proposed method the calculation of a radiation problem for a shark-type antenna located in the ceiling is considered. The problem is solved by MLFMA using the EFIE formulation for the entire structure. The excitation consists of an extended delta-gap applied to the base of the shark-type antenna. The frequency was set to 900 MHz, and an average mesh size of $\lambda/20$ was set to the smooth parts, while a fine enough meshing (up to $\lambda/500$ in some parts) was applied to properly model the small details, which clearly reveals the multi-scale nature of this example, yielding a total of 1 051 408 unknowns. The simulations were calculated on an Intel(R) Xeon(R) E7-8867 v3 computing server using 32 cores.

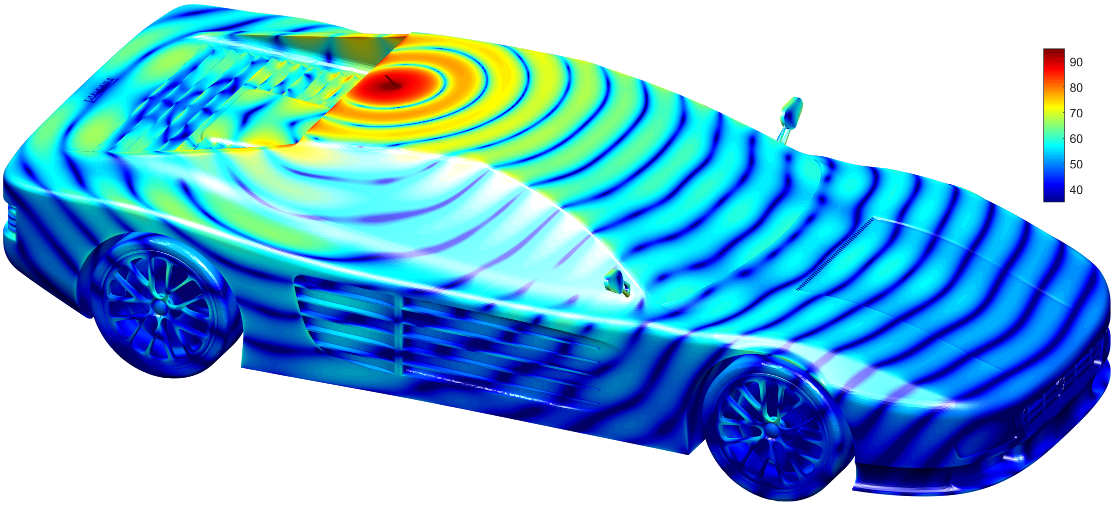

Figure 3.14: Real part of the equivalent electric surface current distribution ($dB\mu A/m$) induced on the Ferrari Testarossa.

The proposed MLFMA-MR-LU is compared to MLFMA-MR, the conventional ILU preconditioning applied to the whole problem using RWG basis functions (indicated MLFMA-ILU), and a raw solution using RWG without preconditioning at all (indicated MLFMA). Importantly, given the large size of the problems posed, the gRWG matrix in MR-LU is stored in CSR format and ILU factorization is accelerated and parallelized throughout PARDISO routines, which are available from the Intel Math Kernel Library. Sparse storage and PARDISO factorization and solving are also applied to the conventional ILU preconditioning. This enables these ILU based preconditioners to be used in the large examples posed, which would otherwise be intractable due to computational burden.

The equivalent electric currents induced on the structure are shown in Fig. 3.14. Figure 3.15(a) shows the convergence of the relative residual error to reach these currents with the number of Krylov iterations. It can be observed that both the MLFMA-MR-LU and MLFMA-ILU approaches outperform MLFMA and MLFMA-MR, reaching residual errors below 10^{-6} in around 1500 iterations. Nevertheless, it must be remarked that the time per iteration is different in each preconditioner. Consequently, a better figure of merit is the wall-clock time, defined as the time to solve the complete problem, which is shown in Fig. 3.15(b). From these curves it can observed that MLFMA-MR-LU is by far the preconditioner that provides the fastest convergence, reaching the prescribed relative error in little more than half an hour. This contrasts with the wall-clock time convergence of the other solutions, which remains above a relative error of 10^{-3} after one hour and a half.

In view of the preceding results, it can be summarized that MLFMA-MR-ILU constitutes the best approach of those tested to deal with this kind of multi-scale

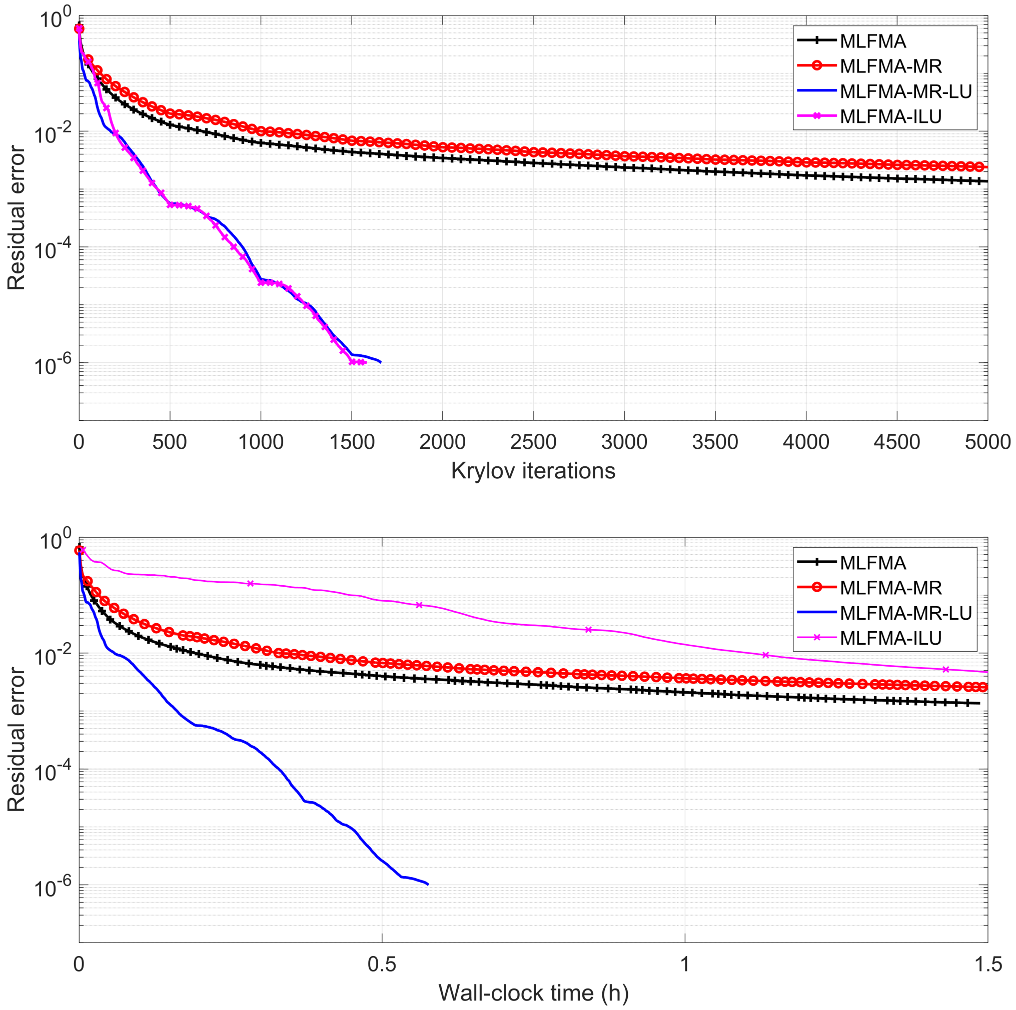

Figure 3.15: teration count and wall-clock time for the radiation of the Ferrari Testarossa proposed in the Fig. 3.13

problems, providing an efficient preconditioner for the acceleration of the local solution of large domains in the proposed DDM.

Chapter 4

Non-conformal SIE Methods

Contenido

In Chapter 3, the DDM approach proposed in this thesis was presented as a powerfull tool to deal with multiscale problems. However, in the case of very large and complex problems, a more efficient handling of the different subsystems in which the problem is decomposed, which does not require conformal discretizations in the connections along the different subdomains, is still lacking. This chapter focuses on applying and envisioning new cutting-edge SIE non-conformal techniques, to improve the usability and versatility of the DDM framework in quite complex scenarios without compromise accuracy and efficiency. The Discontinuos Galerkin method is formulated for the first time in combination with the JMCFIE formulation for arbitrary non-conformal composite problems. A study of the influence of the interior penalty stabilization parameter on the performance of the method for this new type of problem in the scope of DG is also included. Next, the novel multibranch basis functions are introduced and combined with the multiresolution preconditioner for the fast solution of quasi-non-conformal problems exhibiting deep multiscale features. This will enable for the first time the application of quasi Helmholtz preconditioners using non-conformal meshes. Several numerical examples are shown to demonstrate the capabilities of the proposed methods and the convenience of their inclusion in the DDM framework.

4.1 Introduction

The extension of the surface integral equations to non-conforming meshes has ignited intense research in the last years, with the goal of finding versatile and accurate methodologies to address large and multi-scale complex problems while simplifying the otherwise necessary computer-aided-design generation and meshing processes.

Moreover, the extremely different levels of details depending on the working frequencies and the proper addressing of the geometrical tends to greatly increase the number of unknowns when leading with real life problems. In this context, h-refinement techniques work to develop methods capable of incresing the accuracy of the SIE solution for coarse-meshed multiscale problems through local mesh refinement.

Discontinuous Galerkin implementations of the SIE [50, 88–92], based on the combination of the half-Rao-Wilton-Glisson basis functions with an interior penalty term, are one of the most popular approaches to deal with this kind of problems. Those methods were first proposed for the solution of the time-domain Maxwell's equations using the finite element method [93–97]. Recently, they have been extended to the SIE formulations for nonpenetrable objects [88–91], impedance boundary condition (IBC) objects [98, 99], and homogeneous penetrable objects [92]. The allowance of discontinuous and possibly unstructured nonconformal meshes renders this method as a very versatile and effective tool to handle problems with very different geometrical scales and details. For example, the different subsystems of a larger, more complex problem can be independently modeled, meshed and assembled back together to form a whole connected body, without caring about mesh conforming or the presence of spurious slits and overlaps due to slight missplacement between subsystems at the tear contours. This greatly simplifies the CAD generation and meshing processes. Specifically, achieving current continuity across the DG-treated tear lines paves the way for the implementation of simple and scalable domain decomposition Schwarz preconditioners, which significantly reduce the condition number and iteration count in problems including geometrical features at very different scales.

The key to these methods lies in the careful treatment of charge accumulation at the (non-conforming) boundaries between the h-RWG basis functions. This is done through the incorporation of an IP and the appropriate selection of a stabilization parameter, closely relate to the triangular mesh size. Other non-conforming SIE schemes alternative to DG that avoid the inclusion of an IP term (and the involved singular integrals) are the monopolar-RWG basis functions [100–105], based on the addition of artificial testing surfaces or the use of volumetric testing integrals.

More recently, a different approach has been introduced based on the use of the so-called multi-branch RWG basis functions [71]. These functions are defined over non-conforming triangles sharing a common tearing line, with the only restriction that the nodes of the coarser mesh at the tearing line are consistent with part of the nodes of the finer mesh (i.e, the mesh must be partially node-conforming). This is the type of meshing emerging after h-refinements, so the MB-RWG basis functions are especially suited to this problem. But they also bring other advantages. In particular, they can be easily integrated into existing RWG-based SIE codes without the need of including penalty terms, additional volumetric integrals or artificial surfaces, while still simplifying the CAD and mesh generation. Additionally, MB-RWG are div-conforming functions, which has allowed the derivation of loop (solenoidal) bases as linear combination of them [106].

Regardless of the meshing and basis functions applied, as it is mencioned in Chapter 1, SIE methods suffer from ill-conditioning when applied to realistic high-fidelity models that include multi-scale features, making their resolution challenging. The use of physics-based preconditioners such as the multiresolution preconditioner (described in Chaper 3) allows to significantly improve the convergence and iterations count in these problems. However, despite recent efforts to improve the capabilities of DG-SIE methods, to date the application of physics-based preconditioners is limited to conforming schemes such as those relying on the use of RWG basis functions. This is, in part, due to the non div-conforming properties of the h-RWG functions.

In this context, the use of a set of div-conforming functions defined over (possibly) non-conforming meshes and combined with physics-based preconditioners would bring a very appealing advantage, posing a good compromise between performance and versatility in electromagnetic modelling of complex geometries with multi-scale features.

4.2 Discontinuous Galerkin

4.2.1 Formulation

Starting from the matrix system provided by the discretization of the JMCFIE formulation (2.19) (described in Chapter 2) and considering a piecewise homogeneous penetrable object in a homogeneous (unbounded) medium, DG is applied to the collection of surfaces S_{ij} composing the entire problem. To provide the greatest versatility in preparing and solving challenging problems, each surface S_{ij} can be decomposed into one or more nonoverlapping surfaces $\mathcal{S}_k$, in which conformal discretizations are applied, while allowing nonconformal meshes across the tear lines and junctions between different surfaces. This decomposition and the corresponding notation are indicated in Figure 4.1. In general, it can be writen:

$$S_{ij} = \bigcup_k \mathcal{S}_k \tag{4.1}$$

Conventional (normal-continuous) RWG basis functions are considered to represent the currents within the $\mathcal{S}_k$ conformal-meshed surfaces. At the nonconformal tear contours between them, half-RWG basis functions, also named as monopolar-RWG [100] or $\mathbf{L}^2$ basis functions [88], are applied. Taking into account that these are non-div-conforming functions, the normal continuity constraint is broken across the tear lines. This continuity will be *weakly* restored by applying the DG formulation, as described next.

First, equations (2.33) and (2.35) involving operator $\mathcal{L}$ for the tangential and normal equations respectively must be developed. As $\mathcal{K}$ is a Fredholm integral operator of the second kind, it is not naturally concerned by the lack of normal continuity. Equation (2.33) involves hyper-singular integrals, whose singularity order can be reduced in terms of the product rule for divergence and the divergence Gauss theorem, by transferring the gradient operators from the Green's function and the scalar potential (last term in (2.5)) to the divergence of the basis and testing functions in (2.33). Thus it can be written

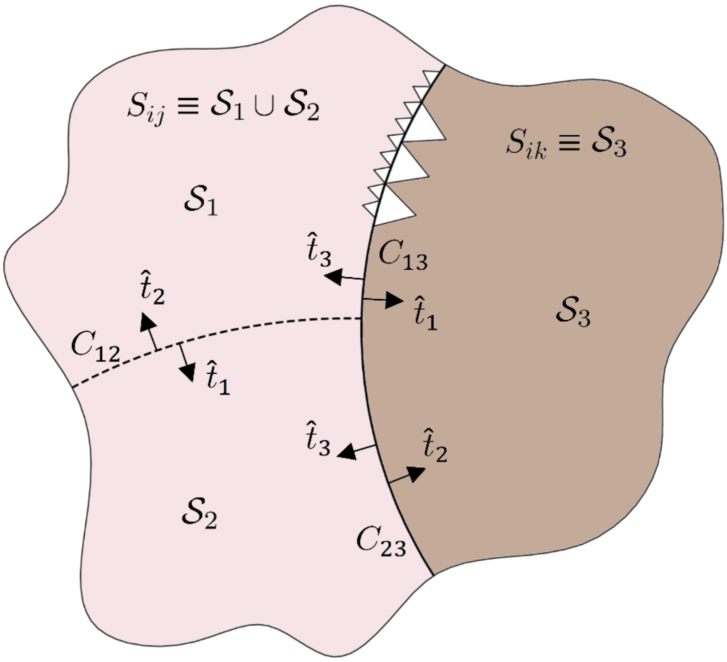

Figure 4.1: Decomposition of the boundary surfaces and interfaces of the composite object. Notation used for Discontinuous Galerkin. Interface S_{ij} between regions R_i and R_j is decomposed into two nonoverlapping surface pieces, $S_{ij} = \mathcal{S}_1 \cup \mathcal{S}_2$, yielding the tear contour C_{12}. Interface S_{ik} separating regions R_i and R_k is modeled by surface $\mathcal{S}_3$. Conformal meshes are applied inside surfaces $\mathcal{S}_k$, $k = 1..3$, while nonconformal meshes are allowed in the tear contour C_{12} and multi-material junction contours C_{13} and C_{23}.

$$\begin{aligned}
A^i_{mn} = & \int_{\Delta_m} \mathbf{f}_m \cdot \mathcal{L}_i(\mathbf{f}_n) dS = \\
& \int_{\Delta_m} \mathbf{f}_m \int_{\Delta_n} \mathbf{f}_n g_i(\mathbf{r}, \mathbf{r}') dS' dS \\
-\frac{1}{jk_i} \Bigg[& \int_{\Delta_m} \nabla \cdot \mathbf{f}_m \int_{\Delta_n} \nabla' \cdot \mathbf{f}_n g_i(\mathbf{r}, \mathbf{r}') dS' dS \\
- & \int_{\Delta_m} \nabla \cdot \mathbf{f}_m \oint_{\partial S_n} \hat{m}_n \cdot \mathbf{f}_n g_i(\mathbf{r}, \mathbf{r}') d\partial S' dS \\
- & \oint_{\partial S_m} \hat{m}_m \cdot \mathbf{f}_m \int_{\Delta_{n|i}} \nabla' \cdot \mathbf{f}_n g_i(\mathbf{r}, \mathbf{r}') dS' d\partial S \\
+ & \oint_{\partial S_m} \hat{m}_m \cdot \mathbf{f}_m \oint_{\partial S_n} \hat{m}_n \cdot \mathbf{f}_n g_i(\mathbf{r}, \mathbf{r}') d\partial S' d\partial S \Bigg]
\end{aligned} \tag{4.2}$$

where ∂S_m denotes the line contour of function subdomain Δ_m, and $\hat{m}_m$ is the corresponding in-plane outgoing unit vector orthogonal to ∂S_m. The last three terms on the right hand side of (4.2) involving line integrals vanish in the case of using div-conforming basis and testing functions, as is the case with RWG basis/testing functions. Otherwise, charges may accumulate on the edges where the normal component of the basis and testing functions do not vanish, as is the case with half-RWG functions. Consequently, the last three terms of (4.2) must be accounted for in the formulation when such functions are applied.

Similarly, applying the product rule for divergence, the divergence Gauss theorem and the mixed product identity to transfer the gradient operators from the Green's function and the scalar potential to the divergence of the basis function and the rotated testing function in (2.35)

$$
\begin{aligned}
A'^{i}_{mn} = \int_{\Delta_m} \mathbf{f}_m \cdot \hat{n}_m \times \mathcal{L}_i(\mathbf{f}_n) dS = \\
\int_{\Delta_m} (\mathbf{f}_m \times \hat{n}_m) \int_{\Delta_n} \mathbf{f}_n g_i(\mathbf{r},\mathbf{r}') dS' dS \\
-\frac{1}{jk_i} \Bigg[\int_{\Delta_m} \nabla \cdot (\mathbf{f}_m \times \hat{n}_m) \int_{\Delta_n} \nabla' \cdot \mathbf{f}_n g_i(\mathbf{r},\mathbf{r}') dS' dS \\
- \int_{\Delta_m} \nabla \cdot (\mathbf{f}_m \times \hat{n}_m) \oint_{\partial S_n} \hat{m}_n \cdot \mathbf{f}_n g_i(\mathbf{r},\mathbf{r}') d\partial S' dS \\
- \oint_{\partial S_m} \hat{m}_m \cdot (\mathbf{f}_m \times \hat{n}_m) \int_{\Delta_n} \nabla' \cdot \mathbf{f}_n g_i(\mathbf{r},\mathbf{r}') dS' d\partial S \\
+ \oint_{\partial S_m} \hat{m}_m \cdot (\mathbf{f}_m \times \hat{n}_m) \oint_{\partial S_n} \hat{m}_n \cdot \mathbf{f}_n g_i(\mathbf{r},\mathbf{r}') d\partial S' d\partial S \Bigg]
\end{aligned}
\tag{4.3}
$$

Equations (4.2) and (4.3) correspond to a symmetric DG formulation [88,98]. Using RWG basis and testing functions, all terms on the right hand side of (4.3) vanish except the first and fourth, the fourth posing a line integral along the testing function contour. However, in case of using half-RWG basis and testing functions, the double-line integral of term number five must be taken into account.

All integrals above are bounded and accurately evaluated using the usual singularity extraction or cancellation procedures for RWG basis functions [2, 107], except the double-contour integrals in the fifth terms on the right hand side of (4.2) and (4.3). Those integrals are problematic as they become unbounded when the testing and charge lines coincide, preventing the application of the Galerkin formulation unless they are avoided or treated in some way.

A carefully inspection of those problematic terms reveals that they can cancel each other out in the neighboring (touching) half-RWG functions at the two sides of the tear lines, provided that the continuity of the normal component is enforced. Simply put, those terms essentially contribute to weakly enforce the current continuity across the tear lines, as it suffices to guarantee such continuity to push them to zero. In light of this, they can be omitted from the formulation and replaced by the condition to weakly enforce normal current continuity across adjacent contours, which is much more favorable to evaluate. This condition can be written as follows

$$\hat{t}_k \cdot \mathbf{X}_k + \hat{t}_{k'} \cdot \mathbf{X}_{k'} = 0 \quad \text{on} \quad C_{kk'} \tag{4.4}$$

where $C_{kk'}$ is the tear contour line between adjacent surfaces $\mathcal{S}_k$ and $\mathcal{S}_{k'}$, with C_k the contour line on $\mathcal{S}_k$ and $C_{k'}$ the contour line on $\mathcal{S}_{k'}$. $\hat{t}_k$ is the in-plane outgoing unit vector orthogonal to contour C_k, and $\hat{t}_{k'}$ is the in-plane outgoing unit vector orthogonal to contour $C_{k'}$. This can be written for the discretized problem as

$$\sum_{\substack{\partial S_m \\ \in C_k}} \sum_{\substack{\partial S_n \\ \in C_{k'}}} (\hat{m}_m \cdot \mathbf{f}_m X_m + \hat{m}_n \cdot \mathbf{f}_n X_n) = 0 \text{ on } C_{kk'}, \qquad \mathbf{r} \in \partial S_m \cap \partial S_n \tag{4.5}$$

and introduced into the formulation after adequately weighting with the testing functions as follows

$$\frac{\beta}{jk_i} \sum_{\substack{\partial S_m \\ \in C_k}} \int_{\partial S_m} \hat{m}_m \cdot \mathbf{f}_m \sum_{\substack{\partial S_n \\ \in C_{k'}}} (\hat{m}_m \cdot \mathbf{f}_m X_m + \hat{m}_n \cdot \mathbf{f}_n X_n) d\partial S = 0 \qquad \text{on } C_{kk'}, \mathbf{r} \in \partial S_m \cap \partial S_n \tag{4.6}$$

where X_n stands for the J_n or M_n current coefficients, and β is the so-called interior penalty stabilization parameter [88]. The proper selection of the last parameter, which depends on the mesh size of the discretization, is very important for the convergence of the method. An in-depth study of this parameter will be carried out in the numerical results section.

The above expression is the IP term [88, 92], used to penalize the charge accumulation along the tear contours. This condition is included in the JMCFIE matrix formulation (2.19) by augmenting (2.33) with the following IP term:

$$IP^i_{mn} = \frac{\beta}{jk_i} \int_{\partial S_m} \hat{m}_m \cdot \mathbf{f}_m \; \hat{m}_n \cdot \mathbf{f}_n \; d\partial S \tag{4.7}$$

4.2.2 Multimaterial junctions

In this thesis it is demonstrated that the DG formulation can address nonconformal junctions between interfaces concerning different regions with different materials. This is one of the most challenging issues in the analysis of arbitrary complex composite objects using the SIE-MoM approach, as the imposition of normal current continuity

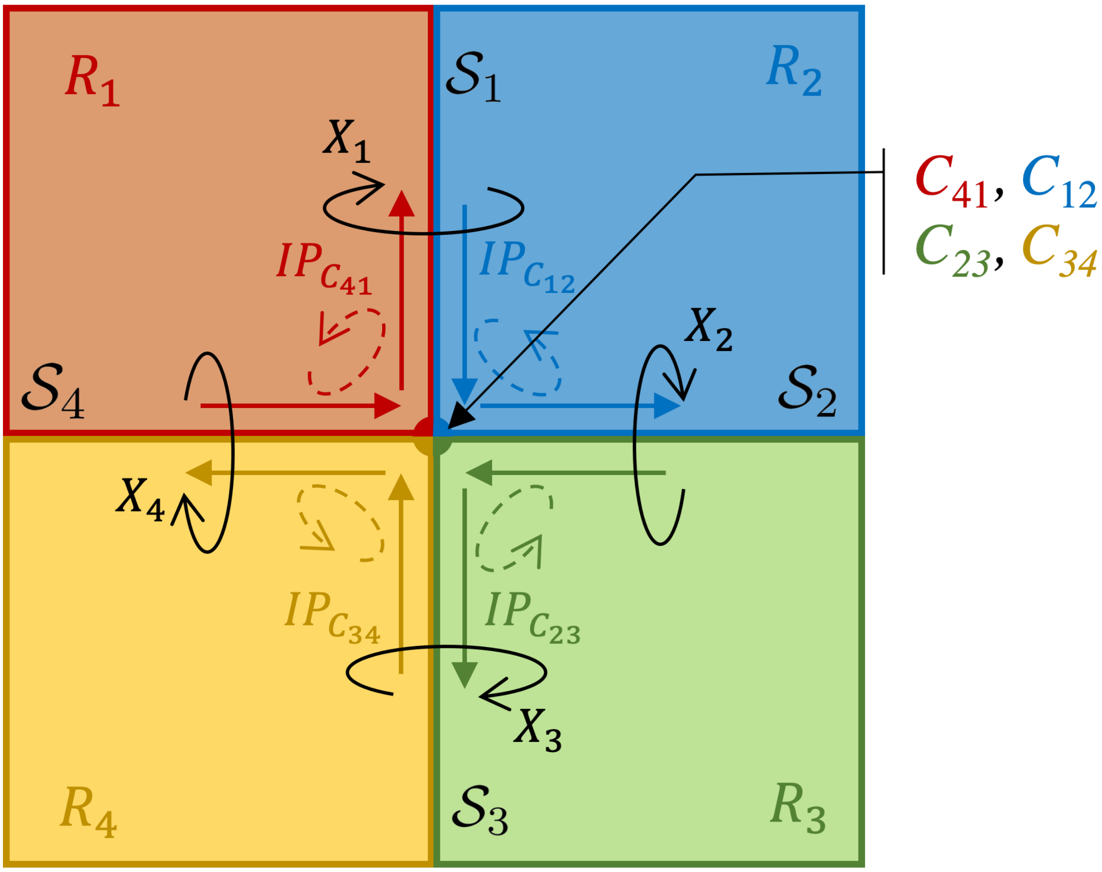

Figure 4.2: Multi-material junction between four regions. Straight dashed lines denote interfaces between regions. The central black point denotes the contour lines between surfaces that meet at the junction. Solid curved arrows denote the boundary conditions implicit in the JMCFIE formulation. Small curved dashed arrows denote interior penalty conditions. The large dashed circular arrow denotes continuity of the normal current across the junction, enforced by the combination of the boundary conditions and the (weakly imposed) interior penalties.

across the entire junction becomes particularly tedious. It usually requires the explicit enforcement of the boundary conditions to combine and remove extra unknowns and equations at junctions [72]. Although the process can be somewhat simplified by using solutions such as the multiregion oriented piecewise basis functions [73], it still requires special treatment and conformed meshes across the junction. Otherwise, the use of non-conforming schemes stands out as a more versatile alternative for modeling highly complex composite objects.

The proposed DG-JMCFIE formulation can be straightforwardly applied to such multi-material piecewise homogeneous problems without any restriction or particular procedure, and without concern for mesh conformity across junction lines. Figure 4.2 shows an example of junction between four different regions R_i, $i = 1..4$, posing four nonoverlapping interfaces S_{12}, S_{23}, S_{34} and S_{14}. Let us assume that these interfaces are meshed separately, resulting in four meshed surfaces $\mathcal{S}_i$ respectively, $i = 1..4$, which may be nonconformal across the junction. Four contour lines between pairs of surfaces that share a region are formed at the junction, namely C_{41}, C_{12}, C_{23} and C_{34}. Each pair of straight arrows entering and leaving the junction represents a half-RWG basis function supporting an unknown X_i, which stands for the current entering or leaving the junction on surface $\mathcal{S}_i$. These coefficients account for the current on both sides of the surface, as they are equal but flow in the opposite direction due to the boundary conditions embedded in the JMCFIE formulation, which are implicitly applied on surfaces $\mathcal{S}_i$ (this fact is denoted by the continuous circular arrows in Fig. 4.2). Therefore, four independent unknowns arise in the junction. To weakly guarantee the normal current continuity throughout the junction, it is sufficient to apply the interior penalty independently to the four contours previously defined within each region (as otherwise is always the case in the tear lines between any non-conforming surfaces), which is denoted as $IP^i_{C_{kk'}}$ (circular dashed arrows in the figure). Remarkably, with this procedure nothing particular is needed for the junction case. The normal current continuity across the whole junction is guaranteed by the combination of the boundary conditions imposed on the surfaces and the interior penalty (weakly) imposed on the contours within each region. All this will be confirmed through the numerical experiments of the next section.

4.2.3 Interior penalty stabilization parameter

The effect of the interior penalty stabilization parameter β (4.7) on the iteration count for problems involving nonconformal and non-uniform meshes at different scales is investigated next. A dielectric cube with 1 m edge size and relative permittivity $\epsilon_r = 2.0$ in vacuum background is considered. The entire surface is partitioned into eight symmetrical surface pieces (defined each in a corner) where conformal meshes are applied, while nonconformal meshes are allowed at the tear contours between them. The inner (conformal meshed) surfaces are modeled using RWG basis and testing functions, while half-RWG are applied in the discontinuous tear lines. Different mesh sizes (h) varying from $h = \lambda/10$ to $h = \lambda/40$ are applied to the different surfaces and/or tear lines, posing a total of nine different combinations. The meshes used in each case are shown as insets in the corresponding results figures. A plane wave impinging in the $-\hat{z}$ direction at a frequency of 300 MHz, with the electric field polarized along the $\hat{x}$ direction, is considered as the excitation.

All problems are solved by MLFMA with the number of unknowns varying from 3 648 to 64 320 unknowns. The raw solution, without preconditioning, is compared to the Jacobi (J), block-Jacobi (BJ) and ILU preconditioners. In each case, the reference is the iteration count obtained for the equivalent conformal problem solved by RWG

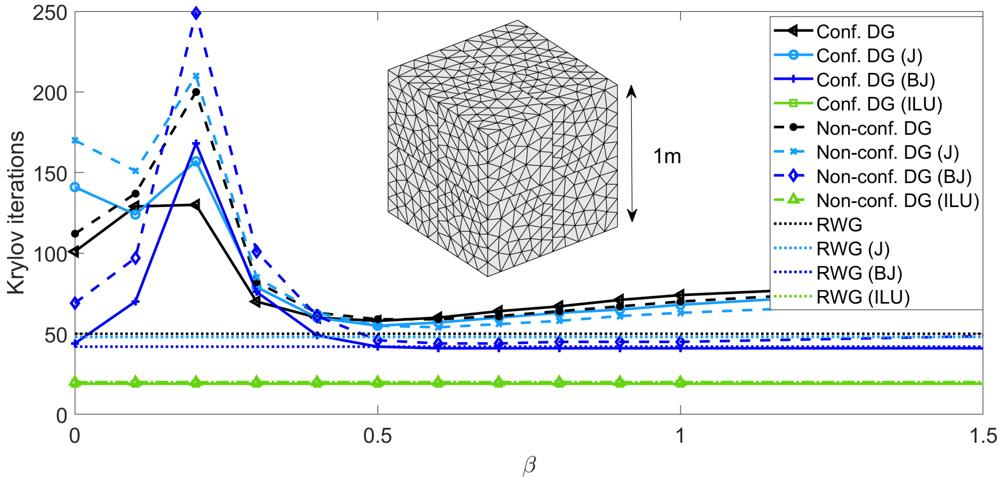

Figure 4.3: Iteration count as a function of β to reach a relative residual error below 10^{-6} for a cube with 1 m edge size and $\epsilon_r = 2.0$ decomposed into 8 surface pieces with uniform mesh size of $h = \lambda/10$.

basis functions using the same preconditioner.

The influence of the mesh size in the case of uniform discretizations is studied, using the same size h for the different surface pieces in which the cube is decomposed. Figure 4.3 shows the number of iterations versus parameter β required to achieve a relative residual error below 10^{-6} for $h = \lambda/10$. Both conformal and nonconformal meshes at the tear lines are considered, on which half-RWG are defined in any case. Looking at the figure, it can be observed that the maximum iteration count is obtained in all cases for IP factors around $\beta = 0.2$. The optimum value of this parameter is found around 0.5, for which the minimum number of iterations to reach the prescribed precision is found for almost all DG solutions. The number of iterations is indeed low, from 42 to 60 depending on the preconditioner. This is merit of using JMCFIE, which combines both tangential and normal equations resulting in a well-conditioned matrix system. An interesting case is that for $\beta = 0$, meaning that no interior penalty is considered at all. Convergence in this singular case is in general poor, except when using block-Jacobi and ILU preconditioners. Remarkably, it can be also observed from Fig. 4.3 that the iteration count in the case of using ILU preconditioner does not depend on the penalty factor, but it is constant and as low as 20 iterations for all values of β. Nevertheless, it is important to note that the application of this preconditioner is computationally more expensive and less effective as the electrical size of the problem increases. Leaving aside the ILU preconditioner, the best iteration count is obtained for block-Jacobi, reaching almost equal convergence to that provided by the conformal reference solution using exclusively RWG functions for the whole problem.

Figure 4.4 shows the results for the previous cube when a uniform denser meshing is applied, with $h = \lambda/20$. Again, both conformal and nonconformal results using

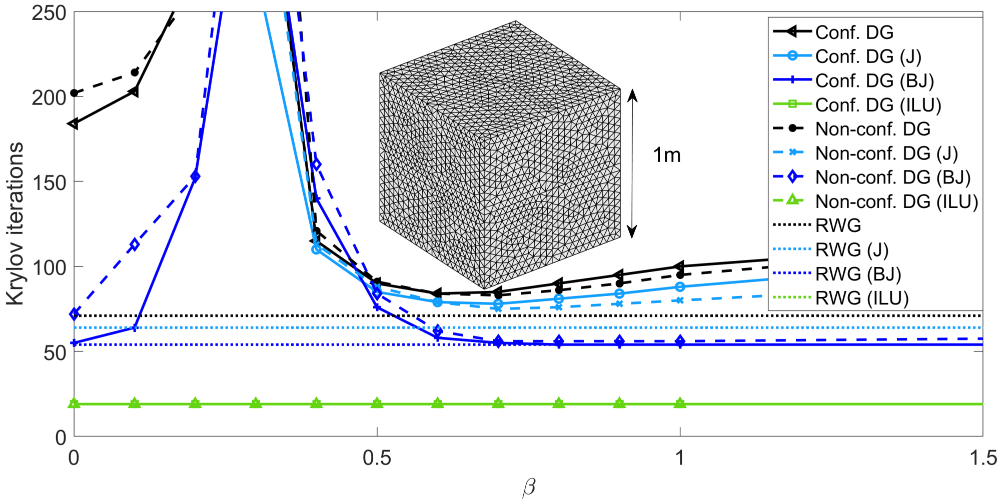

Figure 4.4: Iteration count as a function of β to reach a relative residual error below 10^{-6} for a cube with 1 m edge size and $\epsilon_r = 2.0$ decomposed into 8 surface pieces with uniform mesh size of $h = \lambda/20$.

half-RWGs at contour lines and the different preconditioners are depicted, as well as their respective conformal RWG reference solutions. Looking at this figure, it can be observed a sharper dependence with β, with the iteration counts growing faster as we move away from the optimal value of the interior penalty parameter, which is found around $\beta = 0.7$. The values of this parameter for which the iteration number is maximum move also forward, up to around 0.3. What stands out in this result, however, is the excellent convergence of the block-Jacobi preconditioner with both conformal and nonconformal meshes, which continues to be able to reach the convergence of the equivalent conformal RWG problem.

In the next experiment, the influence of the absolute electrical size of the problem is studied when still using uniform size meshes. A cube with 2 m edge length and uniform mesh size of $h = \lambda/10$ is considered. The same solutions as in the previous examples are considered. Looking at Fig. 4.5, it can be observed a general increase of the number of iterations for all cases, but this rise is well correlated to the increase in the number of iterations for the RWG reference examples. Regarding the location of maximum and minimum of the iterative count with respect to the value of β, a good concordance is observed with the results of Fig. 4.3, revealing that the electrical size of the object does not affect the optimal choice for the penalty factor.

In the following numerical experiments, attention is directed to to the effect of mesh disparity across the tear lines corresponding to transitions between surface meshes of different size. For this, the previous cube of $\epsilon_r = 2.0$ and edge size of 1 m is considered, which is modeled with alternating mesh sizes of $h = \lambda/10$ and $h = \lambda/20$ for the different surface pieces in which it is decomposed, as shown in the inset of Fig. 4.6.

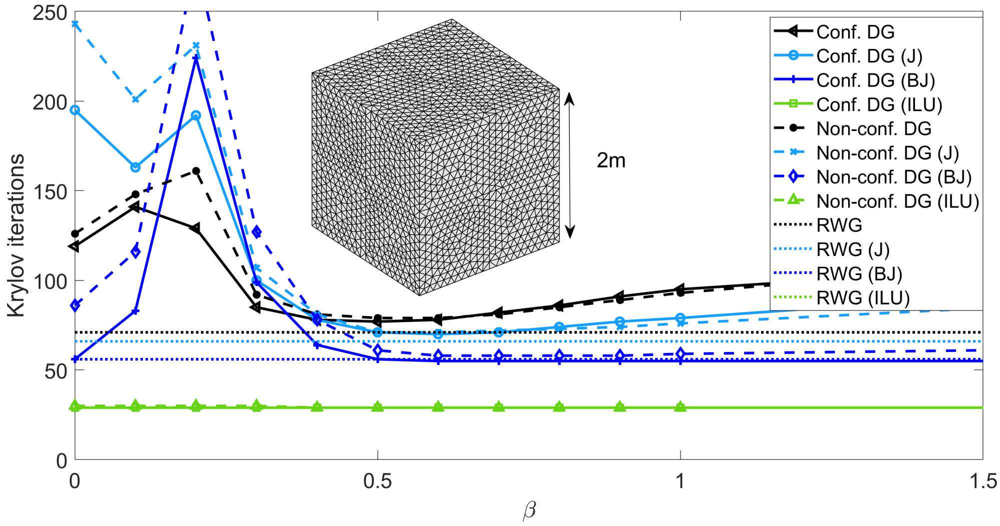

Figure 4.5: Iteration count as a function of β to reach a relative residual error below 10^{-6} for a cube with 2 m edge size and $\epsilon_r = 2.0$ decomposed into 8 surface pieces with uniform mesh size of $h = \lambda/10$.

Three different transition cases are considered: i) Using coarse mesh on both sides of the tear contours, by applying an adaptive mesh thickening in the vicinity of the tear contours on densely meshed surfaces, as shown in the inset of Fig. 4.6; ii) Using fine mesh on both sides of the tear contours, by applying an adaptive mesh refinement in the vicinity of the tear contours on coarsely meshed surfaces, which is depicted in the inset of Fig. 4.7; and iii) Applying different mesh size on both sides of the tear contours, as depicted in the inset of Fig. 4.8. In the first two cases, both conformal and nonconformal meshes are considered. Naturally, only nonconformal meshes can be applied on the latter case, as the triangles on both sides of the tear contours very different in size.

Figures 4.6 to 4.8 gather the results for the different transition examples mentioned above. In all cases good convergences are obtained, demonstrating the robustness of the proposed DG-JMCIE approach to address nonconformal meshes of very different sizes. Interestingly, the iteration number versus the value of β shows a great agreement with the previous results, in which uniform meshing was applied. In this way, the results shown in Fig. 4.6 for the case where coarse meshes are applied to both sides of the tear contours (both conformal and nonconformal) are comparable to those of Fig. 4.3, where uniform coarse mesh sizes are considered for the entire problem. Similarly, the results of Fig. 4.7, where a fine mesh is applied to both sides of the tear contours, are comparable to those of Fig. 4.4, where uniform fine mesh sizes are considered for all surface pieces. Remarkably, the results of Fig. 4.8, calculated considering different mesh sizes on both sides of the tear contours (facing large triangles on one side of the tear contour with nonconformal small triangles on the other side) are also similar to those

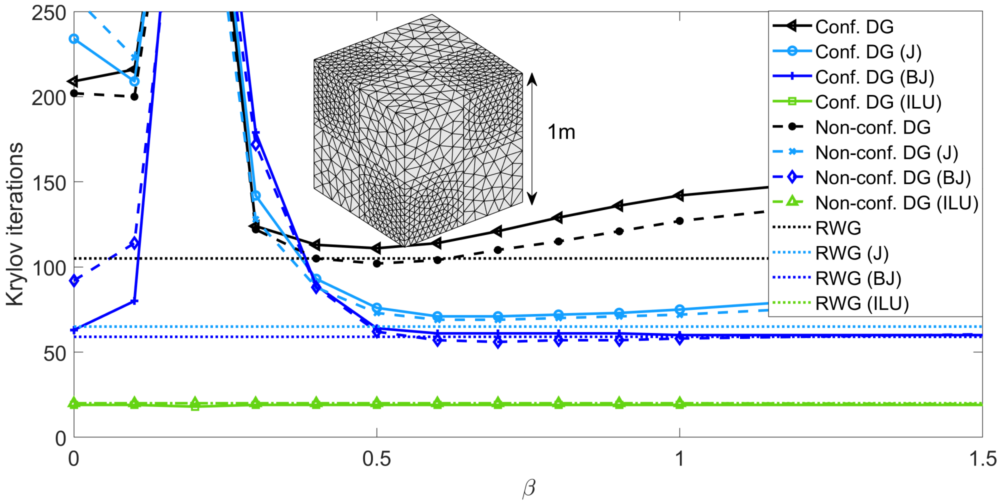

Figure 4.6: Iteration count as a function of β to reach a relative residual error below 10^{-6} for a cube with 1 m edge size and $\epsilon_r = 2.0$ decomposed into 8 surface pieces with alternating mesh sizes of $h = \lambda/10$ and $h = \lambda/20$ and coarse mesh on both sides of the tear contours.

of Fig. 4.4. The reference solutions for this case are those of Fig. 4.7. Further analysis on the convergence histories in Fig. 4.8 shows that block-Jacobi for this example again yields iteration numbers similar to those using conventional RWGs, revealing that this case, of great practical interest, can also be solved accurately in a reasonable time despite drastic mesh size transitions.

In view of the above results, it can be elucidated that the optimal choice of β is determined especially by the size of the mesh in the tear lines between surfaces, where half-RWG basis and testing functions are defined, rather than the mesh size in other surfaces. Importantly, the combination of meshes at very different scales does not impair the performance of the method. A high precision is still achieved in a small number of iterations, on the order of those required in the reference solution with RWGs, thereby paving the way for solving highly complex multiscale problems in a much more comfortable manner.

4.2.4 Composite piecewise homogeneous objects

A final investigation is included to demonstrate the ability and flexibility of the proposed DG-JMCFIE approach to handle composite objects made up of different materials, without need of specific treatment at the multi-material junctions. This eliminates one of the major complications in modeling composite objects with integral equation methodology. The example considered is a composite dielectric cone with a diameter

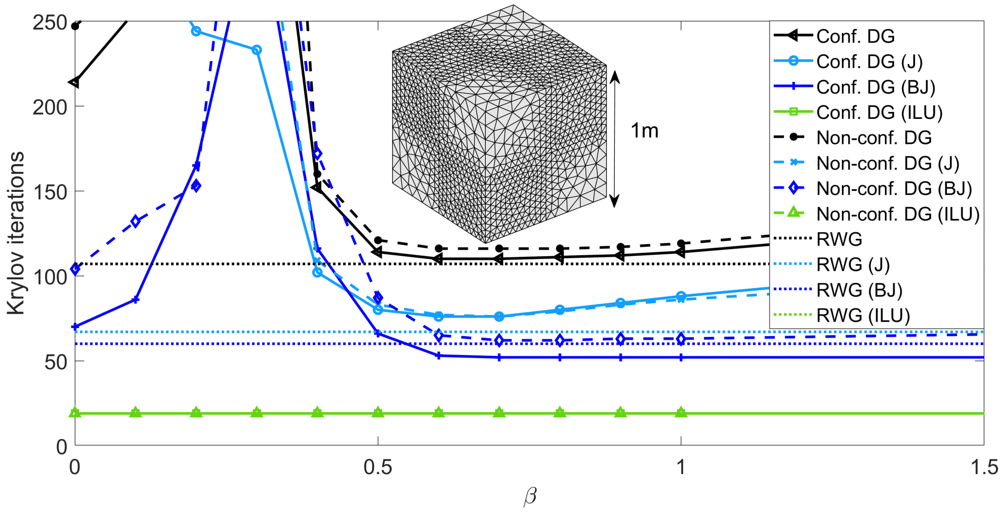

Figure 4.7: Iteration count as a function of β to reach a relative residual error below 10^{-6} for a cube with 1 m edge size and $\epsilon_r = 2.0$ decomposed into 8 surface pieces with alternating mesh sizes of $h = \lambda/10$ and $h = \lambda/20$ and fine mesh on both sides of the tear contours.

of 2 m and 4 m height, in vacuum. It is made up of nine regions R_i, $i = 2..10$, with relative permittivity constants growing correlatively from $\epsilon_{r2} = 2.0$ to $\epsilon_{r10} = 10.0$.

The geometry is depicted in Fig. 4.9. The cone is divided into three main sections along the z-axis. The two lower sections are subdivided into four regions each (R_2 to R_5 and R_6 to R_9 respectively), while the upper section is made of a homogeneous material (R_{10}). This poses 29 boundary surfaces and interfaces between regions. The boundary surface of the last region is in turn decomposed into four surfaces, resulting in a total of 32 nonoverlapping surfaces. These surfaces are independently tessellated and rejoined to assemble the entire geometry, resulting in different kinds of nonconformal tear contours: junction contours at the intersections between three or four surfaces, separating three or four different regions, as well as tear contours between different surface pieces assembling the same homogeneous interface between two regions. In all cases, meshes are nonconformal in the tear and junction contour lines, which in some cases are curved. A total of 69 294 unknowns are applied to model the problem, divided into 66 436 RWG within the conformal surfaces and 2 858 half-RWG in the nonconformal junction and tear contours. The excitation is an $\hat{x}$-polarized plane wave propagating in the $-\hat{z}$ direction at a frequency of 300 MHz.

Figure 4.10 shows the triangles at the tear and junction contours for this example. On the left side, the assembly of half-RWG basis functions at junctions and tear contours to apply the proposed JMCFIE-DG solution is depicted. The (nonconformal) triangles on both sides of the junctions are represented in different colors, meaning that different current coefficients are associated with each half-RWG function. The normal

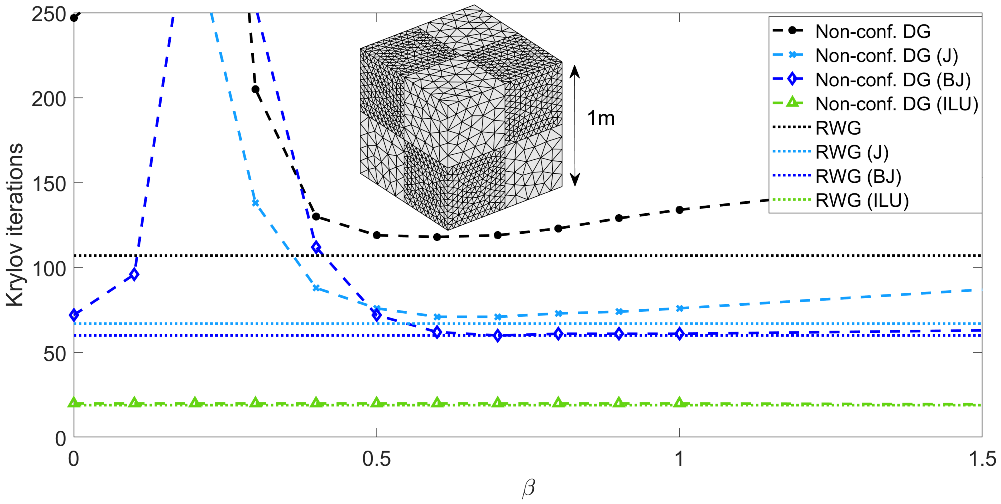

Figure 4.8: Iteration count as a function of β to reach a relative residual error below 10^{-6} for a cube with 1 m edge size and $\epsilon_r = 2.0$ decomposed into 8 surface pieces with alternating mesh sizes of $h = \lambda/10$ and $h = \lambda/20$ in the surfaces and tear lines, resulting in drastic mesh size transitions.

current continuity is in this case weakly enforced throughout the interior penalty. On the right side, the assembly of RWG basis functions at junctions used to calculate the reference result is depicted. The same color is used to depict (conformal) triangles on both sides of the junctions, which means that the RWG functions defined in the different regions and sharing a given junction edge are combined under a single unknown, thus imposing the normal current continuity through the junction (in this case, the multi-region basis functions of [73] are applied to facilitate this solution).

Fig. 4.11 shows the convergence of this problem versus β to reach a residual error below 10^{-6}. A good concordance is observed with the results provided in the previous section, despite the difference in the geometry and composition of the problem, which to a certain extent shows that JMCFIE-DG is an adequate method for any type of problem, regardless its geometry and complexity. Highly accurate results are obtained in reasonable number of iterations despite the use of nonconformal meshes and the high contrast of the media involved in this case, provided that an appropriate penalty factor is chosen.

In Fig. 4.12 the $\hat{\theta}\hat{\theta}$-monostatic RCS of the composite cone in the $\theta = 90$ plane, calculated using the proposed JMCFIE-DG formulation, is compared with the reference result obtained via conventional JMCFIE-RWG formulation. It can be observed that they perfectly agree with each other, further validating the proposed method.

Finally, the equivalent electric and magnetic currents induced at the external boundary surfaces of the cube are shown in Fig. 4.13 for the nonconformal JMCFIE-DG and

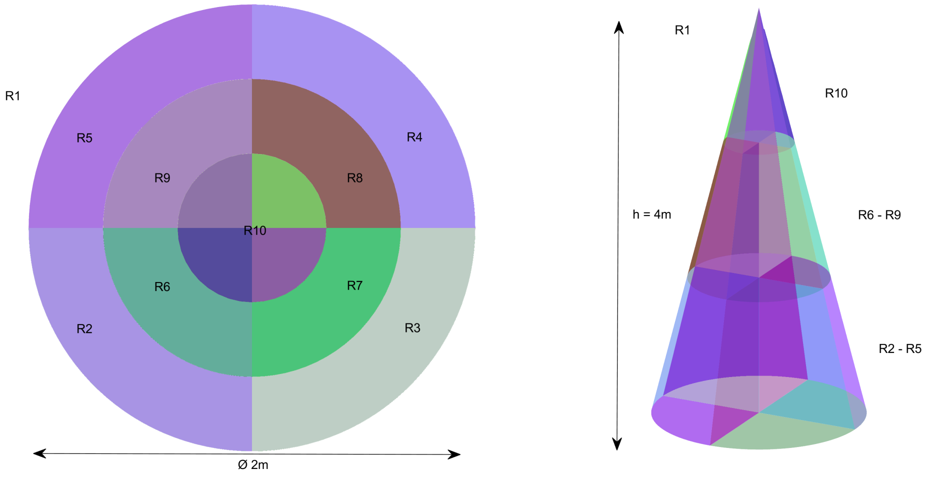

Figure 4.9: Cone-shaped multi-material composite object made up of nine different regions with dielectric permittivity growing correlatively from $\epsilon_{r2} = 2.0$ to $\epsilon_{r10} = 10.0$.

the reference RWG solutions. Looking at this figure, it can be observed that both the electric and magnetic current distributions posed by JMCFIE-DG exactly match the reference solution, flowing smoothly and without the presence of any discontinuity or artifact around the junction contours. All of the above highlights the enormous potential of the inclusion of the DG method in a DD scheme, especially in this case applied to complex composite multi-material objects.

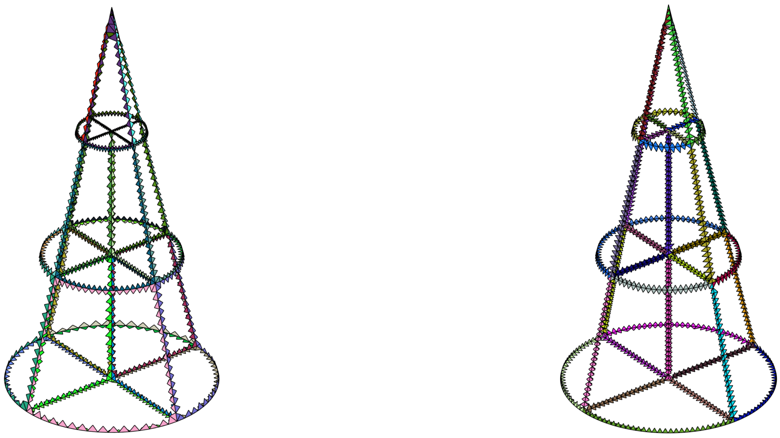

Figure 4.10: Half-RWG functions defined at nonconformal junctions and tear contours for the cone-shape example of Fig. 4.9 (left). RWG functions defined at conformal junctions and tear contours for the cone-shape example of Fig. 4.9(right).

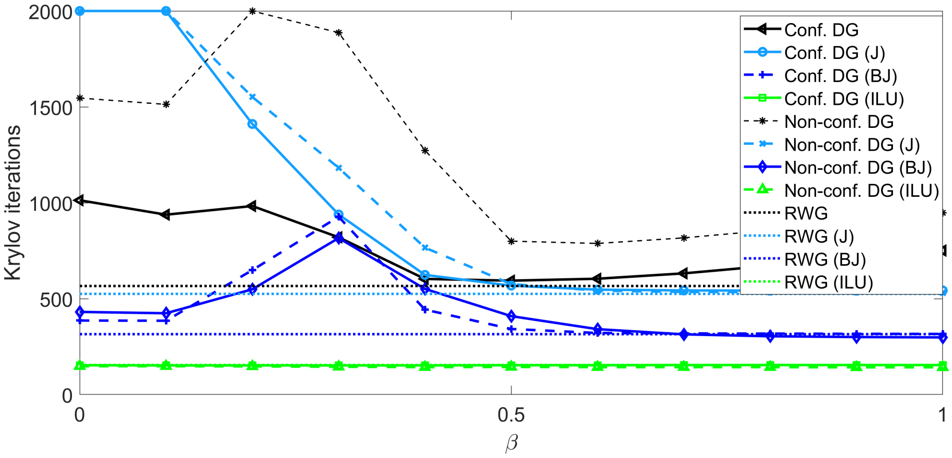

Figure 4.11: Iteration count as a function of β to reach a relative residual error below 10^{-6} for the composite object of Fig. 4.9.

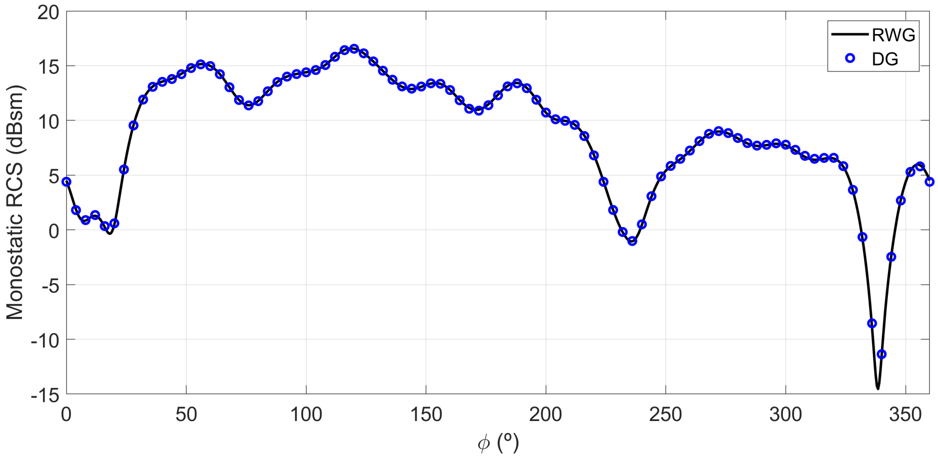

Figure 4.12: $\hat{\theta}\hat{\theta}$-monostatic RCS of the cone-shaped composite object of Fig. 4.9 at 300 MHz in the xy-plane, calculated by the JMCFIE-DG formulation and compared with the conformal RWG reference solution.

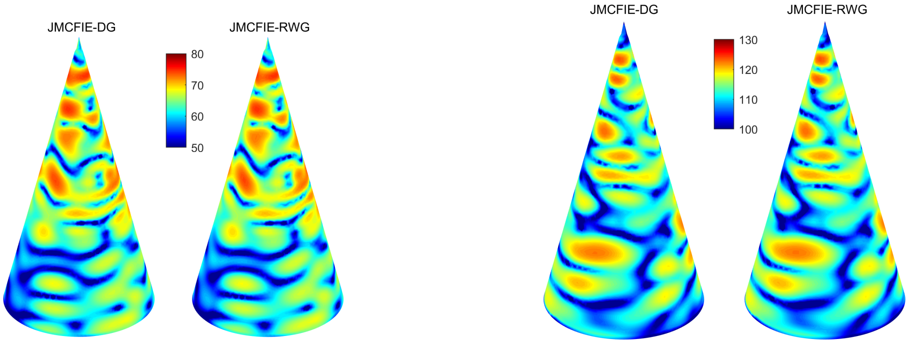

Figure 4.13: Equivalent electric (left) and magnetic (right) current distributions ($dB\mu A/m$) on the external boundary surfaces of the composite object of Fig. 4.9 under plane wave excitation at a frequency of 300 MHz calculated by the proposed JMCFIE-DG formulation (left) and reference RWG solution (right).

4.3 Quasi-Helmholtz preconditioners in non-conformal meshes

In this section the MR preconditioner is developed over the multi-branch RWG basis (MB-MR) functions to automatically build a multi-level quasi-Helmholtz decomposition applied to the MoM solution of complex multi-scale problems discretized with non-conformal meshes.

4.3.1 MB-RWG basis functions

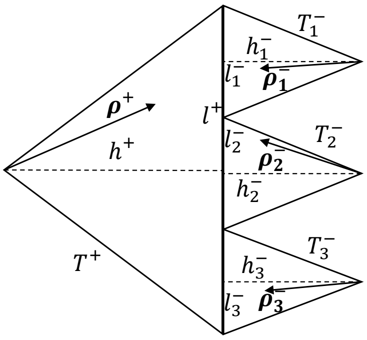

Figure 4.14: Example of a MB-RWG basis function with three branches.

RWG basis functions are the basis functions par excellence for solving SIEs problems defined in terms of triangular meshes. They are defined over two domains (namely, the positive and negative triangles) and have well-known properties that make them especially suitable for solving integral equation problems. Analogous to the RWG functions, the MB-RWG functions are defined over a positive and a negative domain, but in this case one of the two domains (which without loss of generality we will consider here to be the negative one) can be made up of several adjacent triangles (as shown in Fig. 4.14), instead of a single one, as:

$$\mathbf{f}_n^{\mathrm{MB}}(\mathbf{r}) = \begin{cases} \frac{\boldsymbol{\rho}_n^+}{h_n^+}, & \text{with } \mathbf{r} \in T_n^+ \\ -\frac{\boldsymbol{\rho}_{n,i}^-}{h_{n,i}^-}, & \text{with } \mathbf{r} \in T_{n,i}^-,\ i = 1, \dots, M_n \\ 0, & \text{otherwise} \end{cases} \tag{4.8}$$

where T_n^+ is the positive triangle, and $T_{n,i}^-$ are the M_n triangles in the negative domain of the n-th MB-RWG basis function; $\boldsymbol{\rho}_n$ and h_n are respectively the position vector relative to the free vertex and the height relative to the common edge of each triangle. The MB-RWG functions thus defined keep all the desirable properties of RWG functions, namely, null normal component around the outer edges, unit normal component at the common edge lines, and a divergence that can be calculated analytically as

$$\nabla \cdot \mathbf{f}_n^{\mathrm{MB}}(\mathbf{r}) = \begin{cases} \frac{2}{h_n^+}, & \text{with } \mathbf{r} \in T_n^+ \\ -\frac{2}{h_{n,i}^-}, & \text{with } \mathbf{r} \in T_{n,i}^-, i = 1, \ldots, M_n \\ 0, & \text{otherwise} \end{cases} \tag{4.9}$$

4.3.2 MB-MR preconditioner

The standard MR generation procedure is described in Section 3.3.1 of Chapter 3. In the following sections the MR generation scheme will be detailed in the case of non-conformal meshes where MB-RWG basis functions are defined.

4.3.2.1 Multilevel mesh grouping algorithm

One of the critical points regarding the computational efficiency of the MR preconditioner is the development of a function grouping algorithm that allows reducing the order of the local SVDs needed to split the underlying currents into their solenoidal and non-solenoidal parts. The grouping strategy described here extends the scheme proposed in [108] to non-conformal triangular meshes.

In the case of non-conformal or partially non-conformal meshes supporting MB-RWG basis functions, some additional constraints are required to ensure charge conservation in emerging macro-cells. Such constraints are addressed through specific treatment of the non-conformal input mesh (at initial, level-0), where both RWGs and MB-RWGs are defined, posing a proper definition of the level-1 generalized basis functions. In particular, during the aggregation procedure at level-0, if the picked triangle belongs to a negative domain of an MB-RWG function (see Fig. 4.14), all negative triangles of that domain must also be aggregated. This guarantees that each level-1 generalized basis function can be described as a linear combination of complete level-0 RWG and MB-RWG functions. Importantly, to satisfy the charge conservation in level-1, all triangles with a vertex belonging to the internal nodes of this MB-RWG must also be aggregated in the same macro-cell.

To better illustrate the described procedure, Fig. 4.15 shows two possible grouping results when MB-RWG functions come into play, depending on the position of the "central triangle" picked to make the grouping. In the first case, let us consider the central triangle labeled "(1)" in Fig. 4.15(a). The triangles labeled "1" and "2", belonging to respective MB-RWG basis functions, are adjacent to this central triangle, so they are aggregated to the macro-cell labeled “1” in the Fig 4.15(b). The negative triangles of these functions remain free, and will be added in subsequent iterations of the algorithm. However, considering the constraints appointed above, all the negative triangles of each MB-RWG function, together with their adjacent triangles connected to the internal nodes of those functions, must be assigned to the same macro-cell(s). For example, in this case, they have been grouped giving rise to two separate macro-cells, labeled ”3” and ”4” in Fig. 4.15(b).

In the second case, the triangle labeled “(2)” in Fig. 4.15(a) is considered as central triangle, which is part of an MB-RWG function. In this case, all triangles belonging to this function are adjacent to triangle (2) and therefore they are assigned to the same macro-cell of level-1, labelled “2” in Fig. 4.15(b). Again, note that all adjacent triangles of level-0 connected to the internal nodes of the MB-RWG must also be included in the same macro-cell.

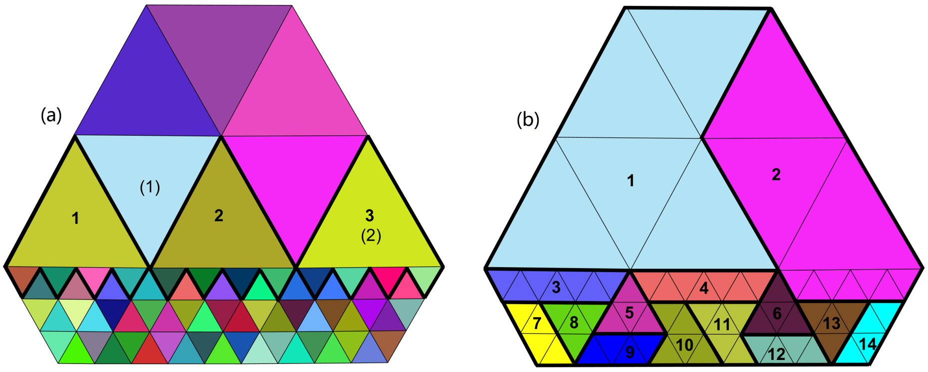

Figure 4.15: Example of cell grouping. (a): level-0 mesh including three MB-RWGs; (b): level-1 mesh (each macro-cell corresponds to a group of adjacent triangles with the same color).

Taking into account the above procedures, the aggregation process is approached through an iterative scheme repeated level by level, in which the central cells are selected and merged with their neighbors (connected or adjacent cells). The implemented algorithm tries to maximize aggregation by avoiding holes in the grouping procedure. The procedure provides good performance compared to other grouping strategies (such as octree-based clustering schemes), posing a good balance in the number of child cells throughout the multilevel grouping, regardless of the density of the underlying mesh.

Finally, depending on the electrical-size of the discretized structure, the grouping scheme is applied until the quasi-Nyquist (coarsest) cell-size level, or up to when all level-($L-1$) cells are completely included in one level-L cell only.

4.3.2.2 Generalized MB-RWG Basis Functions

A set of generalized basis functions $\mathbf{f}_i^l$ is defined on each pair of adjacent level-l generalized cells $C_i^{l,+}$ and $C_i^{l,-}$ and described as linear combination of the level-$(l-1)$ functions as follows:

$$\mathbf{f}_i^l(\mathbf{r}) = \sum_{n=1}^{N_i^{l-1}} f_{i,n}^l \mathbf{f}_{\mu_i(n)}^{l-1}(\mathbf{r}),$$
$$\mu_i \in \{j = j_1, \ldots, j_{N_i^{l-1}} / \mathbf{f}_j^{l-1}(\mathbf{r}) \in C_i^{l,+} \cup C_i^{l,-}\} \tag{4.10}$$

where N_i^{l-1} is the number of level-$(l-1)$ functions defined strictly within the $\mathbf{f}_i^l(\mathbf{r})$ domain. An example of generalized MB-RWG function is shown in Fig. 4.16 defined on two level-1 cells.

This set of generalized bases reproduces the behavior of the initial MB-RWG basis functions at each level. In order to find the coefficients $f_{n,i}^l$ of the above expansion, the surface divergence operator $\nabla_s\cdot$ is applied to both sides of (4.10), and the resulting equation is projected onto the cells of level-$(l-1)$, posing the following linear system:

$$\left[Q_i^l\right]\left[f_i^l\right] = \left[q_i^l\right] \tag{4.11}$$

where $\left[Q_i^l\right]$ is a $M_i^{l-1} \times N_i^{l-1}$ matrix, called charge matrix, whose each m, n element is defined as

$$Q_{im,n}^l = \langle p_m^{l-1}, \nabla_s \cdot \mathbf{f}_{\mu_i(n)}^{l-1}(\mathbf{r}) \rangle \tag{4.12}$$

with M_i^{l-1} equal to the number of level-$(l-1)$ cells that uniquely define the domain of each $\mathbf{f}_i^l$ function, and p_m^{l-1} corresponding to a pulse function, equal to unity inside the corresponding level-$(l-1)$ cell, C_m^{l-1}, and zero elsewhere. $\left[f_i^l\right]$ is a N_i^{l-1} column vector that collects the coefficients $f_{i,n}^l$ with $n = 1, \ldots, N_i^{l-1}$, and $\left[q_i^l\right]$ is a M_i^{l-1} column vector whose elements elements are defined as

$$q_{im}^l = \langle p_m^{l-1}, \nabla_s \cdot \mathbf{f}_i^l(\mathbf{r}) \rangle. \tag{4.13}$$

To facilitate the generation of the above set of generalized functions, the standard MB-RWG functions defined on the input triangular mesh are normalized by the corresponding length of the common edge of the positive triangle $l_{i,+}$, as

$$\mathbf{f}_i^0(\mathbf{r}) = \begin{cases} \frac{\boldsymbol{\rho}_i^+}{2A_i^+}, & \text{with } \mathbf{r} \in T_i^+ \\ -\frac{l_{i,j}}{l_i^+}\frac{\boldsymbol{\rho}_{i,j}^-}{2A_{i,j}^-}, & \text{with } \mathbf{r} \in T_{i,j}^-,\ j = 1, \ldots, M_i \\ 0, & \text{otherwise} \end{cases} \tag{4.14}$$

where A_i^+ and $A_{i,j}^-$ are the areas of the positive and negative domain triangle, T_i^+ and $T_{i,j}^-$, $l_{i,j}$ are the edges of the negative triangles in common with T_i^+, and M_i is the number of negative triangles in the $\mathbf{f}_i^0$ domain. The divergence of (4.14) can be written as

$$\nabla_s \cdot \mathbf{f}_i^0(\mathbf{r}) = \begin{cases} \frac{1}{A_i^+}, & \text{with } \mathbf{r} \in T_i^+ \\ -\frac{l_{i,j}}{l_i^+}\frac{1}{A_{i,j}^-}, & \text{with } \mathbf{r} \in T_{i,j}^-,\ j = 1, \ldots, M_i \\ 0, & \text{otherwise} \end{cases} \tag{4.15}$$

It can be deduced from (4.11) that correctly defining the divergence of each generalized function is enough to properly obtain the generalized coefficients at each level. The divergence of a generalized function ($l > 0$) can be expressed as

$$\nabla_s \cdot \mathbf{f}_i^l(\mathbf{r}) = \begin{cases} \frac{1}{A_i^{l,+}}, & \text{with } \mathbf{r} \in C_i^{l,+} \\ -\frac{1}{A_i^{l,-}}, & \text{with } \mathbf{r} \in C_i^{l,-} \\ 0, & \text{otherwise} \end{cases} \tag{4.16}$$

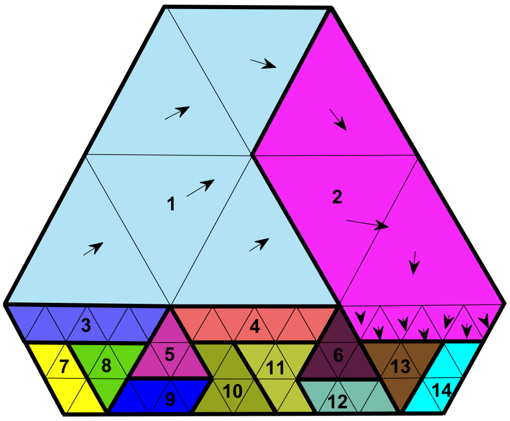

Figure 4.16: Example of a generalized MB-RWG defined on level-1 cells labelled with "1" and "2"

Taking into account that the matrix system (4.11) is indeterminate [56], a new determinate matrix system can be defined by reducing a random row and adding the condition that solenoidal currents do not contribute to the generalized function considered:

$$\begin{bmatrix} \widetilde{[Q_i^l]} \\ [U_i^l] \end{bmatrix} [f_i^l] = \begin{bmatrix} \widetilde{[q_i^l]} \\ [0] \end{bmatrix} \tag{4.17}$$

where $\widetilde{[Q_i^l]}$ and $\widetilde{[q_i^l]}$ correspond to $[Q_i^l]$ and $[q_i^l]$ with one row removed, respectively, $[U_i^l]$ is the set of right singular vectors in the null space of $[Q_i^l]$ (which corresponds to the solenoidal null space functions) that can be obtained through the SVD decomposition of $\left[Q_i^l\right]$, and $[0]$ is a null vector of dimension $(N_i^{l-1} - M_i^{l-1} + 1)$. Solving the system (4.17), the coefficients $f_{i,n}^l$ of (4.10) are found. Then, applying (4.10) recursively, any level-l generalized function $f_i^l(\mathbf{r})$ can be expressed as a linear combination of basis functions at level-0.

4.3.2.3 Multi-Resolution MB-RWG Functions

The procedure for generating multi-resolution MB-RWG functions is described below. The MR functions provide a set of bases capable of improving the spectral properties of the SIE system by separating the current into solenoidal and non-solenoidal parts in a hierarchical scheme. The properties and multilevel nature of these functions transform the matrix system into a robust and well-conditioned system capable of accurately handling multiscale features and very small details, in contrast to a generic quasi-Helmholtz decomposition.

A collection of functions can be defined at each level of the hierarchical mesh decomposition as a linear combination of generalized functions at this given level as

$$\mathbf{w}_i^l(\mathbf{r}) = \sum_{k=1}^{K_i^l} T_{i,k}^l \, \mathbf{f}_{\delta_i(k)}^l(\mathbf{r}) \tag{4.18}$$

where K_i^l is the number of $\mathbf{f}_{\delta_i(k)}^l(\mathbf{r})$ functions defined inside the domain of $\mathbf{w}_i^l$.

The first step to build the MR functions is the generation of the charge matrices in (4.12) for each group of children level-l cells belonging to a given level-$(l+1)$ cell. Then, the coefficients $T_{i,k}^l$ for non-solenoidal functions are determined by the non-zero singular vectors of the charge matrix, while the null singular vectors correspond to the coefficients of the solenoidal functions. To complete the solenoidal part, the divergence-free functions defined across each pair of adjacent level-$(l+1)$ cells must be added [86]. This set can be extracted from the null space functions of the joint charge matrix for the cells defining each generalized MB-RWG function on the level-$(l+1)$ mesh and subtracting the function space generated at the previous step by the Gram-Schmidt orthogonalization process.

A generic MR function $\mathbf{w}_i^l$ of level-l is expressed in (4.18) as linear combination of the generalized basis functions of the same level. Importantly, considering that all generalized functions at any level can be expressed as linear combinations of the original input MB-RWG and RWG functions (level-0), any generic level-l MR function can also be described as a linear combination of the input basis functions. This allows the construction of an MR change-of-basis matrix, paving the way for the application of the multilevel MR basis functions set as left and right multiplicative preconditioner of the original system.

4.3.2.4 Complexity

As mentioned in previous sections, the most expensive operation in the generation of the proposed preconditioner is the SVD decomposition needed to find the coefficients of the solenoidal and non solenoidal bases. Applying the hierarchical decomposition of the input mesh, the dimension of the charge matrices is always small and independent of the total number of unkowns (N), reducing the complexity of the algorithm up to $O(N \log N)$, where $\log N$ corresponds to the number of levels. The hierarquical nature of the MR basis functions limits the number of original basis that an MR depends to those defined on triangles belonging to the level-$l+1$ parent cells. Then, the change-of-basis matrix is sparse, allowing an efficient application of the MR preconditioner to the original system through parallel algorithms for sparse computation. The complexity of the generation algorithm is shown in Fig. 4.17 for the case of a sphere subdivided into eight symmetrical parts, with non-conformal meshes in the contours between them.

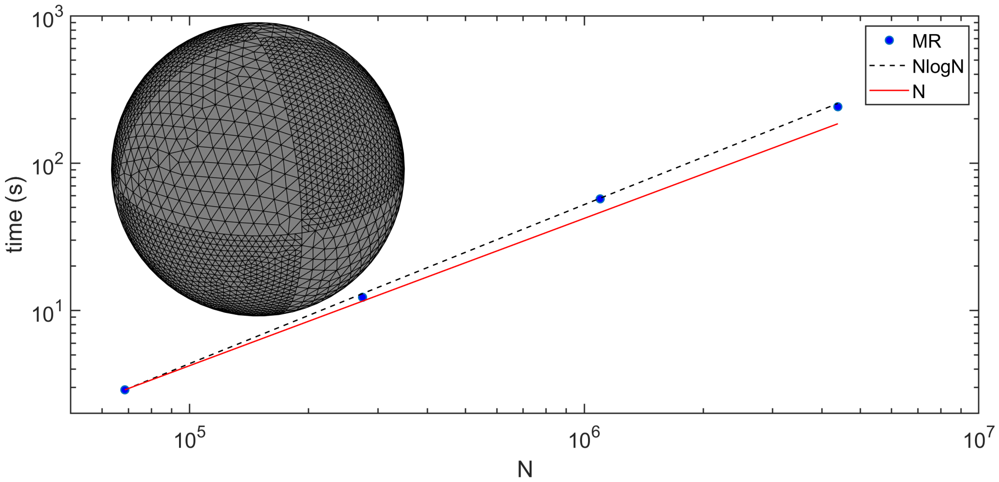

Figure 4.17: Time to generate the multi-resolution basis versus the number of unknowns N. Case of a sphere.

4.3.2.5 Parallel implementation

The generation of the MR basis functions is parallelized in shared memory computers applying a two-step strategy. First, the grouping algorithm is applied sequentially to obtain the relation between cells and generalized basis functions of level-$(l+1)$ with cells and generalized basis functions of level-l. Next, local indices referring to the children of the cells and basis functions are precomputed in level-$(l+1)$ using two parallel loops, which includes the generation of the elements of the charge system (4.11). In a second step, the multi-resolution coefficients in (4.18) of level-$(l+1)$ are computed from the coefficients of level-l using two additional parallel loops.

The above scheme provides a good scalability, which facilitates the parallel generation of the charge matrices and the MR functions, enabling the application of this method to real-life large-scale complex problems.

4.3.3 Validation and application

A numerical example is introduced to validate the proposed approach for the automatic generation of all solenoidal and non-solenoidal functions in the solution of a small object containing global loops. A Möbius volumetric belt is considered, formed by three Möbius strips connected to each other by three small curved bands, forming a smooth curvature in the wedges (with a diameter of curvature of $\lambda/15$ and strip width of $\lambda/75$), as shown in Fig. 4.18. The surfaces that form this structure are meshed independently, yielding non-conformal meshes at the junctions between them (see Fig. 4.18.(right)). The smooth strips are meshed with $\lambda/300$ triangular elements, while the three curved bands placed on the wedges are meshed with $\lambda/1500$ triangular size to minimize the geometrical discretization error on the curved wedges. The use of non-conformal meshes allows a drastic reduction in the number of unknowns, by removing the transition regions that would be required in the case of the equivalent conformed mesh, as illustrated in Fig. 4.18(left). Consequently, the total number of unknowns reduces from 84180 RWGs to 33 033 RWGs plus 720 MB-RWGs.

First, the generation of the quasi-Helmholtz decomposition is examined. The input mesh has 23 702 triangles (M), 10 051 inner nodes (excluding MB-RWG internal nodes), and one structural handle (H). Figure 4.21 shows the cell grouping generated by the algorithm described in Sect. 4.3.2.1, from level-1, where the input triangles are rearranged to provide the first generalized cells, to the last level, where all the input triangles are included in a single generalized cell. A detailed view of the level-1 grouping in the vicinity of the non-conformal meshes is shown in the upper right corner of Fig. 4.21.

The proposed multi-resolution generation scheme is then applied to each level-l mesh, automatically posing 10 052 solenoidal functions (N_s), and 23 701 non-solenoidal functions (N_{ns}), spread across the 7 levels of the grouping. These numbers match the required relationship between the number of non-solenoidal functions ($N_{ns} = M - 1$),

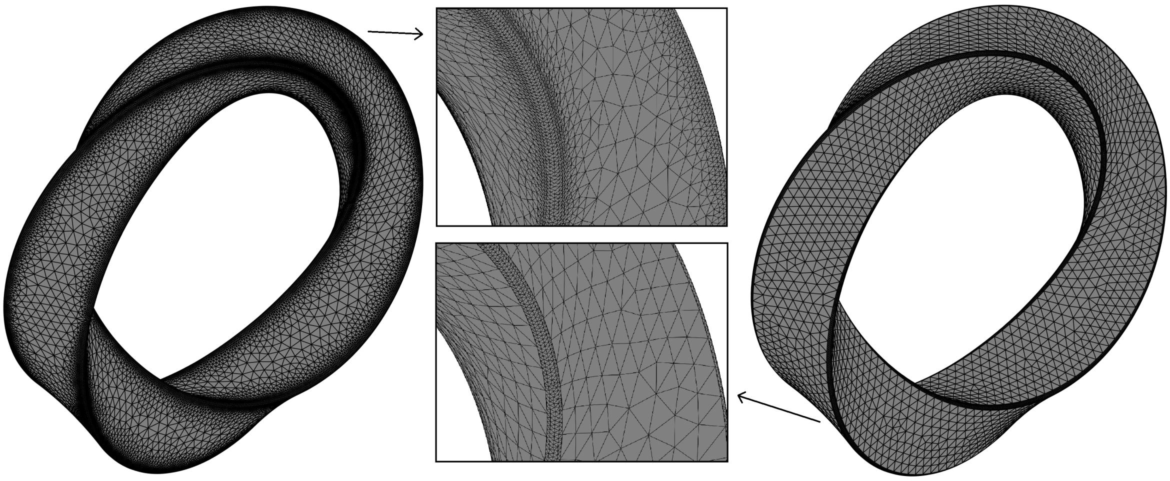

Figure 4.18: Conformal (left) vs non-conformal (right) meshes of the proposed Möbius strip.

and solenoidal functions ($N_s = V_{int} - 1 + 2H$), including the topological (global) loop corresponding to the handle, as described in [109].

The bistatic RCS is calculated for this example using the proposed MR preconditioner, grown from the RWG and MB-RWG basis functions. The result is depicted in Fig. 4.19, compared to the reference MoM solution using the conformally meshed structure of Fig. 4.18(left). A perfect agreement is observed between the MR-MB approach and the reference solution. The equivalent electric currents on the Möbius surfaces are shown in the inset of Fig. 4.19.

Figure 4.20 shows the convergence of the proposed approach in terms of the iteration number under an iterative Krylov resolution of the matrix system. Looking at this figure, it can be observed that the MR preconditioner applied to non-conformal meshes outperforms the MB-RWG solution alone, without preconditioner, despite the small electrical size of the object. This reveals the effectiveness of the MR preconditioner applied to non-conformal meshes thought multi-branch basis functions.

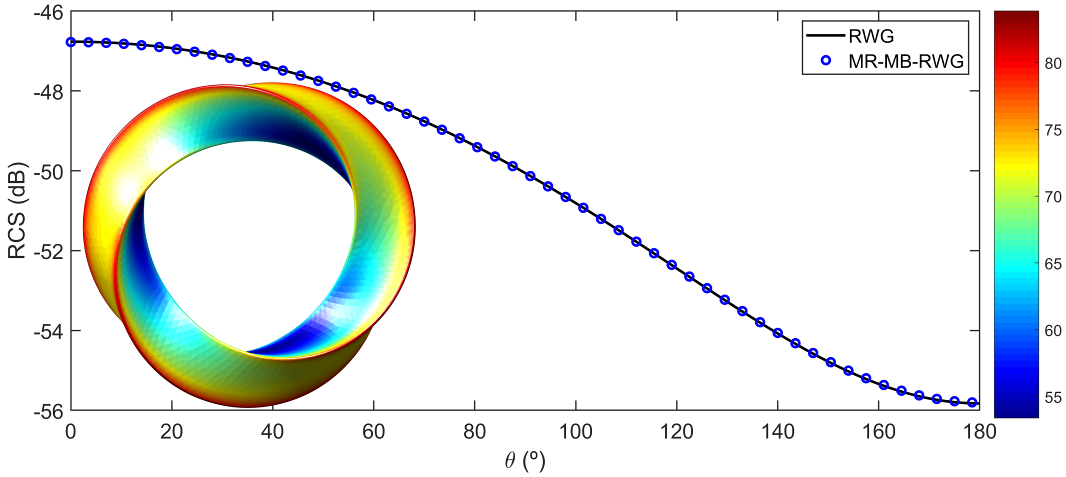

Figure 4.19: Bistatic radar cross section and the electric current distribution ($dB\mu A/m$) of the mobius strip.

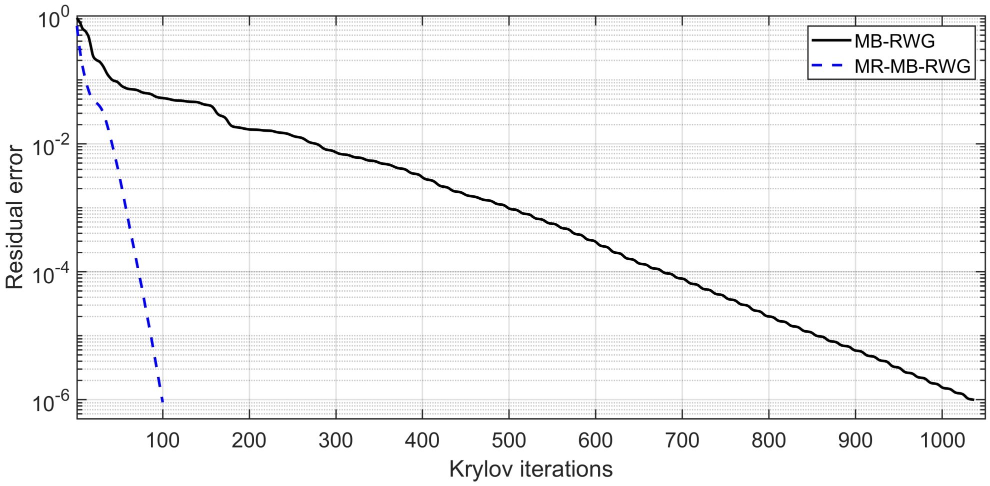

Figure 4.20: Iteration count for the mobius strip considering a plane wave excitation.

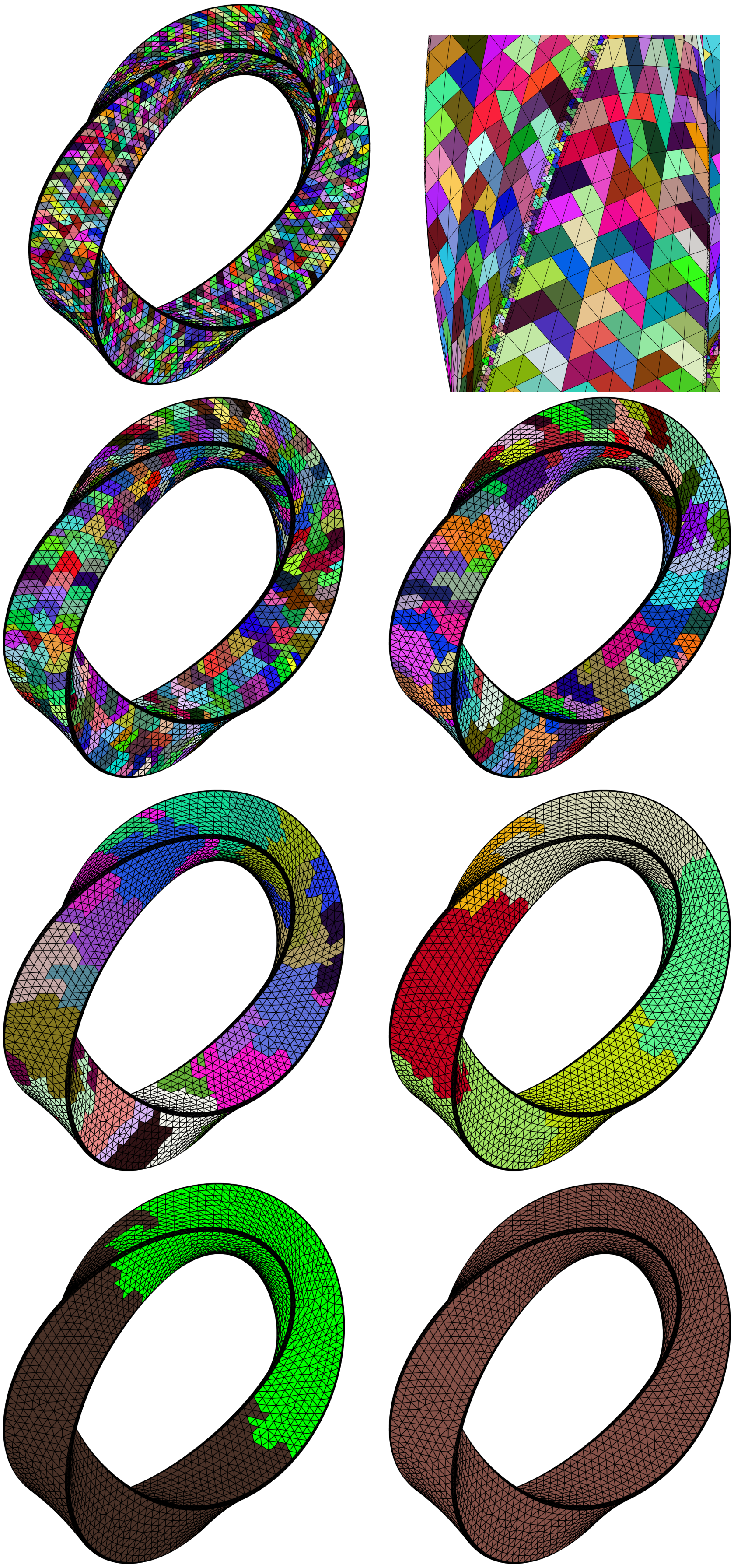

Figure 4.21: Multi-level cell grouping algorithm for the proposed mobius strip.

Chapter 5

Applications

Contenido

In previous chapters, a hybrid MPI/OpenMP parallel version of the multilevel tear-and-interconnect DDM was described, including non-conformal techniques and multiresolution preconditioners to improve the versatility and efficiency of the EM simulation methodology. In this chapter, the performance of the implemented software is tested by solving several complex large-scale composite penetrable and non-penetrable objects exhibiting deep multiscale features, in the context of real-life EMC/EMI and nanotechnology applications.

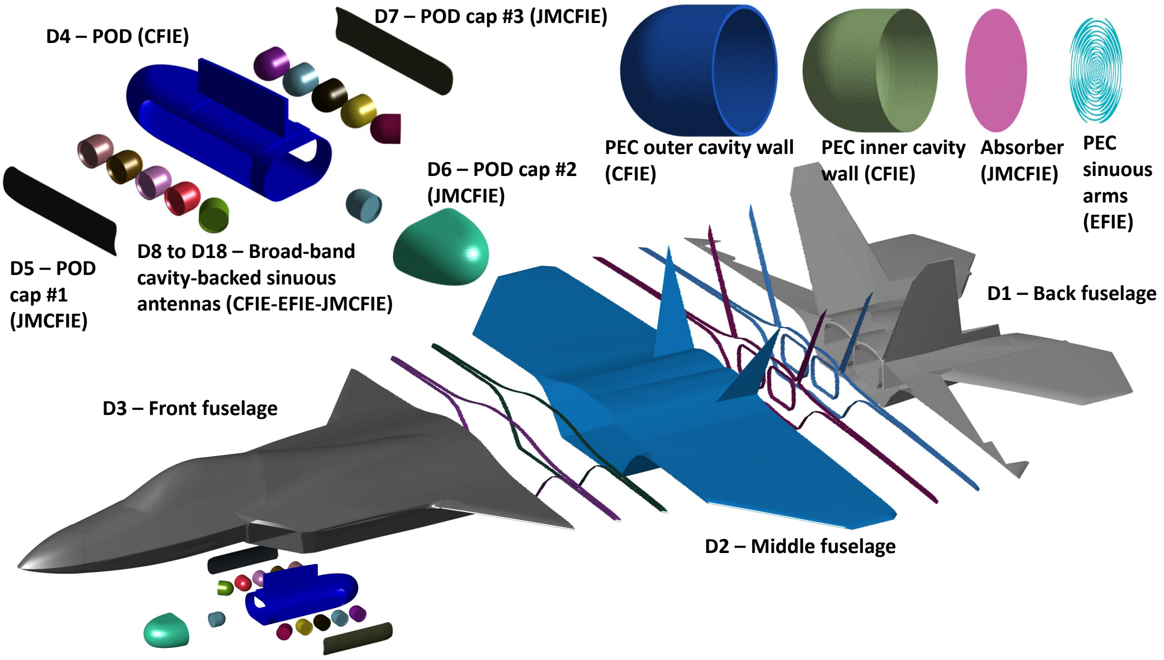

Figure 5.1: Partition into 18 subdomains of the F-22 aircraft and onboard radiating systems. The dimensions of the aircraft are approximately 15 m long, 20 m wide and 5 m high ($50\lambda \times 66.667\lambda \times 16.667\lambda$ in terms of the used working wavelength corresponding to 1 GHz). The solver employed in each domain is indicated. The inner flaps of each touching domain (outer flaps of adjacent domains) are shown.

5.1 EMC applications

5.1.1 F-22 tactical fighter aircraft

The following example demonstrates the ability of the proposed SIE-DDM method to handle multi-scale composite materials. The objective is to obtain the accurate vector solution with the currents induced over the surface of an F-22 aircraft and the onboard sensors. Subsequently, this solution could be post-processed to predict the operational performance of the different systems involved. The geometry of the problem is shown in Figure 5.1. The total number of unknowns is 5 766 388, with the discretization size varying from $\lambda/10$ to $\lambda/360$, being λ the wavelength corresponding to 1 GHz. The F-22 fuselage, including the engine air intake cavities, is split into 3 large PEC touching subdomains, as shown in Figure 5.1, including the corresponding flaps to apply the transmission conditions between them. Note that the partition does not respond to the different subsystems of the fuselage (such as wings, tail, nose, etc.), but it simply divides it into three approximately equal parts. A partition by subsystems could be more convenient, although it is not imperative. The radiating systems consist of 11 antennas (subdomains D_8 to D_{18}) assembled inside a PEC POD located in the underbelly of the aircraft. The POD is made up of four pieces: the central PEC body to hold antennas (D_4), and three protection dielectric covers (D_5 to D_7), which are electromagnetic "transparent" at the operating frequency of 1 GHz. We considered absorbent-loaded cavity-backed sinuous antennas as those in [110, 111], all of them equal. The structure of the antennas is detailed at the top of Figure 5.1. Each antenna is a complex musti-scale composite structure made up of several sinuous PEC arms of about 3 mm width ($\lambda/100$), describing a complex pattern including tiny details, which demands a careful generation of the mesh. The sinuous arms are embedded on a PEC cavity filled with absorbing material to avoid back radiation and increase gain in the maximum radiation direction, thus providing circularly polarized transmissions in the forward direction in the UHF band. For this complex problem the requirement fixed for the GMRES residual error is of 10^{-4} for the outer GMRES and 10^{-5} for the inner GMRES. The global MVP is computed using accelerated near field radiation between subdomains. The simulations were performed in a cluster with 4× Xeon E7-8867v3@2.5GHz (4×16 cores = 64 cores) and 1 TB of RAM memory.

The comparative analysis of the convergence performance of the SIE-DDM approach and MLFMA is shown in Figure 5.2. Only 20 iterations of the outer GMRES and 18 hours of simulation were required with the SIE-DDM approach to converge to a residual error of $8.5 \cdot 10^{-5}$, below the prescribed threshold. The MLFMA simulation, however, took more than 20 000 external iterations and 72 hours to achieve a residual error of $7 \cdot 10^{-3}$. The challenging multi-scale and multi-material features of this problem make it difficult for the global problem to converge if a proper preconditioning strategy is not employed. Moreover, the possibility offered by the SIE-DDM approach of using multiple formulations within a subdomain (see Figure 5.1) has special positive implications in the convergence when there are composite subdomains, as in this example.

The computational parameters of the simulation corresponding to this problem are gathered in Table 5.1. The approach exploits the fact that the single antenna subdomains D_8 to D_{18} are geometrically identical, except from rotation and/or translation movements, by reusing the MoM impedance matrix calculations of the first antenna subdomain for all of them. The convergence records of Figure 5.2, together with the data of Table 5.1, point out again that the SIE-DDM implementation allows to take on real-life projects involving convergence difficulties, high requirements of computational resources and time constraints. Finally, Figure 5.3 shows the equivalent surface current distribution over the aircraft surface.

Table 5.1: Computational metrics of subdomains in the simulation of F22 example

Domain	D_1	D_2	D_3	D_4
Unknows	1 904 096	1 677 374	1 746 978	255 084
Memory (GB)	258.6	162.8	189.4	44.1
Setup time (s)	5380	33136	3851	1188
Solving time (s)	6084	665	708	184
Domain	D_5	D_6	D_7	D_8
Unknows	54 360	109 872	54 504	19 874
Memory (GB)	10.5	22.2	10.6	12.0
Setup time (s)	350	885	350	262
Solving time (s)	13	43	14	0.5
Domain	D_9	D_{10}	D_{11}	D_{12}
Unknows	19 874	19 874	19 874	19 874
Memory (GB)	12.0	12.0	12.0	12.0
Setup time (s)	262	262	262	262
Solving time (s)	0.5	0.5	0.5	0.5
Domain	D_{13}	D_{14}	D_{15}	D_{16}
Unknows	19 874	19 874	19 874	19 874
Memory (GB)	12.0	12.0	12.0	12.0
Setup time (s)	262	262	262	262
Solving time (s)	0.5	0.5	0.5	0.5
Domain	D_{17}	D_{18}		
Unknows	19 874	19 874		
Memory (GB)	12.0	12.0		
Setup time (s)	262	262		
Solving time (s)	0.5	0.5		

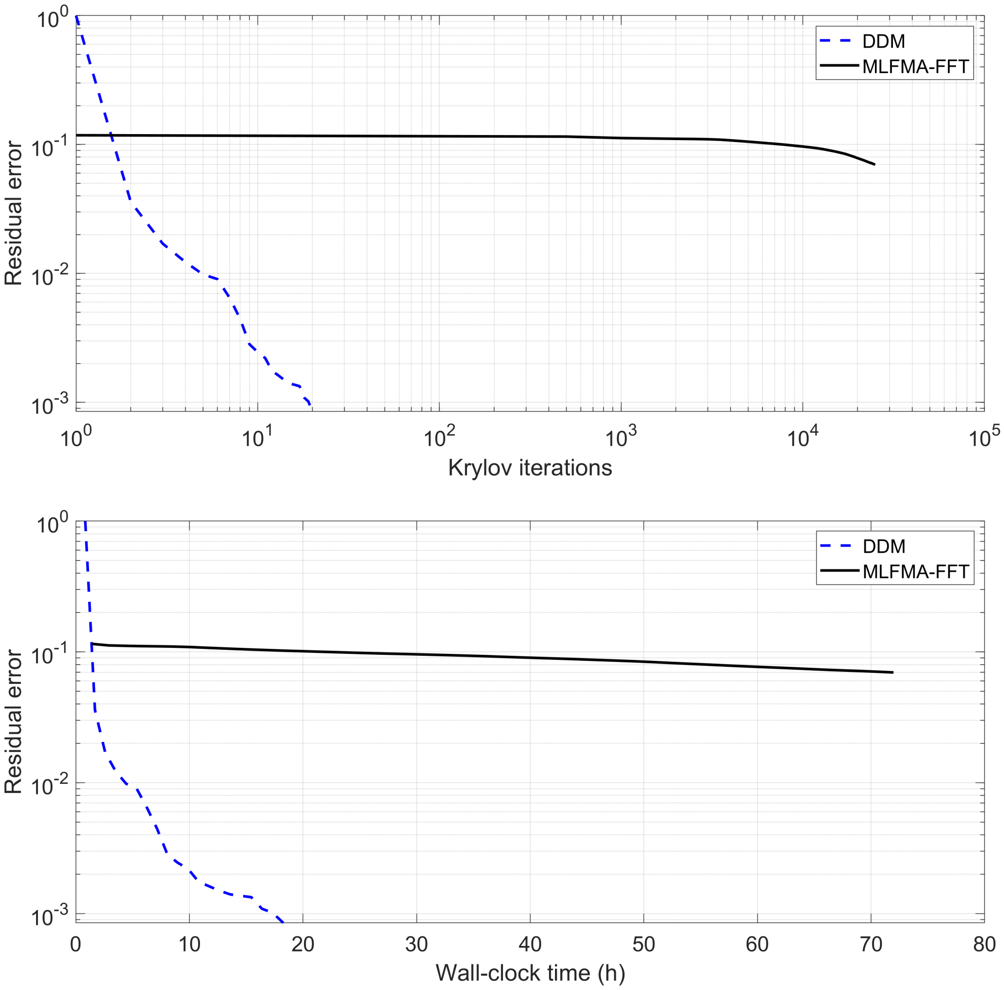

Figure 5.2: Convergence performance of the outer GMRES when solving the EMC problem of the F-22 aircraft using the proposed SIE-DDM method and the MLFMA: (a) residual error versus number of iterations; (b) residual error versus time.

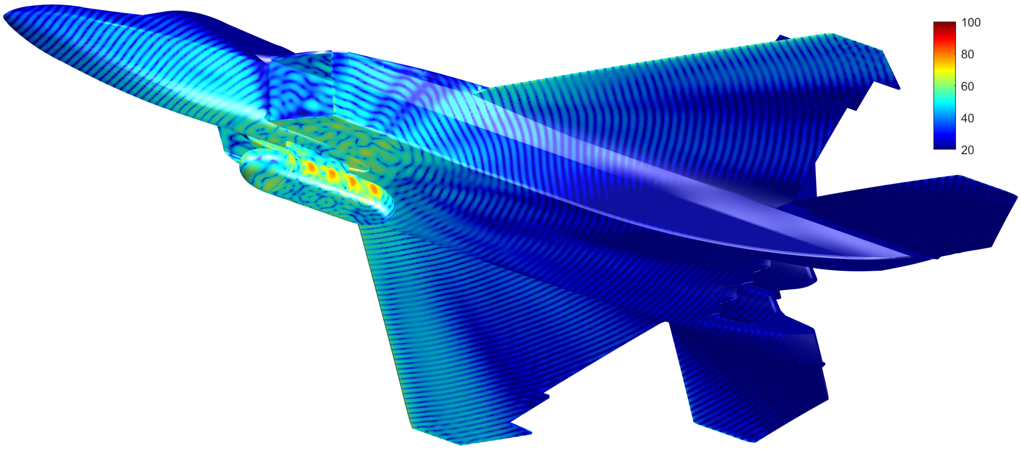

Figure 5.3: Real part of the equivalent electric surface current distribution $(dB\mu A/m)$ on the F-22 aircraft surfaces provided by the proposed SIE-DDM method.

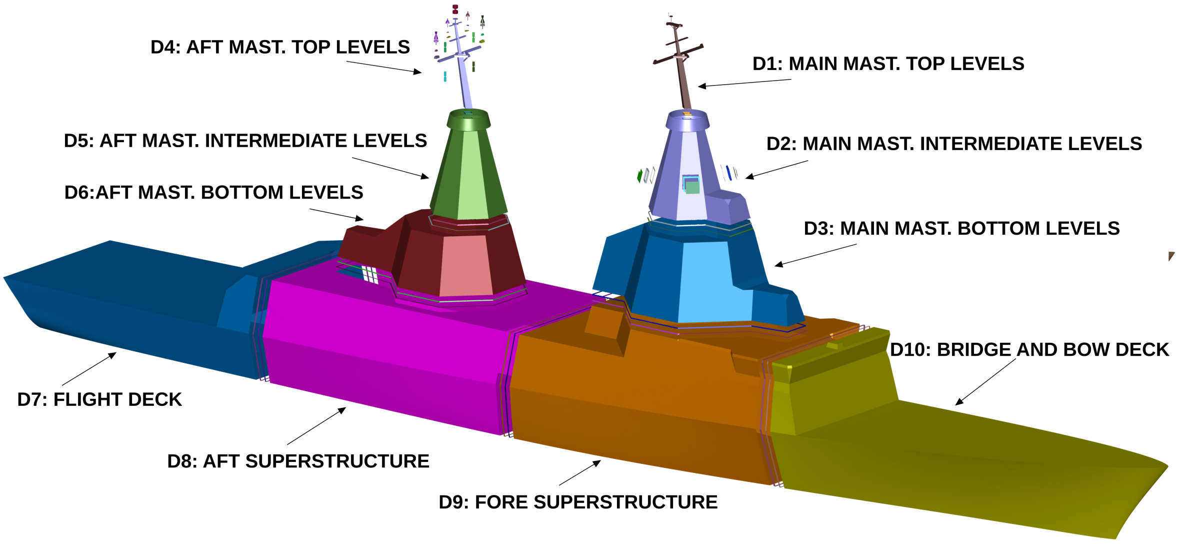

Figure 5.4: Partition into subdomains of the superstructure and masts of the vessel.

5.1.2 Isolation Among V/UHF Communication Systems Onboard a Modern Vessel

A second numerical example is introduced to highlight the ability and versatility of the proposed approach to solve challenging multi-scale problems using non-conformal meshes. The evaluation of the isolation between the antennas belonging to four communications and tactical intelligence systems installed in a realistic vessel is attempted in this section. The first system (S_1) is intended for air-to-ship communications operating in the VHF band. It consists of several transceivers connected throughout multiport combining filters to four patch antennas integrated in the intermediate level of the main mast. The antennas are specifically designed to work simultaneously providing a full 360° field of view and are meshed separately, with a mesh size tailored to the fine detail features of their respective structures, and placed on the platform mesh resulting in non-conforming triangles on either side of the tear (connection) lines. Some details of the resulting non-conformal mesh are illustrated in Fig. 5.7).

The second system (S_2) operates in the V/UHF band, dedicated to exterior communications. The transceiver is connected without associated external filtering to two omnidirectional vertically polarized coaxial dipole antennas [112] located at the main yardarm of the aft mast, in port/starboard arrangement. The third system (S_3) is composed of two transceivers connected to respective UHF omnidirectional vertically polarized sleeve dipole antennas [112, 113]. The antennas are sited on the upper yardarm of the aft mast, in port/starboard arrangement. The fourth system (S_4) is an V/UHF system for surface naval applications that makes use of four broadband omnidirectional, vertically polarized active bicone antennas located at the aft mast.

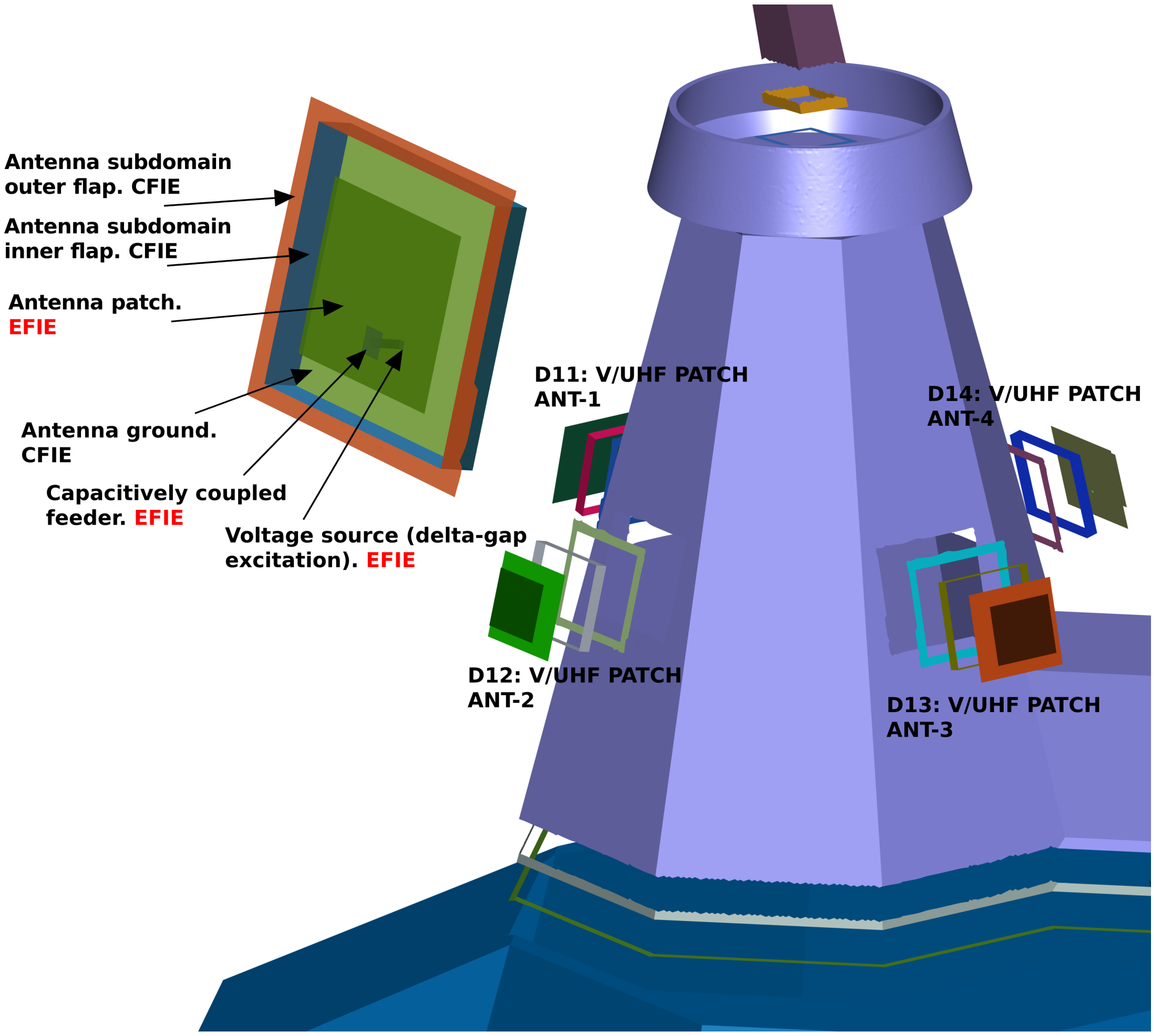

Figure 5.5: Arrangement of the antennas on the main (forward) mast of the proposed vessel and partition into subdomains. The inner flaps of each touching domain (outer flaps of the adjacent domains) are shown. The formulations employed inside each domain are indicated.

The dimensions of the realistic (although fictitious) ship are approximately 140 m length, 20 m beam and 40 m height ($140\lambda \times 20\lambda \times 40\lambda$ in the used working wavelength, λ, corresponding to the frequency of 300 MHz). A total of 13 864 912 unknowns are required in order to mesh the entire geometry of the problem, including 3 468 MB-RWG basis functions. The vastly multi-scale character of this geometry is brought to light by the wide variation margin of the edge length of the triangular patches, which goes from $\lambda/10$ in smooth surfaces of the geometry to $\lambda/1639$ in regions containing antennas with fine details (especially in the vicinity of feeding areas [114]).

According to the multi-scale features of the problem, it is decomposed into $p = 23$ subdomains, as shown in Figures 5.4 to 5.6 :

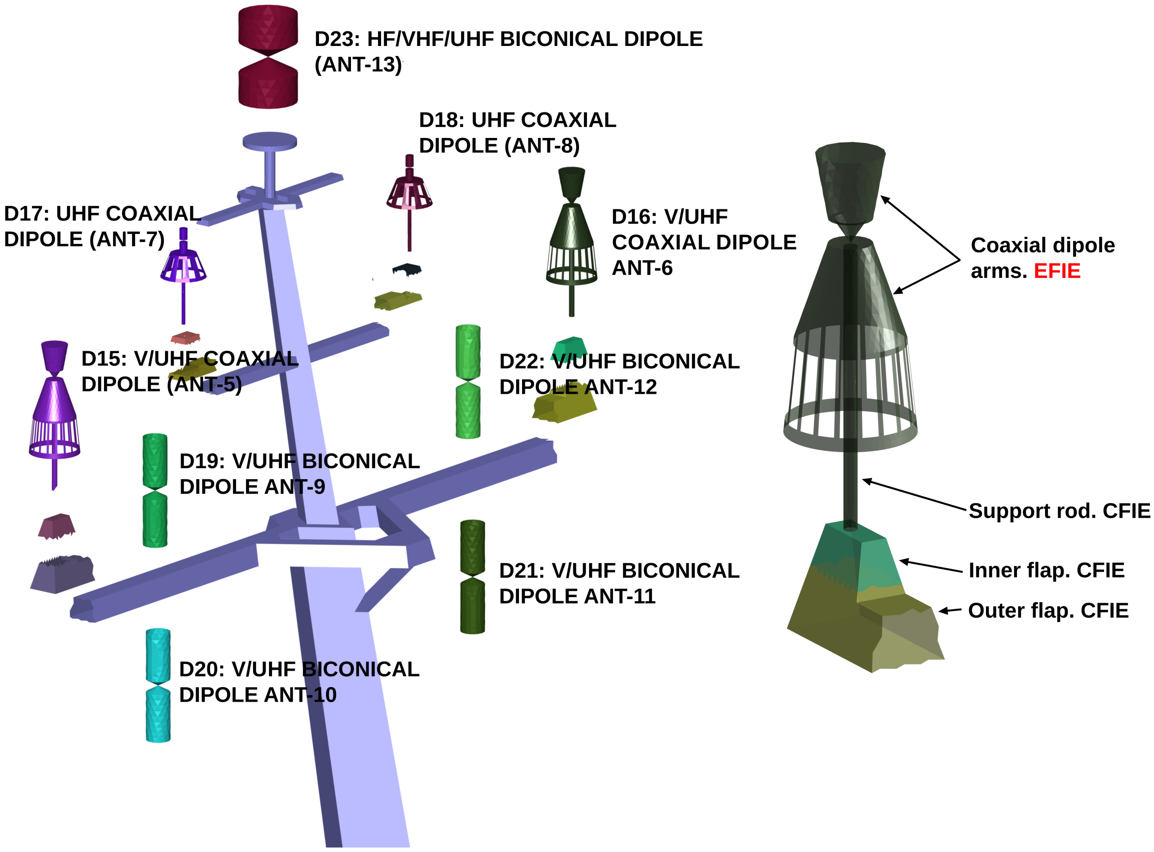

Figure 5.6: Arrangement of the antennas on the aft mast and partition into subdomains of the proposed vessel. The inner flaps of each touching domain (outer flaps of the adjacent domains) are shown. The formulations employed inside each domain are indicated.

- 10 large subdomains (D_1 to D_{10}) containing structural parts of the vessel (Figure 5.4). They are solved using 10 independent four-level MLFMA-FFT solvers.
- 13 electrically small subdomains (D_{11} to D_{23}) including the 13 antennas onboard (Figures 5.5 and 5.6): D_{11} to D_{14} include the antennas #1 to #4 of system S_1, D_{15} and D_{16} include the antennas #5 and #6 of S_2, D_{17} and D_{18} include the antennas #7 and #8 of S_3, and D_{19} to D_{23} include the antennas #9 to #13 of S_4. These subdomains are solved via direct MoM and MoM with MB functions for the non-conformal cases.

The inner and outer flaps are identified in each case to indicate the formation of restricted and augmented subdomains.

Excitation with delta-gap voltage sources at the feed terminals defined along the circumference perimeter of the feed wires is considered, as illustrated in the right insets of Figures 5.5 and 5.6. Remarkably, MB-RWG basis functions are being considered as

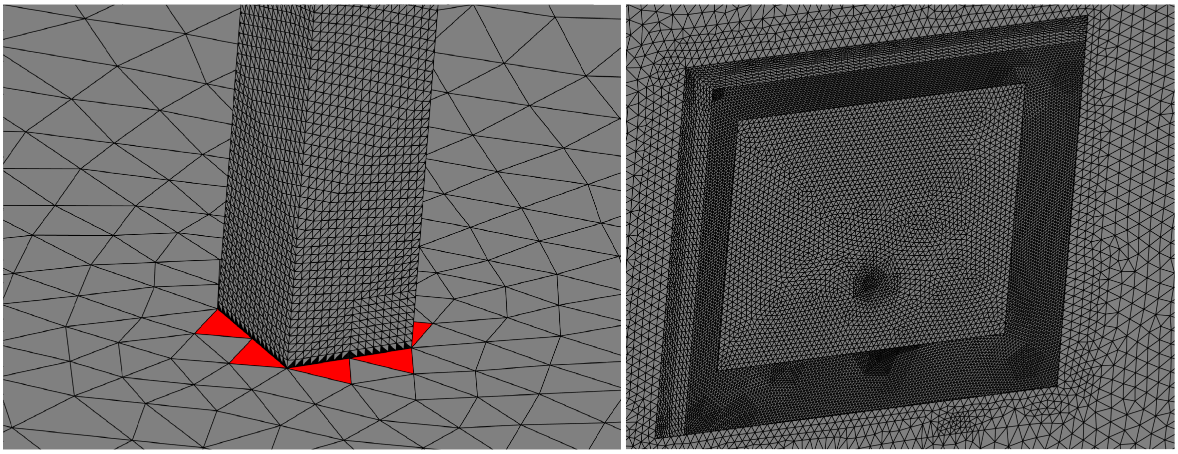

Figure 5.7: Non-conformal mesh details of the feeding point and the connections of antennas with the vessel structure.

feeder terminals, for which the voltage value must be weighted by the length of the common edge of the positive triangle at each basis (see Figure 5.7). The entire problem is modeled as perfectly conducting surfaces. Consequently, the EFIE formulation ($\alpha = 1$) is used for open surfaces, namely the open parts of the antennas as well as the feed points. CFIE formulation ($\alpha = 0.5$) is used for the rest of surfaces, despite the fact that the application of the DDM scheme shows them as open surfaces with holes corresponding to the connection of the antenna subdomains to the superstructure of the vessel. Nevertheless, those “seemingly” open surfaces are actually part of closed surfaces in the original problem, and they are certainly closed back by the incoming radiation coming from all the other subdomains, which is added up on the right hand side of the local subsystems. To accomplish this, both the EFIE and the CFIE must be able to be combined arbitrarily on the geometry surfaces, regardless of their assignment to the same or different subdomains.

The global MVP that account for the mutual coupling between subdomains at the external Krylov stage is sped up via MLFMA-FFT. A residual error of 10^{-6} (10^{-7}) is imposed as requirement for the outer (inner) GMRES. Surprisingly, we have checked that better convergence rates are reached if a high precision is ascribed to the inner solvers making up the preconditioner. Consequently, equal or even more restrictive GMRES residual error thresholds than those imposed for the global iterative solver are set for the inner problems. The simulations were performed in a cluster with 4× Xeon E7-8867v3@2.5GHz (4×16 cores $= 64$ cores) and 1 TB of RAM memory.

To conduct a comprehensive EMC/EMI study in a real engineering case like this, the simulations could easily be extended from HF to X-band or higher. In this academic case study, however, the numerical simulations have been constrained to a frequency sweep from 100 MHz to 550 MHz, according to the different operating bands of the

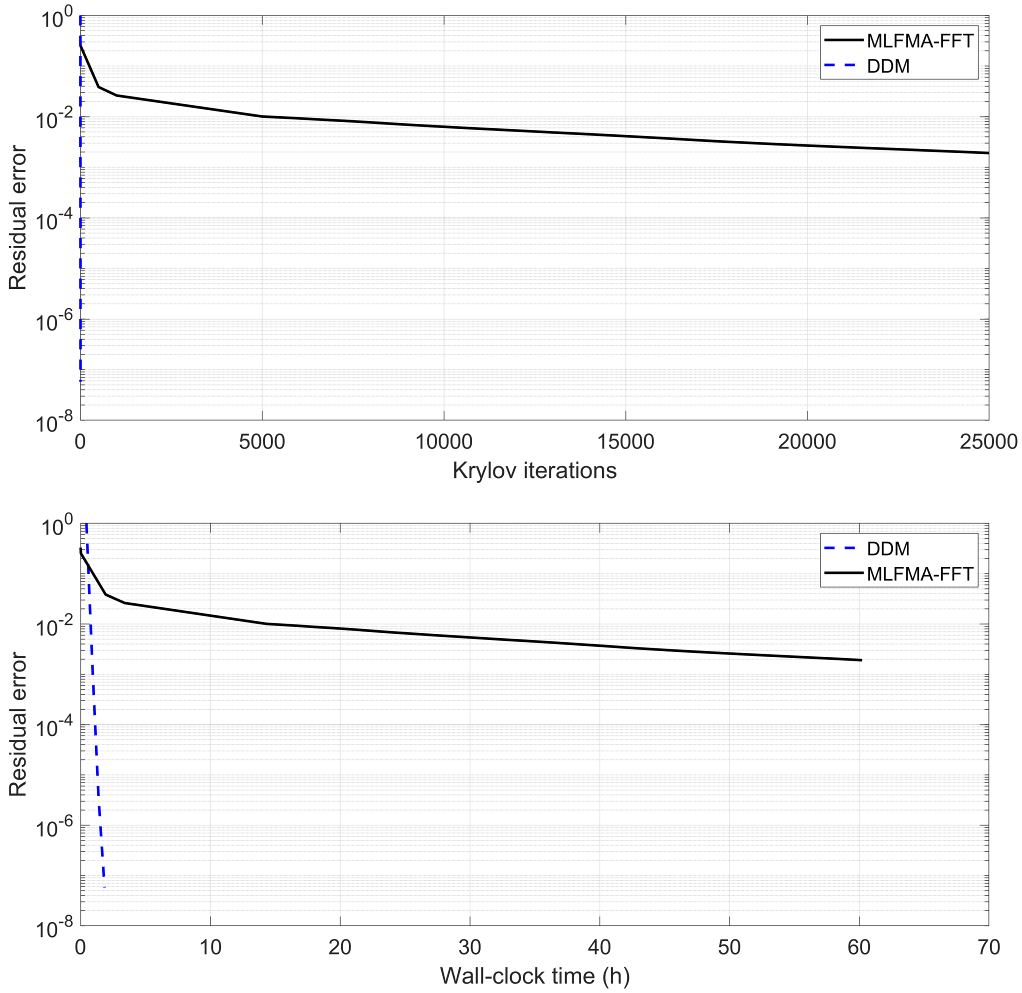

Figure 5.8: Convergence performance of the outer GMRES when solving the EMC problem of the vessel using the proposed SIE-DDM method and the MLFMA: (a) residual error versus number of iterations; (b) residual error versus time.

systems involved in the example (and considering fundamental emission and reception bands, out-of-band and spurious bands, as well as harmonic emission and image reception bands when applicable). For conciseness, the results shown below correspond only to one simulated frequency, 300 MHz, except for S_{12} parameters, which are displayed as a function of frequency covering the usual frequency band for communications in V/UHF.

Figure 5.8 compares the outer GMRES residual error of the DDM preconditioned system and the original matrix system in terms of the number of iterations and the wall-clock time employed to reach a certain convergence threshold (which is a better figure of merit). What stands out in this result is the excellent convergence of the proposed SIE-DDM approach, which takes 4 outer Krylov iterations and 1.8 hours of

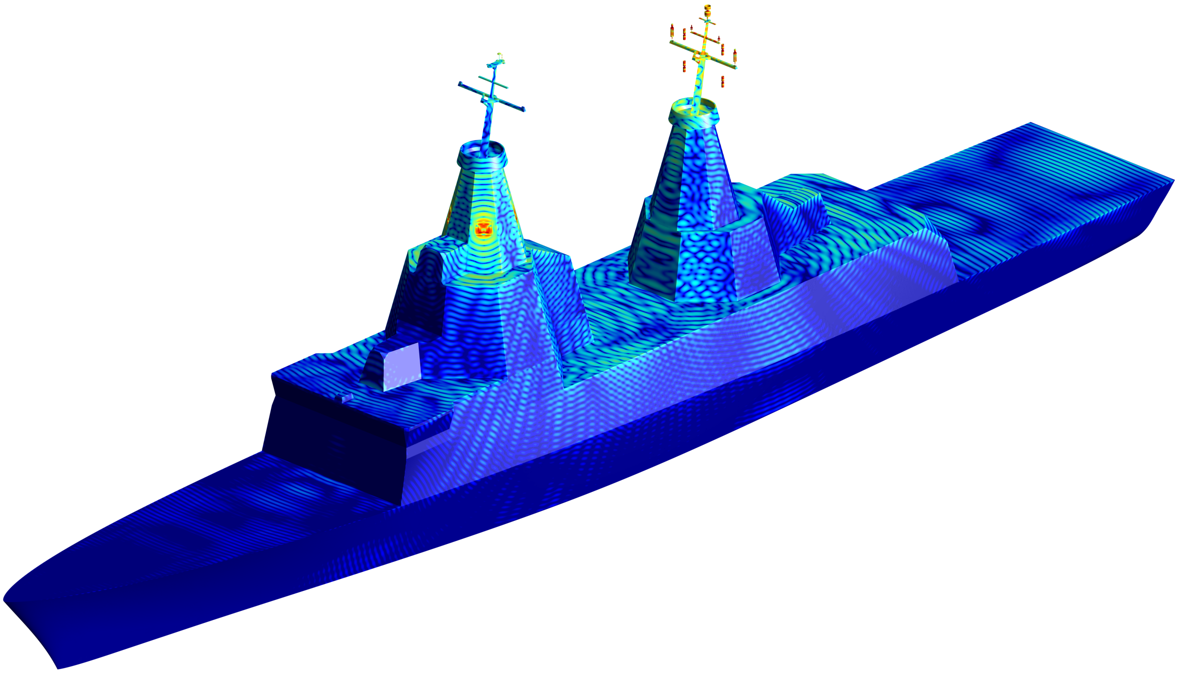

Figure 5.9: Real part of the equivalent electric surface current distribution ($dB\mu A/m$) on the vessel surfaces provided by the SIE-DDM approach.

simulation to converge to a residual error of $5 \cdot 10^{-8}$. This performance contrasts with the more than 25 000 iterations and the 60 hours spent by MLFMA to reach a residual error of just $2 \cdot 10^{-3}$. The above problem is a good example of how the concurrence of large and coarsely meshed objects (vessel superstructure) and radiating elements with local excitation and finely meshed details, slow down the convergence of the problem when using a global MLFMA. Otherwise, the rapid convergence of the DDM method to high precision solutions brings a major competitive advantage for the resolution of such kind of real EMC projects, in which, additionally to the obvious requirements in terms of precision, there are due dates to complete the study.

Figures 5.9 and 5.10 show the equivalent currents distribution in the vessel superstructure. From these currents, the S_{12} parameters accounting for the coupling among the antennas of the onboard communications systems are computed. As an example, the mutual coupling between antenna #3 and the onboard antennas sharing operating band is shown in Figure 5.11. Now, the interference margin matrices could be sequentially derived from the joint information provided by the S_{12} values and the specifications of the systems involved in the study (external filtering attenuations, RF and IF response, spurious emission and rejection, receiver sensibilities, etc.). These matrices lead to an easy evaluation of the potential EMC/EMI threats.

The computational statistics corresponding to this example can be looked up in Table 5.2, where the following information is shown for each augmented subdomain:

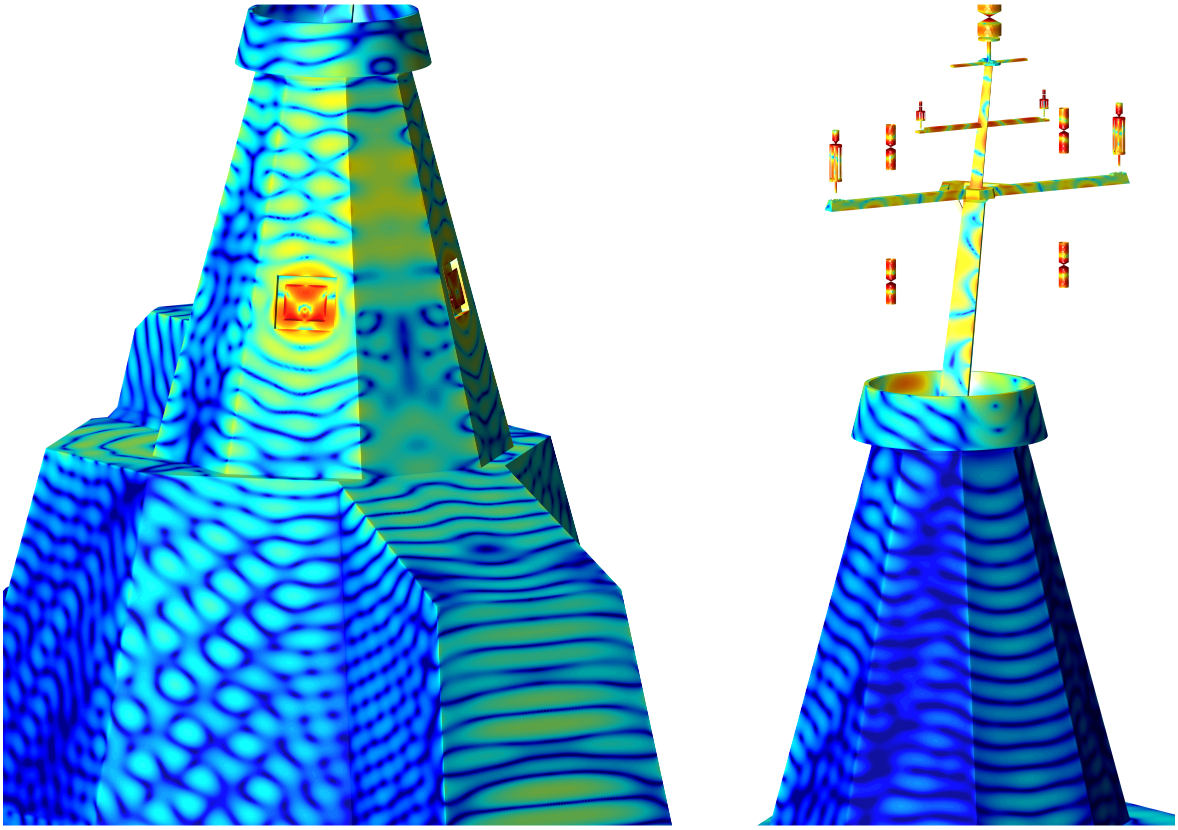

Figure 5.10: Zoom-in view of the current distribution ($dB\mu A/m$) on the masts around the antennas of the proposed vessel.

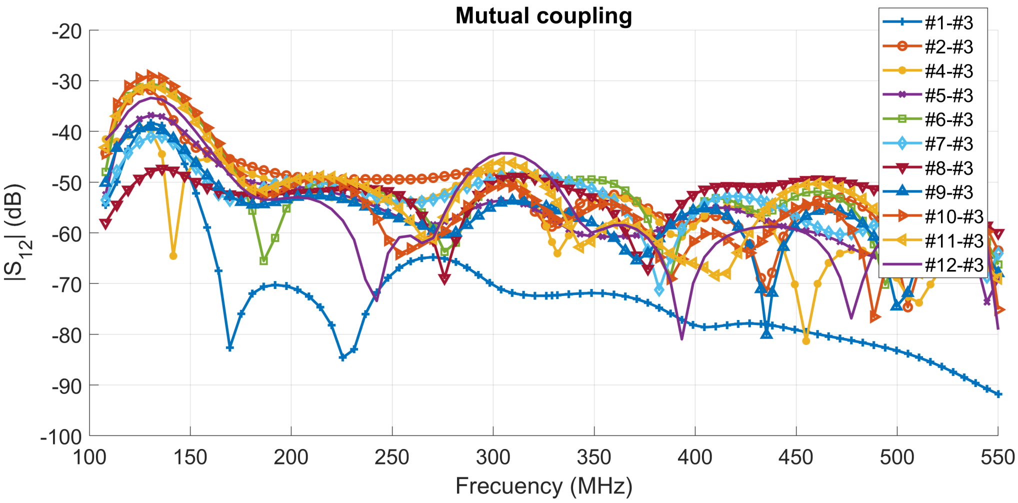

Figure 5.11: Mutual coupling (S_{12}) for the transmitting patch antenna #3 of the vessel in the frequency range from 108 to 550 MHz.

number of unknowns, memory consumption, setup time (consumed only once per frequency, at the beginning of the simulation), and the solving time, computed as the average of the solving times throughout all the external iterations.

Table 5.2: Computational metrics of subdomains in the simulation of vessel example

Domain	D_1	D_2	D_3	D_4
Unknows	64 575	480 887	992 569	64 314
Memory (GB)	1.4	9.6	19.2	1.3
Setup time (s)	8.28	38.66	73.34	8.6
Solving time (s)	9.22	71.7	74.6	9.08
Domain	D_5	D_6	D_7	D_8
Unknows	439 633	698 046	2 771 909	2 820 127
Memory (GB)	8.8	13.4	50.5	51.7
Setup time (s)	35.66	51.01	193.66	196.89
Solving time (s)	63.66	51.28	459.97	264.29
Domain	D_9	D_{10}	D_{11}	D_{12}
Unknows	2 881 272	2 770 883	18 147	18 147
Memory (GB)	52.9	51.9	5.8	5.8
Setup time (s)	200.91	193.66	97.8	97.8
Solving time (s)	299.12	459.97	0.33	0.33
Domain	D_{13}	D_{14}	D_{15}	D_{16}
Unknows	18 147	18 147	6 804	6 804
Memory (GB)	5.8	5.8	1.4	1.4
Setup time (s)	97.8	97.8	40.8	40.8
Solving time (s)	0.33	0.33	0.11	0.11
Domain	D_{17}	D_{18}	D_{19}	D_{20}
Unknows	4 320	4 320	2 498	2 498
Memory (GB)	0.6	0.6	0.2	0.2
Setup time (s)	18.43	18.43	3.72	3.72
Solving time (s)	0.05	0.05	0.03	0.03
Domain	D_{21}	D_{22}	D_{23}	
Unknows	2 498	2 498	2 384	
Memory (GB)	0.2	0.2	0.1	
Setup time (s)	3.72	3.72	3.38	
Solving time (s)	0.03	0.03	0.02	

5.1.3 Realistic Satellite

As a third example, let us consider a complex satellite by the European Space Agency, as illustrated in Fig 5.12. The dimensions of the satellite are approximately 20 m length, 7 m beam and 5 m height ($800\lambda \times 280\lambda \times 200\lambda$ at the working wavelength, λ). The detailed model of this structure includes four different communication systems as shown in Fig 5.12. The C-band and X-band communication systems consist of four horn antennas supported by two external arms (shown in the upper left corner of Fig 5.12) whose beam is directed by five reflectors. The K-band communication system consists of a complex array of horn antennas, which is shown in the lower right corner of Fig 5.12. The model is completed with two solar panels and the main structure supporting the described elements.

The DDM was applied in conjunction with the MR preconditioner to get an accurate prediction of the K-band system radiation at 12 GHz. A total of 60 267 853 unknowns were required to mesh the entire geometry, which exhibits deeply multiscale features, with a disparate mesh size ranging from $\lambda/20$ on smooth surfaces to $\lambda/1350$ in the vicinity of K-band antennas. This disparity in the mesh size results in poor conditioning, which in turn leads to lack of convergence unless proper simulation methodologies are applied.

For the analysis of this challenging structure, the entire problem was partitioned into 10 subdomains (as shown in Fig 5.12). This partitioning is done according to its natural features:

- Two large subdomains corresponding to the complete solar panels, far enough from the excitation domain, where it is assumed a smooth variation of the electric currents and fast convergence.
- Four subdomains for the four aperture antennas belonging to the different communication systems on the satellite.
- Two subdomains for the support arms of the upper communication systems, including its horn antennas.
- One subdomain for the main structure of the satellite.
- One subdomain for the excited array of antennas.

The subdomains are solved using 10 independent MLFMA-FFT solvers, with six levels for the support arms subdomains, five levels for the array antenna subdomain and eight levels for the rest. The intrinsic complexity of this structure is exacerbated

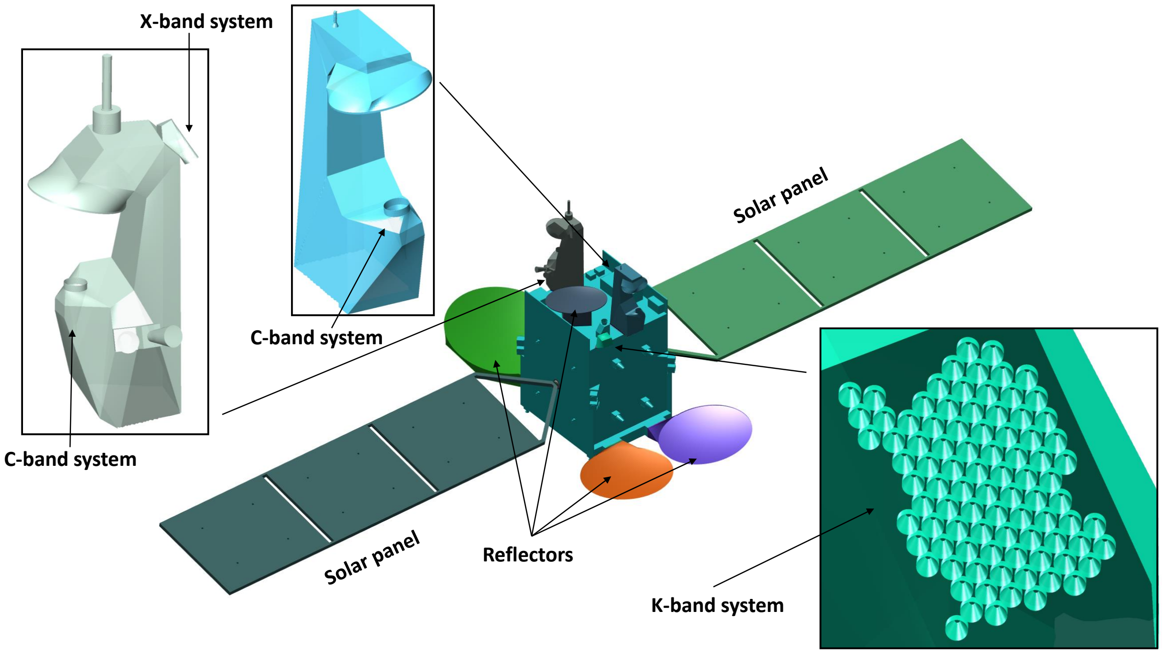

Figure 5.12: Partition into subdomains of the satellite.

by the presence of the large array with 90 horn antennas. The extremely intense mutual coupling between elements prevents in this case the use of 90 equal small MoM domains, which would allow taking advantage of the repetition pattern, relieving local calculations and memory consumption. But, due to the intense mutual coupling mentioned, this would be at the expense of the lack of convergence of the global iterative solver. Nevertheless, considering the complete array as an unique large subdomain is not without problems, since the strong interaction between the elements makes it necessary to include some kind of effective preconditioning (in this case, the MR preconditioner) to avoid slow convergence of this specific subdomain, which would become the bottleneck of the problem.

Fig 5.13 shows the residual error of the local iterative solution (at a given DDM iteration) of the subdomain corresponding to the horn array antenna using the MR preconditioned, compared with the Jacobi preconditioner. It can be observed that the MR preconditioner greatly reduces the iteration count for this multi-scale problem, thus enabling the solution of this challenging domain in the context of the DDM iterative resolution.

Fig 5.14 shows the residual error for whole problem using DDM for the two cases of local preconditioners mentioned in Fig 5.13. Although the outer Krylov convergence should be similar for both local preconditioner cases, the poor residual error posed by the Jacobi preconditioner impairs the outer GMRES convergence, thus ruining the accuracy of the solution. The final equivalent currents calculated applying DDM and

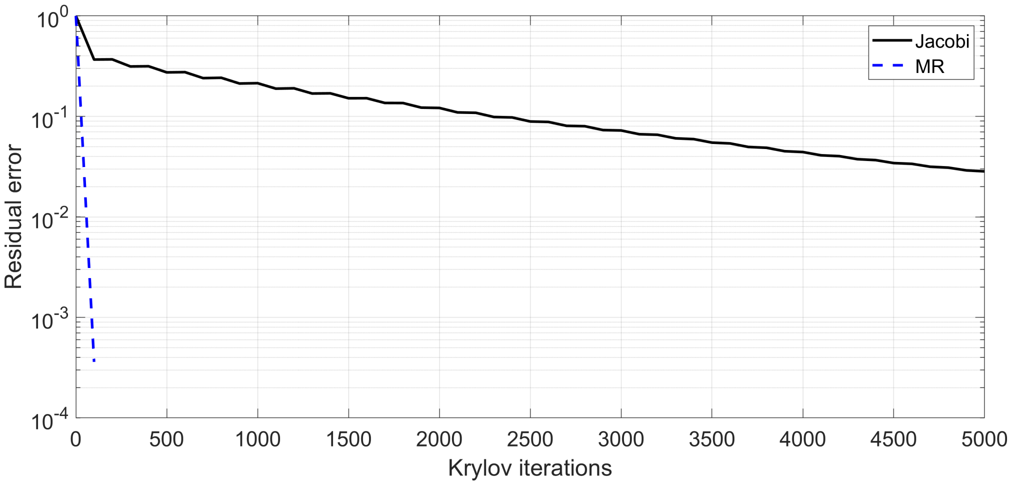

Figure 5.13: Convergence performance of the inner GMRES when solving one outer GMRES iteration of the array of antennas domain of the satellite using the proposed MR preconditioner method and the Jacobi preconditioner.

the MR preconditioner for the local horn array antenna subdomain is shown in Fig 5.15 for the sake of completeness.

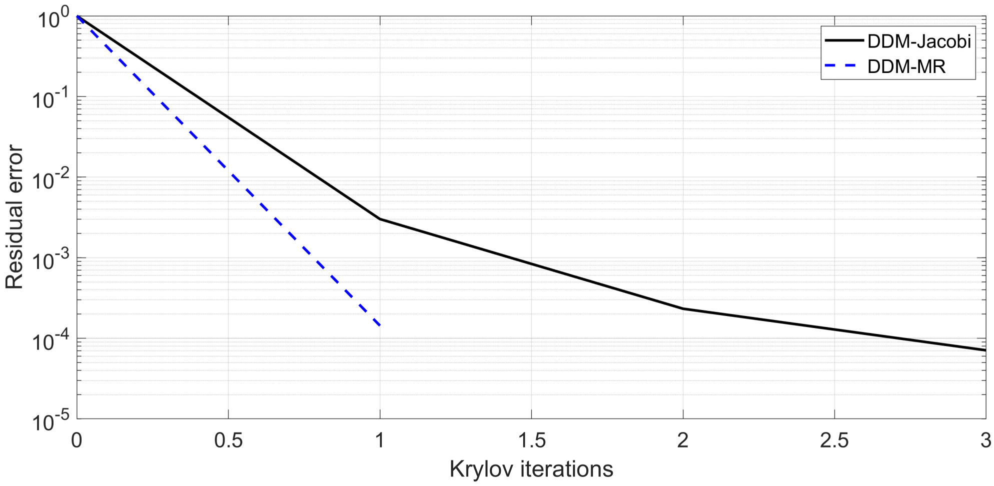

Figure 5.14: Convergence performance of the outer GMRES when solving the EMC problem of the satellite using the proposed MR and the Jacobi preconditioner in the local solver.

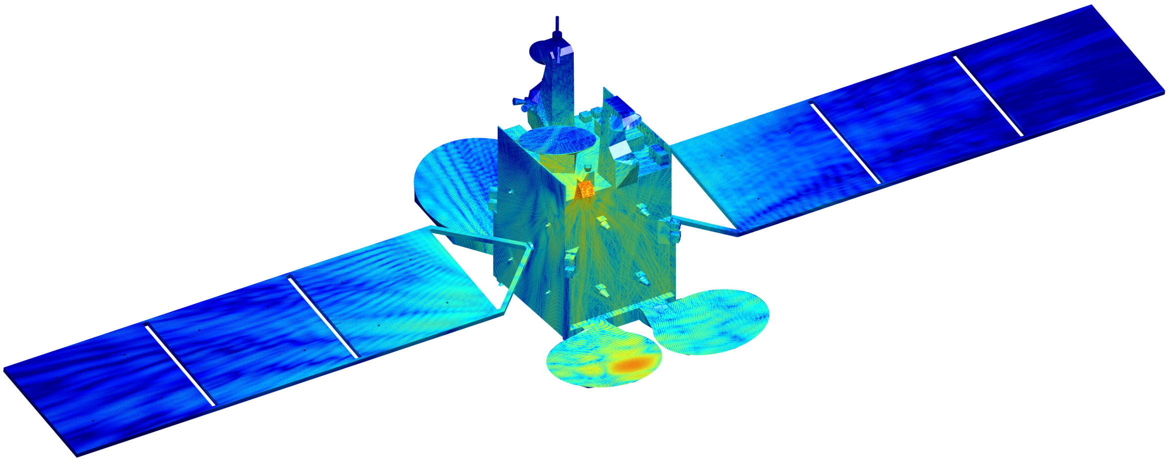

Figure 5.15: Real part of the equivalent electric surface current distribution $(dB\mu A/m)$ on satellite surfaces provided by the SIE-DDM approach.

5.1.4 Rafale aircraft

A different example is shown next. In the previous numerical examples, the focus of the use of non-conformal discretizations has been in transitions between different subdomains of a complex geometry, in the framework of a DDM solution. In this example, the usefulness of this approach for the application of h-refinement techniques is demonstrated, which allows increasing the degrees of freedom in those regions where there are fine geometric details or where higher precision is required. This naturally gives rise to non-conforming multi-scale problems with localized mesh refinement.

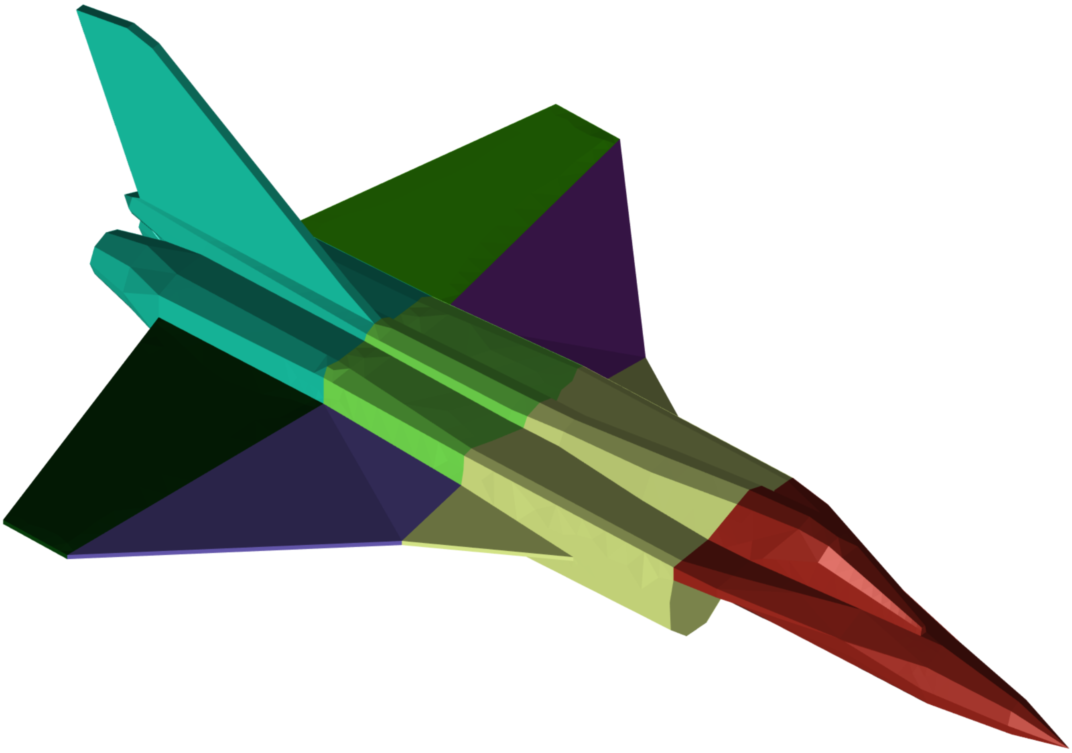

Figure 5.16: Partition into subdomains of the Rafale aircraft.

The Rafale aircraft is decomposed into eight DDM subdomains, as shown in Fig. 5.16. An automatic h-refinement method [115] is then applied to the input mesh of the different subdomains, with two steps of refinement, rendering a locally refined version that improves accuracy without burdening the computational cost. The final mesh obtained is shown in Fig. 5.17. The maximum length of the aircraft is 7λ, and the problem is modeled using 55 267 RWG basis functions in the conformal-mesh regions and 4 543 MB-RWG basis functions in the non-conformal mesh parts of the geometry.

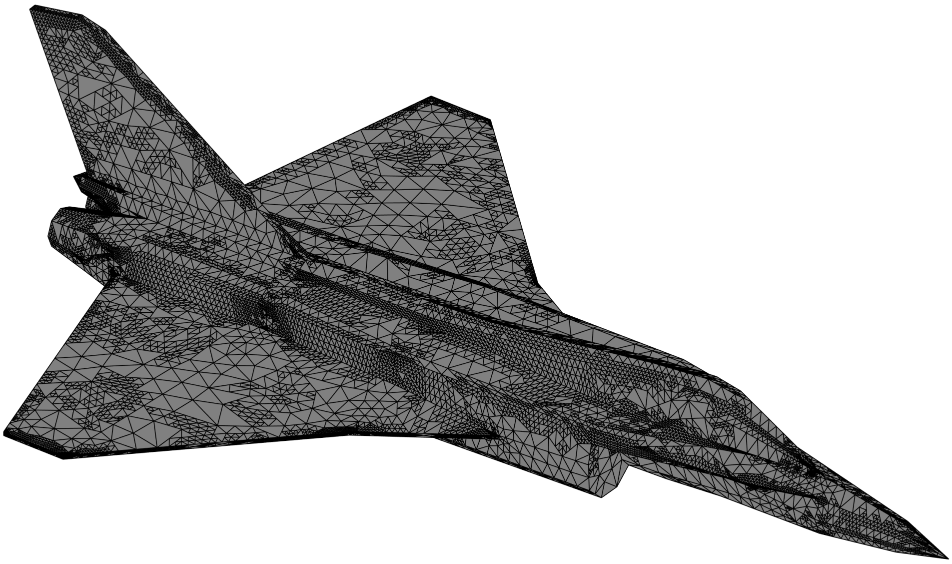

Figure 5.17: H-refinement non-conformal mesh of the proposed Rafale aircraft .

Figure 5.18 compares the GMRES residual error provided by the proposed MR-MB-RWG scheme with that provided by the Jacobi preconditioner, in both cases applying MLFMA for the solution of the h-refined subproblem corresponding to the airplane nose subdomain (see Fig. 5.16). An excellent convergence can be observed. The residual error for the complete problem is gathered in Fig 5.19, compared to that provided by the reference solution using conventional MLFMA. It can be observed looking at this figure that the combination of the MR preconditioner with the MB-RWG basis functions under a DDM resolution of the problem drastically reduces the global number of iterations, achieving a Krylov residual error below 10^{-6} in just 12 iterations.

Finally, the equivalent current distribution in the aircraft structure is shown in Fig. 5.20.

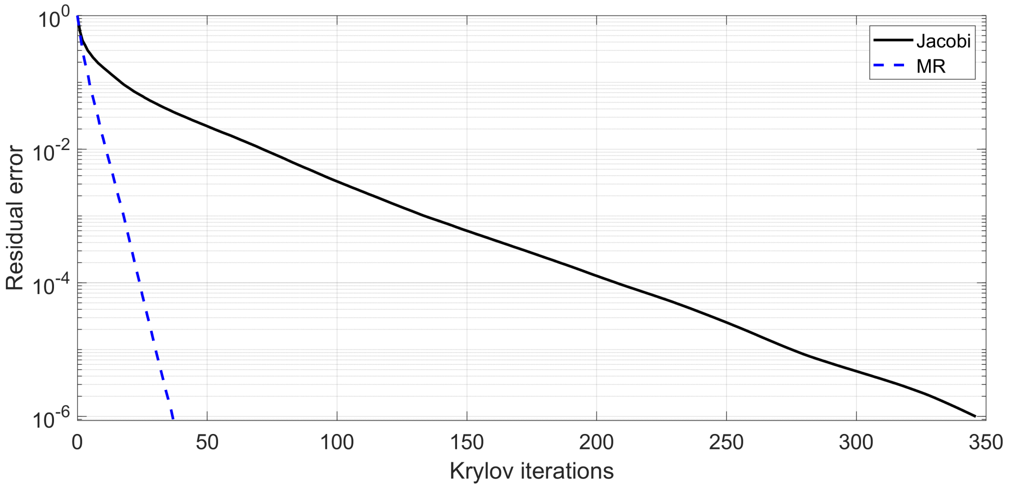

Figure 5.18: Convergence performance of the inner GMRES when solving one outer GMRES iteration of one domain of the Rafale aircraft using the proposed MR preconditioner method and the Jacobi preconditioner.

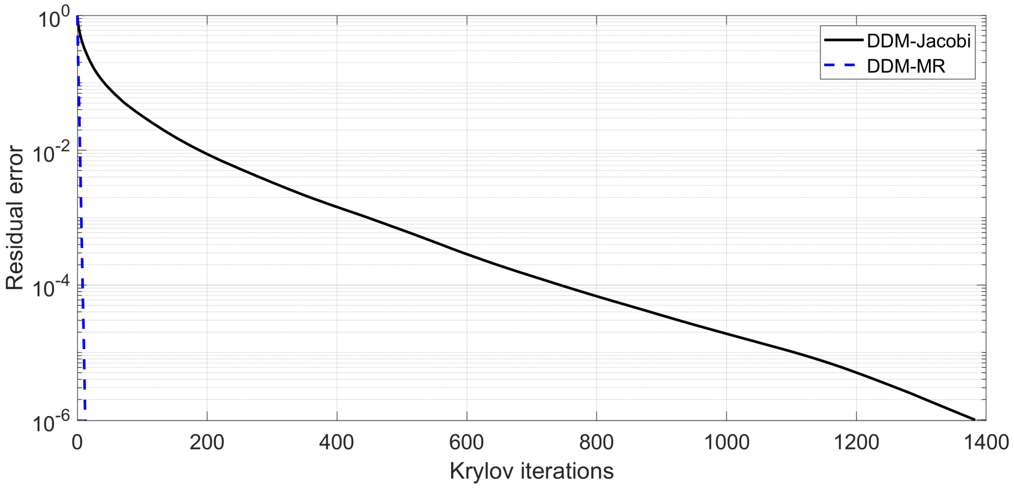

Figure 5.19: Convergence performance of the outer GMRES when solving the EMC problem of the Rafale aircraft using the proposed DDM-MB-MR and the Jacobi preconditioner for the entire problem.

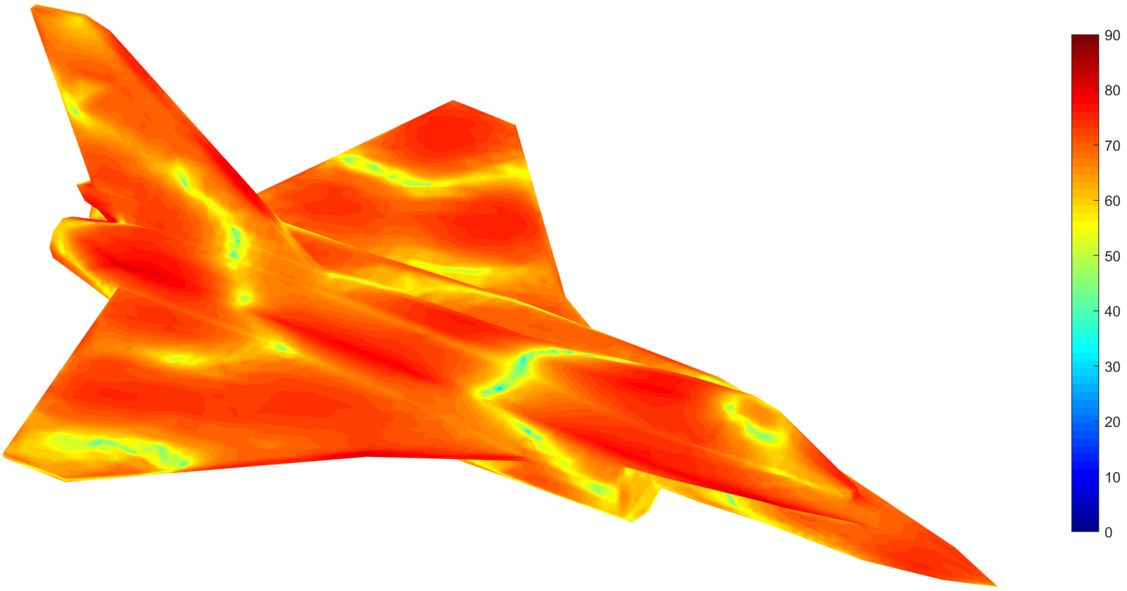

Figure 5.20: Equivalent electric currents ($dB\mu A/m$) induced on the aircraft surfaces.

5.2 Nanoplasmonic applications

This section gathers some results of application of the methodologies proposed in this thesis to the field of nanoplasmonics and biosensing. Raman spectroscopy is an important biosensing method for the identification of molecules in very low concentrations. This method consists of impinging onto a sample of analyte with a laser source. Most of the light absorbed by the sample is elastically scattered back at the same laser wavelength (Rayleigh scattering). However, a very small portion of the impinging energy is inelastically scattered posing a spectrum that depends on the energy differences between vibrational states of the molecule. Different molecules have different vibrational modes, so the spectrum of the inelastically scattered light yields a molecular fingerprint which uniquely identifies the interrogated molecule. The SERS enhancement of the otherwise extremely weak inelastic emission of molecules in the nearby of arrangements of metal nanoparticles supporting localized surface plasmon resonances (LSPRs) is a key factor for the ultrasensitive detection of a variety of organic molecules at low concentrations [116, 117].

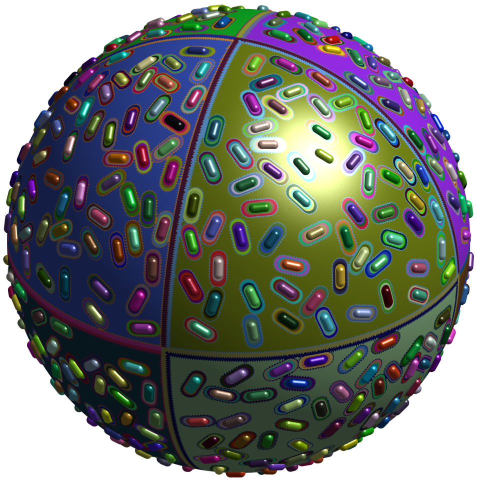

Figure 5.21: PS bead with embedded Au nanorods: Subdomains, inner and outer flaps.

5.2.1 Hybrid colloidal nanocomposite

As a first example, let us consider an assembly of Au nanorods (NR) onto a Polystyrene (PS) bead. The PS bead has a diameter of 400 nm and relative permittivity $\epsilon_r = 1.5$. The NRs have circular section and they are ended with spherical end-caps, with a diameter of 16 nm and a total length of 38 nm. The excitation of this problem is a normally impinging plane wave (laser) at 633 nm. The relative (dispersive) permittivity of gold at this wavelength is interpolated from the measurements of [118], being $\epsilon_r = -11.7522 - 1.2598i$. This kind of real-life hybrid dielectric/plasmonic system is of interest to surface-enhanced Raman scattering (SERS) chemical sensing of analytes, as they can directly interact with the NR surfaces [119]. The tunable Au NR density can be used to optimize the SERS efficiency of these hybrid nanomaterials. Nevertheless, the presence of multiple materials governed by a very different physics exhibiting rather high dielectric contrast, such as in this case the PS surface (dielectric) and the embedded gold nanorods (plasmonic at visible frequencies), poses a slow convergence of the iterative solver. The above is compounded by the fact that NRs are embedded onto the PS bead. Although the multiple-material junctions can be precisely modeled by the MR piecewise basis/testing functions, its presence hinders the already challenging multiphysics problem.

The DDM strategy was applied to overcome the potential lack of convergence, the complete problem is partitioned as sketched in Fig. 5.21(left). Considering first the large size of this system, it is split into 8 main subdomains, one for each octant. Next, considering the very different physical nature of the PS bead and the Au NRs, each NR (and its respective plasmonic-to-dielectric junction) is included into a different subdomain. In all, the domain decomposition procedure of this system with 496 Au NRs leads to 504 subdomains, 8 for the PS dielectric sphere and 496 for the NRs. Based on this decomposition, we apply different solvers tailored to the different subdomains. Subdomains 1 to 8 are solved iteratively via MLFMA-FFT, while the remaining subdomains (NRs) are solved by direct MoM factorization. In this particular case, as all the NRs are equal in shape and material, the same impedance matrix block is recycled for the calculations of the 496 NRs, thereby benefiting from the multiple repetitions (which is a usual feature of these nanosystems). Global interactions between subdomains are accelerated through parallel distributed MLFMA-FFT. The simulations were performed in a cluster with 4× Xeon E7-8867v3@2.5GHz (4×16 cores = 64 cores) and 1 TB of RAM memory.

The complexity of this analysis remains especially in the presence of LSPRs supporting very fast (subwavelength) field fluctuations. A high surface mesh density is considered for the Au NRs, with an edge size around 1/400 wavelengths, while about 1/20 wavelengths are required for the PS sphere. This poses a total of 6 754 224 unknowns for the electric and magnetic equivalent currents. The JMCFIE SIE formulation is applied, and a relative error norm of 10^{-6} is considered to halt the global Krylov iterative solver. Due to the tear-and-interconnect DDM transmission conditions, the subdomains are divided into different parts. The rod subdomains are extended to a small portion of the sphere around them, facilitating the calculation of junctions between domains. By doing so, the augmented sphere subdomain does not contain basis functions belonging to the nanorods, improving convergence. Additionally, all DDM junctions remain simple, since only two surfaces are involved in each case. Remarkably,

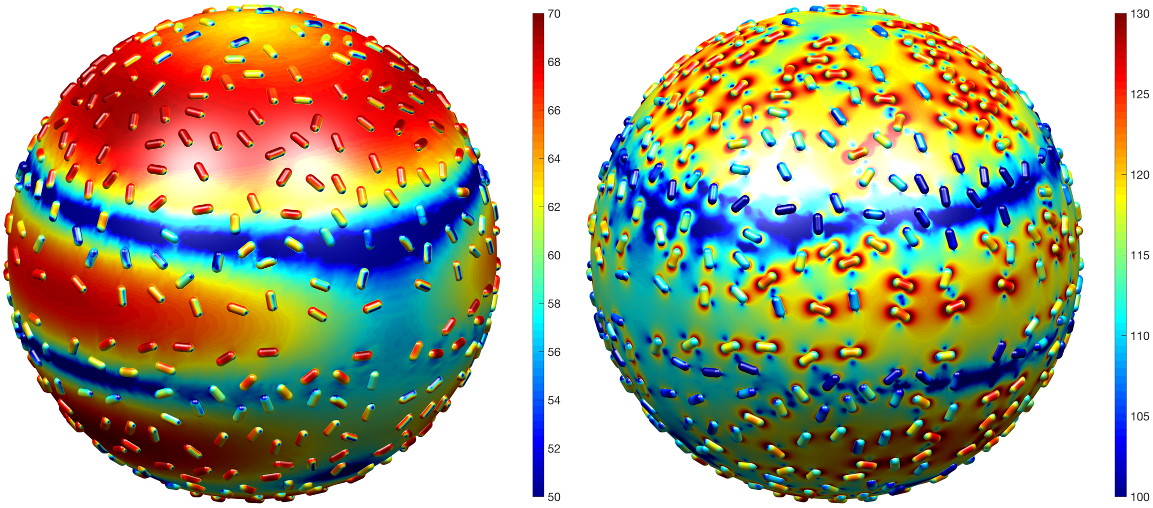

Figure 5.22: Equivalent electric and magnetic currents ($dB\mu A/m$) induced on the PS bead .

in this example we must solve a dielectric open problem (sphere with holes). Nevertheless, it must be pointed out again that the global problem we are solving is closed (due to the contributions from the RHS in DDM).

Looking at Fig. 5.23, it cab be observed that the above problem can be efficiently solved in reasonable time. A fast convergence is observed for the DDM solution, requiring only 35 outer Krylov iterations to attain a residual error below 10^{-6}. In comparison, MLFMA-FFT fails to reach the prescribed residual error within 200 iterations (posing a residual error above $5 \cdot 10^{-2}$). A larger picture is obtained by observing the wall-clock time convergence. In this real-life case, the proposed DDM method brings a definitive advantage both in terms of iteration count and solving time, enabling convergence and providing a solution with a high degree of accuracy in just over 5 hours. A solution of such precision would be very difficult to achieve using MLFMA-FFT (if even possible), as it begins to stagnate at high residual errors.

Finally, it can be observed looking at Fig. 5.22 that no artifacts are present in the equivalent currents. These currents flow smoothly through the tear lines between the different PS octants and between the PS and the NR subdomains. The use of DDM enables the solution of such multiphysics problem combining plasmonic and conventional dielectric materials, which are at the antipodes in terms of electromagnetic behavior.

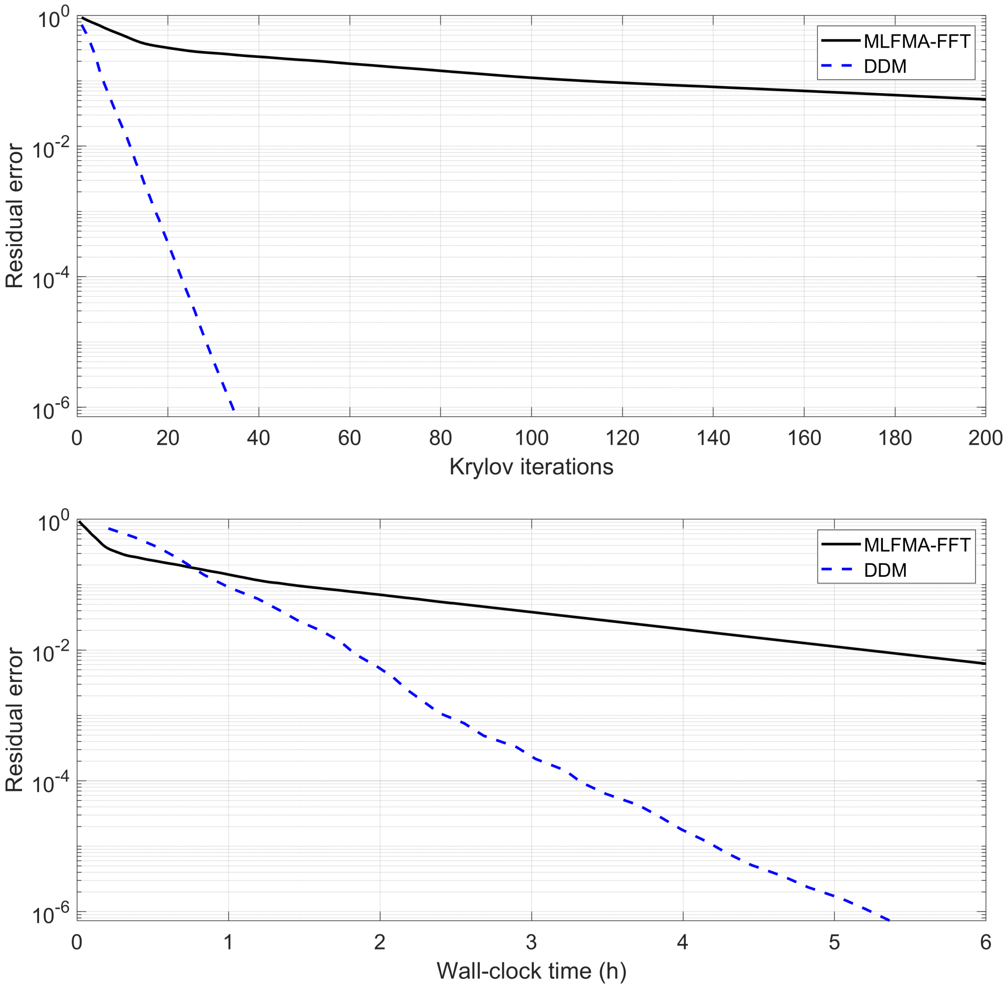

Figure 5.23: Iteration (up) count and wall-clock time (down) for the PS bead with embedded nanorods.

5.2.2 Gold Nanooctahedra plasmonic supercrystal for ultra-sensitive SERS

The next example is a plasmonic biosensor designed to improve the SERS for ultra-sensitive detection of different analytes related to biology, medicine, forensics, and environment analysis. The structure considered is a collection of 8 192 gold octahedra (75nm in length) organized hierarchically to form a densely packed supercrystal, as shown in Fig. 5.24. 33 128 448 unknowns (4 044 unknowns per element) are required to capture the physical phenomena produced by supercrystal. A small randomly generated self-rotation is included in the different octahedrons to account for the assembly errors in the actual synthesis procedure. The excitation consists of a focused beam through a lens on the center of the upper layer of the supercrystal, at a wavelength of 785nm, using the Novotny paraxial approximation [120].

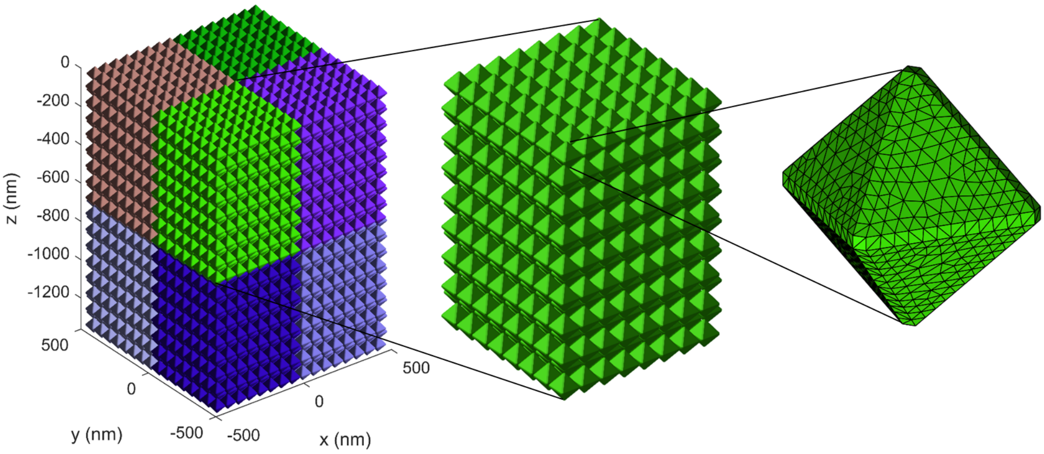

Figure 5.24: Gold Nanooctahedra geometry and domains

The main complexity of this example lies in the low distance between edges of different elements (as low as 1nm), producing intense interactions between nearby NP that increase the appearance of LSPRs. These strong interactions (posing a quasi-volumetric behavior) require complete octree cells under an MLFMA-FFT scheme, with the subsequent memory increase for the near interactions that burdens the solution or even make it impossible with reasonable computational resources. However, a problem of these characteristics can be perfectly addressed using the methods proposed and developed in this thesis.

A two-level DDM strategy was applied. At the coarsest level, eight subdomains are defined to capture the mutual coupling interactions between nearby blocks, as shown in Fig. 5.24 (left). At a finer level, one subdomain per element is considered to capture the physics of each nanoparticle. The periodicity of the proposed structure is exploited to reduce the memory consumption, by calculating the MoM matrix only once for the local solution of all the repeated elements at the finer level, as well as for the self-coupling interactions at the second level, where MLFMA-FFT is applied to speed-up the calculations. The simulations were performed in a cluster with 4 computational nodes of 4× Xeon E7-8867v3@2.5GHz (4×16 cores = 64 cores) and 1 TB of RAM memory each (a total of 256 cores and 4 TB of RAM). Two coarsest domains were distributed for each computational nodes.

Figs 5.25 and 5.26 show the residual error and the equivalent electromagnetic currents induced on the surfaces, respectively. Initially, we can not compare the convergence of DDM with other methods, since only DDM really enabled the analysis of this problem with the available resources. But DDM technology can be applied to reduce the computational resources required in the global MVP calculation required for an

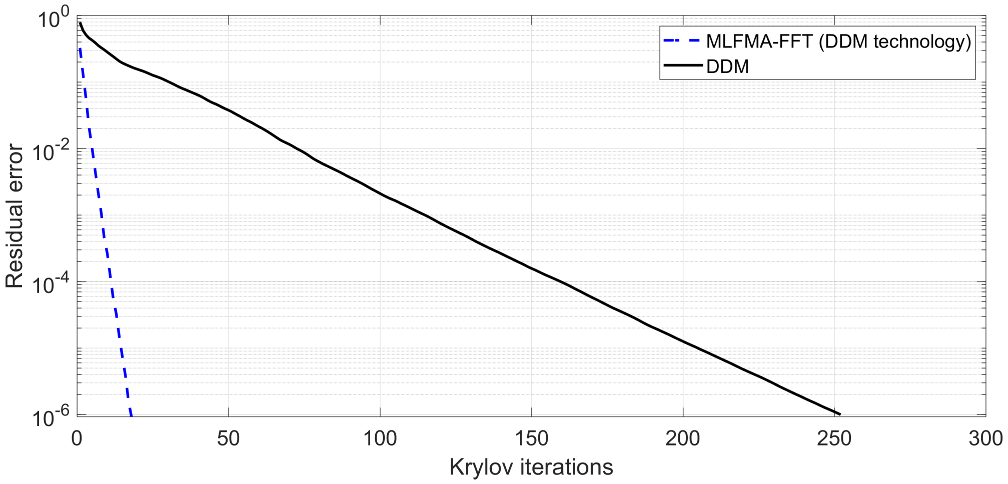

Figure 5.25: Gold Nanooctahedra iterative convergence

MLFMA-FFT without applying the DDM preconditioner. In any case, DDM still provides an accurate solution 10 times faster (a wall-clock time less than an hour) than this new MLFMA-FFT approach. Figure 5.26 shows the effect of the focused beam on the crystal, and how it propagates through the internal lattice.

The SERS enhancement factor for the electric near field is obtained to demonstrate the physical behaviour of the plasmonic biosensor. The SERS e enhancement factor can be calculated from simulation data as follows [121, 122]:

$$\text{E.F.} = \frac{|\mathbf{E}(\omega_{in})|^2}{|\mathbf{E}_i(\omega_{in})|^2} \frac{|\mathbf{E}(\omega_{out})|^2}{|\mathbf{E}_i(\omega_{out})|^2} \tag{5.1}$$

where $\mathbf{E}_i$ is the electric field of the incident laser and $\mathbf{E}$ is the total field in the presence of the nanoparticle assembly. The first term in (5.1) represents the local electric field intensity enhancement at the impinging frequency ω_{in}. The second term represents the local electric field intensity enhancement of the Raman inelastic scattering produced by the molecule sought. The calculation of the second term is done by reciprocity, repeating the simulation under a light excitation at the Raman-shifted (output) frequency ω_{out}. For low Raman shifts compared with ω_{in}, the following approximation can be applied, which avoids the need for a second simulation:

$$\text{E.F.} \approx |\mathbf{E}(\omega_{in})|^4 / |\mathbf{E}_i(\omega_{in})|^4. \tag{5.2}$$

This poses a fourth power dependence on the local electric field enhancement, which is why very high enhancements can be obtained using this technique.

Fig 5.27 represents the SERS of the biosensor. On the left, we can observe the normalized SERS of the total electric field. On the right, we show the SERS filtered

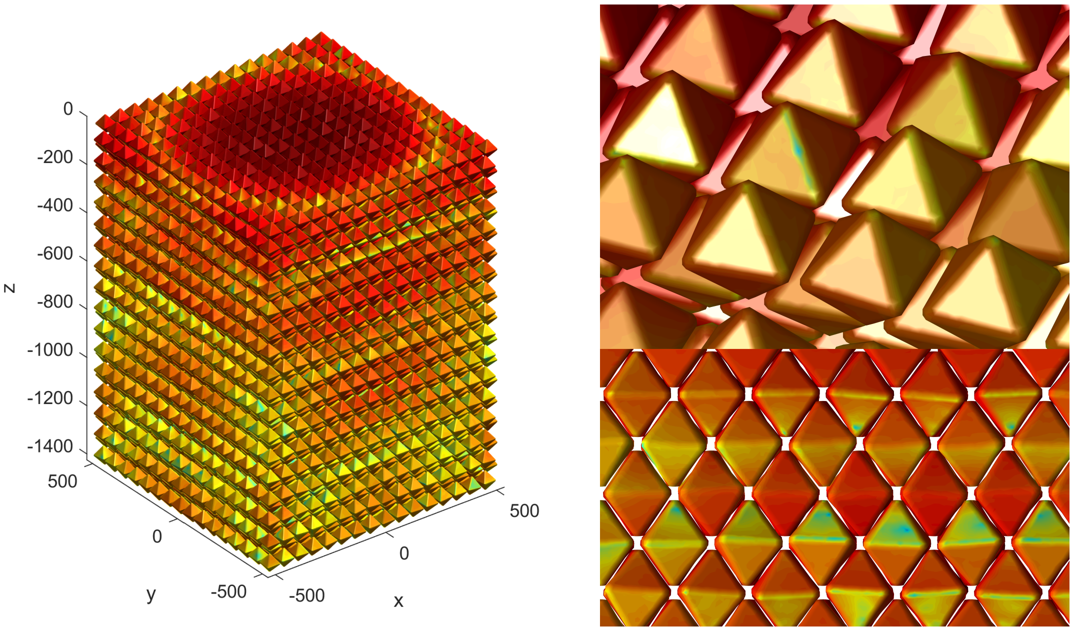

Figure 5.26: Equivalent electric and magnetic currents ($dB\mu A/m$) induced on Gold Nanooctahedra biosensor

with a gaussian function to simulate the effect of the objective lens used in the experimental measurements. In this figures, we can see how the light penetrates leading to a concentration at the crystal bottom, even given the small distance in wavelengths between elements.

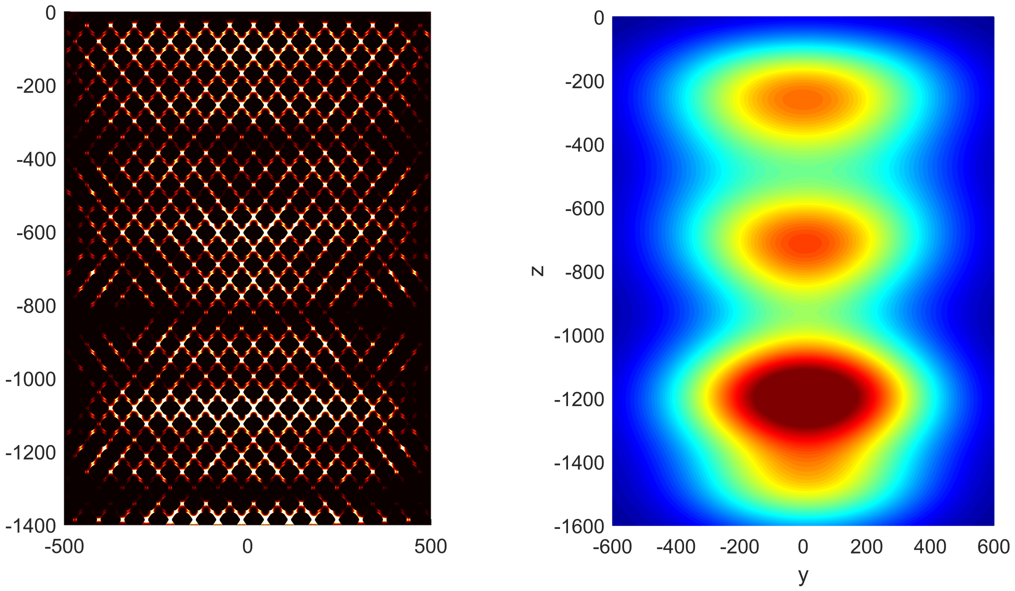

Figure 5.27: Gold Nanooctahedra SERS and filtered SERS

5.2.3 Gold nanocubes with silver incrustations embedded to a conventional substrate

A final numerical experiment is included to demonstrate the versatillity of the DG approach in combination with a DDM strategy to solve extremely complex multiscale structures in plasmonic applications. The example consists of a collection of 400 gold nanocubes with silver incrustations on the edges, connected to a conventional substrate. The nanocubes have a side length of 40 nm and are distributed posing small gaps of 3 nm between them. The geometry is shown in Fig. 5.28, and a detailed view of the mesh and the silver incrustations is depicted in Fig. 5.29. The cubes and substrate are tessellated separately and assembled back together, resulting in a nonconformal mesh with 5 187 138 basis functions, of which 5 153 538 are RWG basis functions defined on the inner conformal meshed surfaces, and 33 600 are half-RWG placed on the nonconformal tear lines. The DDM strategy was applied in conjunction with the DG, thus guaranteeing the current flow across the non-conformal tearing lines. The problem is decomposed into 401 overlapping subdomains (one substrate with length size of 800 nm and 400 for the nano-cubes). The excitation consists of a plane-wave impinging from above at a wavelength of 633 nm. The JMCFIE-DG formulation was applied with an interior penalty stabilization parameter $\beta = 50$. The setup time was approximately 2.8 hours, while it took 5.86 hours and 441 iterations for the iterative solver to achieve a low relative error on the equivalent currents, below 10^{-6}, on a computing server with 128 parallel cores.

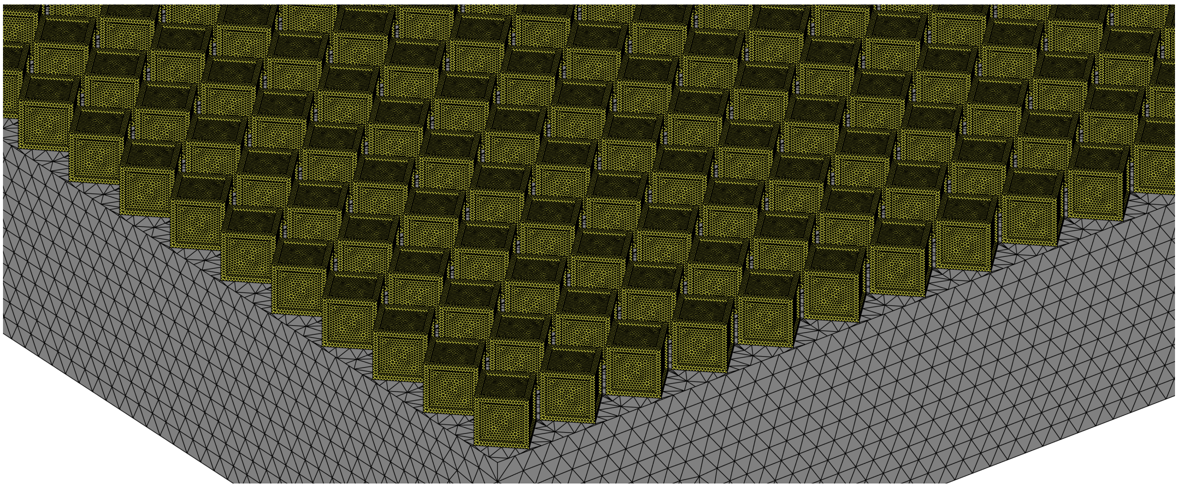

Figure 5.28: Plasmonic Au nanocubes with Ag depositions over dielectric substrate

Fig. 5.30 show the equivalent electric currents on the external boundary surfaces of the gold nanocubes and the substrate. Remarkably, no discontinuities or artifacts are appreciated, revealing that the currents flow perfectly through the nonconforming tear lines.

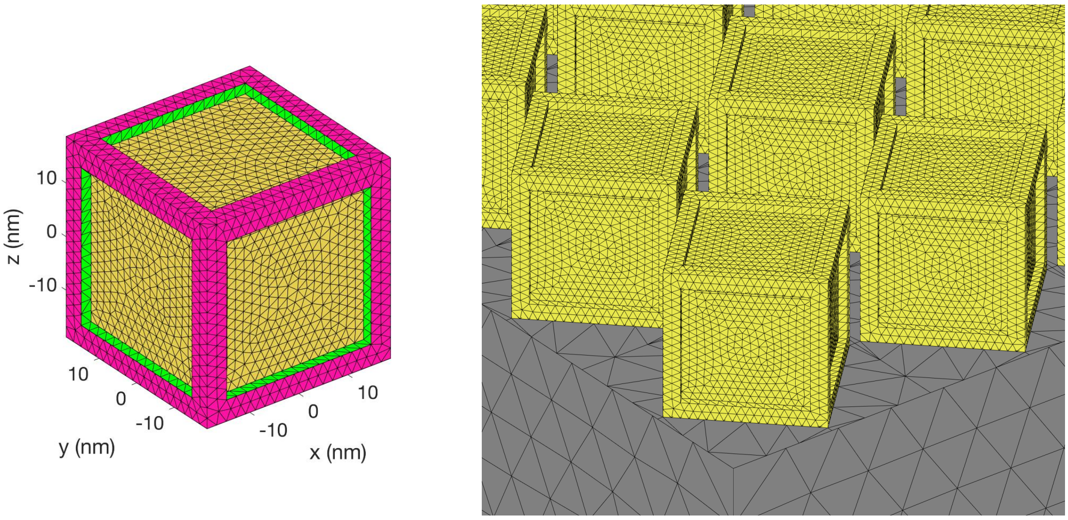

Figure 5.29: Detail view of plasmonic Au nanocubes non-conformal meshes

Finally, the SERS enhancement factor of Fig. 5.31 was obtained for the assembly of nanocubes on a horizontal plane that intersects the nanocubes, placed at a distance of 40 nm above the substrate. The enhancement factor is calculated here using the approximated formula of (5.2) for a plane wave (laser) normally impinging in the $-\hat{z}$ direction. Both the $\hat{x}$ and $\hat{y}$ polarization directions are considered and the respective results are averaged. As expected, high enhancement factors ($> 10^5$) can be observed in hot-spots occurring in the gaps between adjacent nanoparticles of the assembly, which arise due to mode hybridization.

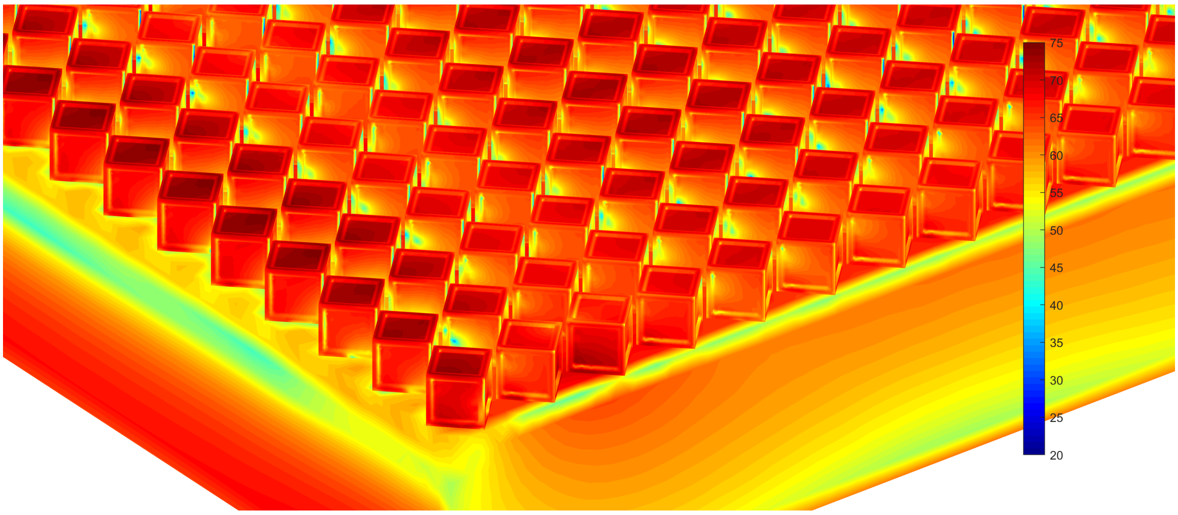

Figure 5.30: Equivalent electric currents ($dB\mu A/m$) on non-conformal surfaces of the plasmonic Au nanocubes depositions.

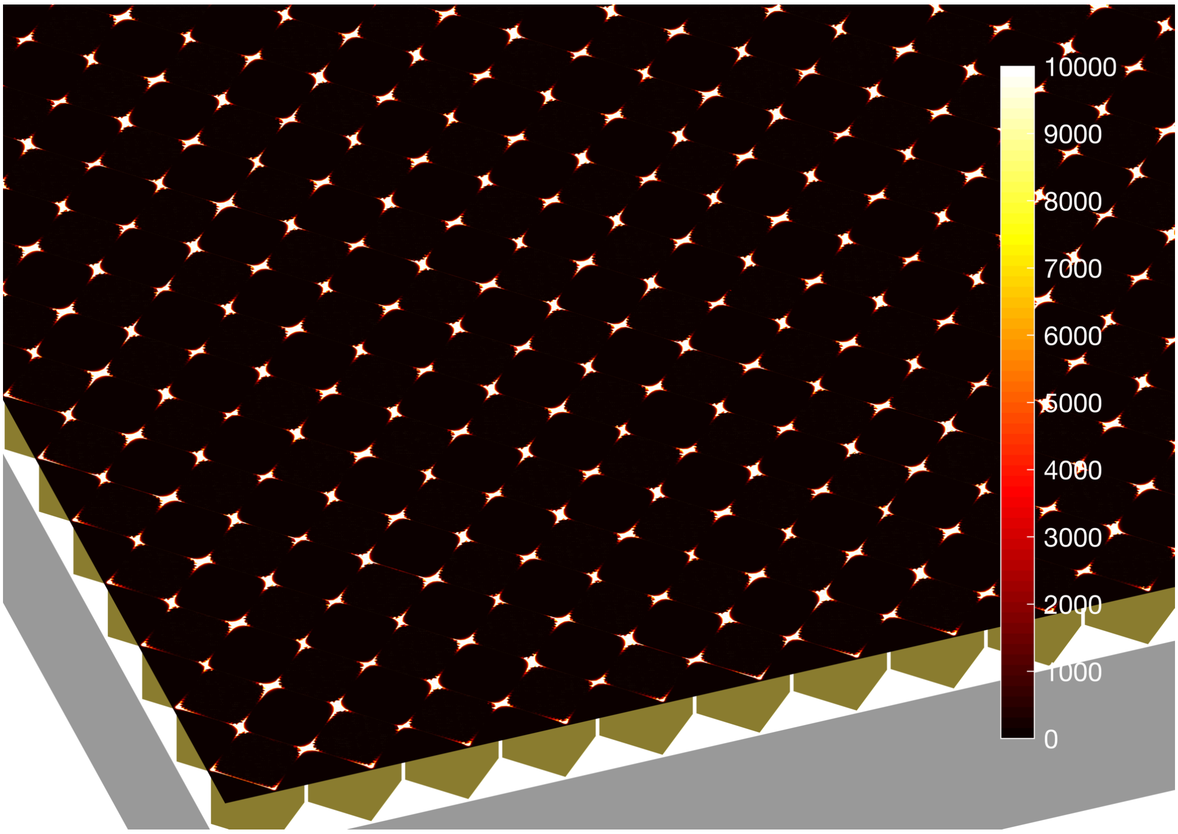

Figure 5.31: SERS enhancement factor for the assembly of figure 5.28 calculated on a horizontal plane placed at a distance of 40 nm above the substrate.

Chapter 6

Conclusion and future lines

6.1 Conclusion

The work developed in this thesis can be classified into three main lines. First, a multisolver tear-and-interconnect DDM has been developed in the context of the SIE for the efficient solution of very complex and large-scale radiation and scattering problems exhibiting deep multiscale features. This method is supported by a stable and compact methodology that unifies the treatment of surfaces, interfaces, and junctions, enabling the combination of different formulations (CFIE, EFIE, JMCFIE, etc.) including arbitrarily shaped junctions between different materials. The tear-and-interconnect strategy allows the partition of the entire problem into locally solved subproblems, according to their physical and geometrical properties. These subproblems can be addressed using local independent solvers tailored to the particular characteristics and needs, and taking advantage of pattern repetitions through the inherent divide-and-conquer strategy of the DDM framework. Moreover, efficient and accurate fast algorithms were also included to obtain the accelerated solution of the mutual coupling between subdomains. A novel highly-scalable parallel implementation of MLFMA-FFT combined with MR-ILU was proposed. The hierarchical nature of the multiresolution base functions has been exploited in the implementation through the use of efficient algorithms for the storage and calculation of SpMVPs and the efficient application of the PARDISO solver. The efficiency and accuracy of the proposed methods was demonstrated through the solution of challenging numerical examples.

The versatility of the proposed method was then improved through the devising and development of non-compliant SIE techniques based on DG, as well as applying the novel MB-RWG basis functions. One technology or the other (or both at the same time) will be applied depending on the needs of each subdomain. The proposed JMCFIE-DG formulation brings great flexibility to the application of the DDM in real-life problems, whose CAD models can be built and tessellated independently for the different parts of the geometry without caring about mesh conformity. Additionally, by applying DG we effectively solved the awkward issue of junctions between three or more materials. Normal current continuity is satisfied by the combination of the boundary conditions at the meeting surfaces (wired to the JMCFIE formulation), and the weak interior penalty condition independently applied inside the different regions defining the junction. This greatly simplifies the formulation for the general case, avoiding any especial action by the end user for this particular case. Numerical experiments were included to investigate the optimal choice of the interior penalty stabilization parameter and to demonstrate the versatility and accuracy of the proposed methods.

Finally, the quasi-Helmholtz multi-resolution preconditioner was combined with the multi-branch RWG functions for the electromagnetic analysis of non-conformal meshes, enabling the application of h-refinement techniques in the case of problems including deep multi-scale features. This provides an efficient, accurate and versatile solver for dealing with very large-scale and extremely complex geometries. Furthermore, due to the multilevel quasi-Helmholtz decomposition posed by this method, it could be applied to improve convergence in multiscale non-conformal problems suffering from low-frequency breakdown issues.

The complete set of devised and implemented simulation tools has been applied to solve different real-life challenging problems in EMC/EMI and plasmonics applications. Each of these examples shows various capabilities and possible configurations of the multipurpose methodology developed in this thesis.

6.2 Future lines

The enormous potential and versatility of the methods developed in this thesis offers a wide repertoire of possible improvements to continuously guide the simulation methodologies to the needs of the industry and research centers. The intrinsic nature of the domain decomposition methods to independently tackle the different parts of a challenging problem facilitates the easy combination of new solvers to undertake new problems. In addition, our hybrid MPI/OpenMP implementation of DDM allows to take advantage of the latest (and likely future) advances in HPC.

Four main lines of action can be distinguished to prepare the developed methodologies for the near future. First, the development of new solvers to exploit the natural properties of new kind of problems can be considered, e.g. the combination of accelerated MoM solvers as slottFFT [123] to optimally address the periodicity of finite periodic structures.

Although the SIEs have emerged as a powerful tool in CEM, the development of a hybrid implementation with finite element methods can be very useful to efficiently deal with complex antennas or coated layers of inhomogeneous materials. In this context, the accelerated near field radiation method devised in this thesis for the global MVP enables the easily combination of non-SIE methods as local solvers in the DDM. Furthermore, advances in iterative physical optics (IPO) algorithms can be added to optimize the solution of extremely large domains whose interactions can be approximated with asymptotic methods.

As a second line, the tear and interconnect DDM can be combined with other DD technologies to further exploit the geometric and physical properties of different subsystems. Especially, the Robin type transmission conditions and the multitrace methods [45] allow the efficient treatment of composite multimaterial subdomains (by overlapping different interfaces with different discretizations) without need of flaps in the connection between subdomains. This DD paradigm is especially convenient to split embedded and different material domains in a superstructure. In addition, the equivalent principle algorithm (EPA) [124] can be combined with the multitrace methods in the mutual coupling procedure of the DDM to develop a truly multisolver method capable of handling extremely different domains even in the global MVP calculation. Moreover, the combination of EPA and multitrace methods transform the global MVP step into a finite periodic problem, that can be accelerated through the proper algorithms.

The third line of work is the optimization of the DDM implementation taking into account the mathematical properties of the algorithms in two directions. The development of recycling Krylov subspaces to reduce the iteration counts of the outer GMRES, and the incorporation of algorithms to optimize the choice of subdomains.

Finally, different steps in the DDM procedure can be accelerated by using massive parallelization via graphics processing units (GPUs).

Bibliography

[1] R. F. Harrington. *Field Computation by Moment Method.* NJ, USA: IEEE Press, 1993.

[2] S. M. Rao, D. R. Wilton, and A. W. Glisson. Electromagnetic scattering by surfaces of arbitrary shape. *IEEE Transactions on Antennas and Propagation*, 30(3):409–418, may 1982.

[3] Roger F. Harrington. Boundary integral formulations for homogeneous material bodies. *Journal of Electromagnetic Waves and Applications*, 3(1):1–15, 1989.

[4] J. Song and W. C. Chew. Multilevel fast multipole algorithm for solving combined field integral equations of electromagnetic scattering. *Microw. Opt. Tech. Lett.*, 10(1):14–19, 1995.

[5] B. Stupfel. A fast-domain decomposition method for the solution of electromagnetic scattering by large objects. *IEEE Transactions on Antennas and Propagation*, 44(10):1375–1385, 1996.

[6] F. Andriulli, K. Cools, F. Olyslager, A. Buffa, S. Christiansen, and E. Michielssen. A multiplicative Calderon preconditioner for the electric field integral equation. *IEEE Transactions on Antennas and Propagation*, 56(8):2398–2412, aug 2008.

[7] Xiaochuan Wang, Zhen Peng, Kheng-Hwee Lim, and Jin-Fa Lee. Multisolver domain decomposition method for modeling emc effects of multiple antennas on a large air platform. *IEEE Transactions on Electromagnetic Compatibility*, 54(2):375–388, 2012.

[8] Andrew J. Hesford and Weng C. Chew. On preconditioning and the eigensystems of electromagnetic radiation problems. *IEEE Transactions on Antennas and Propagation*, 56(8):2413–2420, 2008.

[9] F. Obelleiro, J. M. Taboada, J. L. Rodríguez, J. O. Rubiños, and A. M. Arias. Hybrid moment-method physical-optics formulation for modeling the electromagnetic behavior of on-board antennas. *Microwave and Optical Technology Letters*, 27(2):88–93, 2000.

[10] Tim H. Taminiau, Robert J. Moerland, Frans B. Segerink, Laurens Kuipers, and Niek F. van Hulst. /4 resonance of an optical monopole antenna probed by single molecule fluorescence. *Nano Letters*, 7(1):28–33, 2007. PMID: 17212435.

[11] Palash Bharadwaj and Lukas Novotny. Spectral dependence of single molecule fluorescence enhancement. *Opt. Express*, 15(21):14266–14274, Oct 2007.

[12] F. Obelleiro, J. M. Taboada, D. M. Solís, and L. Bote. Directive antenna nanocoupler to plasmonic gap waveguides. *Opt. Lett.*, 38(10):1630–1632, May 2013.

[13] F. Obelleiro, J.M. Taboada, J.L. Rodriguez, and J.M. Bertolo. Hemcuvi: a software package for the electromagnetic analysis and design of radiating systems on board real platforms. *IEEE Antennas and Propagation Magazine*, 44(5):44–61, 2002.

[14] Inés García-Tuñón Blanca, José Luis Rodríguez, Fernando Obelleiro, José M. Taboada, José M. Núñez, and Daniel Cortina. Experience on radar cross section reduction of a warship. *Microwave and Optical Technology Letters*, 56(10):2270–2273, 2014.

[15] Weng Cho Chew, Mei Song Tong, and Bin Hu. Integral equation methods for electromagnetic and elastic waves. *Synthesis Lectures on Computational Electromagnetics*, 3(1):1–241, 2008.

[16] Zhen Peng, Kheng-Hwee Lim, and Jin-Fa Lee. Nonconformal domain decomposition methods for solving large multiscale electromagnetic scattering problems. *Proceedings of the IEEE*, 101(2):298–319, 2013.

[17] Mao-Kun Li and Weng Cho Chew. Multiscale simulation of complex structures using equivalence principle algorithm with high-order field point sampling scheme. *IEEE Transactions on Antennas and Propagation*, 56(8):2389–2397, 2008.

[18] Feng Hao, Colleen L. Nehl, Jason H. Hafner, and Peter Nordlander. Plasmon resonances of a gold nanostar. *Nano Letters*, 7(3):729–732, 2007. PMID: 17279802.

[19] Jian-Ming Jin. *The Finite Element Method in Electromagnetics.* SIAM, NJ, USA: Wiley, 2002.

[20] Shunping Zhang, Kui Bao, Naomi J. Halas, Hongxing Xu, and Peter Nordlander. Substrate-induced fano resonances of a plasmonic nanocube: A route to increased-sensitivity localized surface plasmon resonance sensors revealed. *Nano Letters*, 11(4):1657–1663, 2011.

[21] José M. Taboada, Javier Rivero, Fernando Obelleiro, Marta G. Araújo, and Luis Landesa. Method-of-moments formulation for the analysis of plasmonic nano-optical antennas. *J. Opt. Soc. Am. A*, 28(7):1341–1348, Jul 2011.

[22] Fernando Obelleiro, José M. Taboada, and Marta G. Araújo. Calculation of wave propagation parameters in generalized media. *Microwave and Optical Technology Letters*, 54(12):2731–2736, 2012.

[23] J. Rivero, J. M. Taboada, L. Landesa, F. Obelleiro, and I. García-Tu nón. Surface integral equation formulation for the analysis of left-handed metamaterials. *Opt. Express*, 18(15):15876–15886, Jul 2010.

[24] Javier Rivero Marta Gomez Araujo, Jose Taboada and Fernando Obelleiro. Comparison of surface integral equations for left-handed materials. *Progress In Electromagnetics Research*, 118:425–440, 2011.

[25] M. G. Araújo, J. M. Taboada, D. M. Solís, J. Rivero, L. Landesa, and F. Obelleiro. Comparison of surface integral equation formulations for electromagnetic analysis of plasmonic nanoscatterers. *Opt. Express*, 20(8):9161–9171, Apr 2012.

[26] M. G. Araújo, J. M. Taboada, J. Rivero, D. M. Solís, F. Obelleiro, and L. Landesa. Electromagnetic analysis of metamaterials and plasmonic nanostructures with the method of moments. *IEEE Antennas and Propagation Magazine*, 54(6):81–91, 2012.

[27] Diego M. Solís, José M. Taboada, Fernando Obelleiro, Luis M. Liz-Marzán, and F. Javier García de Abajo. Toward ultimate nanoplasmonics modeling. *ACS Nano*, 8(8):7559–7570, 2014.

[28] Diego M. Solís, José M. Taboada, Fernando Obelleiro, and Luis Landesa. Optimization of an optical wireless nanolink using directive nanoantennas. *Opt. Express*, 21(2):2369–2377, Jan 2013.

[29] Polman A. Atwater, H. Plasmonics for improved photovoltaic devices. *Nature Mater*, (9):205–213, 2010.

[30] Halas NJ Payne JD West JL. O'Neal DP, Hirsch LR. Photo-thermal tumor ablation in mice using near infrared-absorbing nanoparticles. *Cancer Lett*, 209:171–176, 2004.

[31] Jatish Kumar, Hasier Eraña, Elena López-Martínez, Nathalie Claes, Víctor F. Martín, Diego M. Solís, Sara Bals, Aitziber L. Cortajarena, Joaquín Castilla, and Luis M. Liz-Marzán. Detection of amyloid fibrils in parkinson's disease using plasmonic chirality. *Proceedings of the National Academy of Sciences*, 115(13):3225–3230, 2018.

[32] Daniel García-Lojo, Sergio Gómez-Graña, Víctor F. Martín, Diego M. Solís, José M. Taboada, Jorge Pérez-Juste, and Isabel Pastoriza-Santos. Integrating

plasmonic supercrystals in microfluidics for ultrasensitive, label-free, and selective surface-enhanced raman spectroscopy detection. *ACS Applied Materials & Interfaces*, 12(41):46557–46564, 2020.

[33] Sara Gullace, Verónica Montes-García, Victor Martín, David Larios, Valentina Girelli Consolaro, Fernando Obelleiro, Giuseppe Calogero, Stefano Casalini, and Paolo Samorì. Universal fabrication of highly efficient plasmonic thin-films for label-free sers detection. *Small*, 17(33):2100755, 2021.

[34] Rashid Zia, Jon A. Schuller, Anu Chandran, and Mark L. Brongersma. Plasmonics: the next chip-scale technology. *Materials Today*, 9(7):20–27, 2006.

[35] Sorger V. Zentgraf T. et al. Oulton, R. Plasmon lasers at deep subwavelength scale. *Nature*, 461:629–632, 2009.

[36] Zhu G. Belgrave A. et al. Noginov, M. Demonstration of a spaser-based nanolaser. *Nature*, 460:1110–1112, 2009.

[37] Mukherjee A. Yu C. et al Akimov, A. Generation of single optical plasmons in metallic nanowires coupled to quantum dots. *Nature*, 450:402–406, 2007.

[38] Diego M. Solís, José M. Taboada, Fernando Obelleiro, Luis M. Liz-Marzán, and F. Javier García de Abajo. Optimization of nanoparticle-based sers substrates through large-scale realistic simulations. *ACS Photonics*, 4(2):329–337, 2017.

[39] Youcef Saad and Martin H. Schultz. Gmres: A generalized minimal residual algorithm for solving nonsymmetric linear systems. *SIAM Journal on Scientific and Statistical Computing*, 7(3):856–869, 1986.

[40] J. M. Song and W. C. Chew. Multilevel fast-multipole algorithm for solving combined field integral equations of electromagnetic scattering. *Microwave and Optical Technology Letters*, 10(1):14–19, 1995.

[41] J. Song, Cai-Cheng Lu, and Weng Cho Chew. Multilevel fast multipole algorithm for electromagnetic scattering by large complex objects. *IEEE Transactions on Antennas and Propagation*, 45(10):1488–1493, 1997.

[42] S. Velamparambil and Weng Cho Chew. Analysis and performance of a distributed memory multilevel fast multipole algorithm. *IEEE Transactions on Antennas and Propagation*, 53(8):2719–2727, 2005.

[43] Xiao-Min Pan and Xin-Qing Sh. A sophisticated parallel mlfma for scattering by extremely large targets [em programmer's notebook]. *IEEE Antennas and Propagation Magazine*, 50(3):129–138, 2008.

[44] Jose Manuel Bertolo Luis Landesa Fernando Obelleiro Jose Taboada, Marta Gomez Araujo and Jose Luis Rodriguez. Mlfma-fft parallel algorithm for the solution of large-scale problems in electromagnetics (invited paper). *Progress In Electromagnetics Research*, 105:15–30, 2010.

[45] Z. Peng, K. H. Lim, and J. F. Lee. Computations of electromagnetic wave scattering from penetrable composite targets using a surface integral equation method with multiple traces. *IEEE Transactions on Antennas and Propagation*, 61(1):256–269, jan 2013.

[46] Kong, Wei-Bin and Zhou, Hou-Xing and Zheng, Kai-Lai and Hong, Wei. Analysis of Multiscale Problems Using the MLFMA With the Assistance of the FFT-Based Method. *IEEE Transactions on Antennas and Propagation*, 63(9):4184–4188, 2015.

[47] Simon B. Adrian, Alexandre Dély, Davide Consoli, Adrien Merlini, and Francesco P. Andriulli. Electromagnetic integral equations: Insights in conditioning and preconditioning. *IEEE Open Journal of Antennas and Propagation*, pages 1–1, 2021.

[48] Zhen Peng, Xiao-Chuan Wang, and Jin-Fa Lee. Integral equation based domain decomposition method for solving electromagnetic wave scattering from non-penetrable objects. *IEEE Transactions on Antennas and Propagation*, 59(9):3328–3338, 2011.

[49] Zhen Peng, Kheng-Hwee Lim, and Jin-Fa Lee. Nonconformal domain decomposition methods for solving large multiscale electromagnetic scattering problems. *Proceedings of the IEEE*, 101(2):298–319, 2013.

[50] Mario A. Echeverri Bautista, Francesca Vipiana, Matteo Alessandro Francavilla, Jorge A. Tobon Vasquez, and Giuseppe Vecchi. A nonconformal domain decomposition scheme for the analysis of multiscale structures. *IEEE Transactions on Antennas and Propagation*, 63(8):3548–3560, 2015.

[51] Diego M. Solís, Fernando Obelleiro, and Jose M. Taboada. Surface integral equation-domain decomposition scheme for solving multiscale nanoparticle assemblies with repetitions. *IEEE Photonics Journal*, 8(5):1–14, 2016.

[52] Lan-Wei Guo, Yongpin Chen, Jun Hu, Ran Zhao, Ming Jiang, Joshua Le-Wei Li, and Zaiping Nie. A novel jmcfie-ddm for analysis of em scattering and radiation by composite objects. *IEEE Antennas and Wireless Propagation Letters*, 16:389–392, 2017.

[53] F. Vipiana, M. A. Francavilla, and G. Vecchi. EFIE modeling of highdefinition multiscale structures. *IEEE Transactions on Antennas and Propagation*, 58(7):2362–2374, jul 2010.

[54] G. Vecchi. Loop-star decomposition of basis functions in the discretization of the efie. *IEEE Transactions on Antennas and Propagation*, 47(2):339–346, 1999.

[55] Jin-Fa Lee, R. Lee, and R.J. Burkholder. Loop star basis functions and a robust preconditioner for efie scattering problems. *IEEE Transactions on Antennas and Propagation*, 51(8):1855–1863, 2003.

[56] Francesco P. Andriulli, Francesca Vipiana, and Giuseppe Vecchi. Hierarchical bases for nonhierarchic 3-d triangular meshes. *IEEE Transactions on Antennas and Propagation*, 56(8):2288–2297, 2008.

[57] Francesco P. Andriulli, Kristof Cools, Hakan Bagci, Femke Olyslager, Annalisa Buffa, Snorre Christiansen, and Eric Michielssen. A multiplicative calderon preconditioner for the electric field integral equation. *IEEE Transactions on Antennas and Propagation*, 56(8):2398–2412, 2008.

[58] H. Contopanagos, B. Dembart, M. Epton, J.J. Ottusch, V. Rokhlin, J.L. Visher, and S.M. Wandzura. Well-conditioned boundary integral equations for three-dimensional electromagnetic scattering. *IEEE Transactions on Antennas and Propagation*, 50(12):1824–1830, 2002.

[59] R.J. Adams. Physical and analytical properties of a stabilized electric field integral equation. *IEEE Transactions on Antennas and Propagation*, 52(2):362–372, 2004.

[60] Matthew B. Stephanson and Jin-Fa Lee. Preconditioned electric field integral equation using calderon identities and dual loop/star basis functions. *IEEE Transactions on Antennas and Propagation*, 57(4):1274–1279, 2009.

[61] Oscar Bruno, Tim Elling, Randy Paffenroth, and Catalin Turc. Electromagnetic integral equations requiring small numbers of krylov-subspace iterations. *Journal of Computational Physics*, 228(17):6169–6183, 2009.

[62] Yousef Saad. *Iterative methods for sparse linear systems.* SIAM, 2003.

[63] Edmond Chow and Yousef Saad. Experimental study of ilu preconditioners for indefinite matrices. *Journal of Computational and Applied Mathematics*, 86(2):387–414, 1997.

[64] Marcus J. Grote and Thomas Huckle. Parallel preconditioning with sparse approximate inverses. *SIAM Journal on Scientific Computing*, 18(3):838–853, 1997.

[65] Mario A Echeverri Bautista, Francesca Vipiana, Matteo Alessandro Francavilla, Jorge A. Tobon Vasquez, and Giuseppe Vecchi. A nonconformal domain decomposition scheme for the analysis of multiscale structures. *IEEE Transactions on Antennas and Propagation*, 63(8):3548–3560, 2015.

[66] Oliver Wiedenmann and Thomas F. Eibert. A domain decomposition method for boundary integral equations using a transmission condition based on the near-zone couplings. *IEEE Transactions on Antennas and Propagation*, 62(8):4105–4114, 2014.

[67] Diego M. Solís, Víctor F. Martín, Marta G. Araújo, David Larios, Fernando Obelleiro, and José M. Taboada. Accurate emc engineering on realistic platforms using an integral equation domain decomposition approach. *IEEE Transactions on Antennas and Propagation*, 68(4):3002–3015, 2020.

[68] Andrew Greenwood Brian MacKie-Mason and Zhen Peng. Adaptive and parallel surface integral equation solvers for very large-scale electromagnetic modeling and simulation (invited paper). *Progress In Electromagnetics Research*, 154:143–162, 2015.

[69] Zhen Peng, Ralf Hiptmair, Yang Shao, and Brian MacKie-Mason. Domain decomposition preconditioning for surface integral equations in solving challenging electromagnetic scattering problems. *IEEE Transactions on Antennas and Propagation*, 64(1):210–223, 2016.

[70] Víctor F. Martín, David Larios, Diego M. Solís, José M. Taboada, Luis Landesa, and Fernando Obelleiro. Tear-and-interconnect domain decomposition scheme for solving multiscale composite penetrable objects. *IEEE Access*, 8:107345–107352, 2020.

[71] Shifeng Huang, Gaobiao Xiao, Yuyang Hu, Rui Liu, and Junfa Mao. Multibranch rao–wilton–glisson basis functions for electromagnetic scattering problems. *IEEE Transactions on Antennas and Propagation*, 69(10):6624–6634, 2021.

[72] P. Ylä-Oijala, M. Taskinen, and S. Järvenpää. Surface integral equation formulations for solving electromagnetic scattering problems with iterative methods. *Radio Science*, 40(6):RS6002, dec 2005.

[73] Diego Martínez Solís, Jose Manuel Taboada, and Fernando Obelleiro Basteiro. Surface Integral Equation-Method of Moments With Multiregion Basis Functions Applied to Plasmonics. *IEEE Transactions on Antennas and Propagation*, 63(5):2141–2152, may 2015.

[74] R. Coifman, V. Rokhlin, and S. Wandzura. The fast multipole method for the wave equation: a pedestrian prescription. *IEEE Antennas and Propagation Magazine*, 35(3):7–12, 1993.

[75] Jose Manuel Taboada, Marta G. Araujo, Fernando Obelleiro Basteiro, Jose Luis Rodriguez, and Luis Landesa. MLFMA-FFT parallel algorithm for the solution of extremely large problems in electromagnetics. *Proceedings of the IEEE*, 101(2):350–363, 2013.

[76] M. G. Araújo, J. M. Taboada, J. Rivero, D. M. Solís, and F. Obelleiro. Solution of large-scale plasmonic problems with the multilevel fast multipole algorithm. *Optics Letters*, 37(3):416, feb 2012.

[77] Bruno Stupfel. A hybrid finite element and integral equation domain decomposition method for the solution of the 3-d scattering problem. *Journal of Computational Physics*, 172(2):451–471, 2001.

[78] Zhen Peng and Jin-Fa Lee. Non-conformal domain decomposition method with second-order transmission conditions for time-harmonic electromagnetics. *Journal of Computational Physics*, 229(16):5615–5629, 2010.

[79] Miodrag S. Tasic and Branko M. Kolundzija. Method of moment weighted domain decomposition method for scattering from large platforms. *IEEE Transactions on Antennas and Propagation*, 66(7):3577–3589, 2018.

[80] Zhen Peng, Kheng-Hwee Lim, and Jin-Fa Lee. Computations of electromagnetic wave scattering from penetrable composite targets using a surface integral equation method with multiple traces. *IEEE Transactions on Antennas and Propagation*, 61(1):256–270, 2013.

[81] B. Stupfel. A fast-domain decomposition method for the solution of electromagnetic scattering by large objects. *IEEE Transactions on Antennas and Propagation*, 44(10):1375–1385, 1996.

[82] Oliver Wiedenmann and Thomas F. Eibert. A domain decomposition method for boundary integral equations using a transmission condition based on the near-zone couplings. *IEEE Transactions on Antennas and Propagation*, 62(8):4105–4114, 2014.

[83] Diego M. Solís, Marta G. Araújo, Santiago García, Fernando Obelleiro, and José M. Taboada. Multilevel fast multipole algorithm for fields. *Journal of Electromagnetic Waves and Applications*, 32(10):1261–1274, 2018.

[84] S.V. Georgakopoulos, C.A. Balanis, and C.R. Birtcher. Cosite interference between wire antennas on helicopter structures and rotor modulation effects: Fdtd versus measurements. *IEEE Transactions on Electromagnetic Compatibility*, 41(3):221–233, 1999.

[85] Xiaochuan Wang, Zhen Peng, Kheng-Hwee Lim, and Jin-Fa Lee. Multisolver domain decomposition method for modeling emc effects of multiple antennas on a large air platform. *IEEE Transactions on Electromagnetic Compatibility*, 54(2):375–388, 2012.

[86] Francesca Vipiana and Giuseppe Vecchi. A novel, symmetrical solenoidal basis for the mom analysis of closed surfaces. *IEEE Transactions on Antennas and Propagation*, 57(4):1294–1299, 2009.

[87] Developer reference for intel math kernel library pardiso - parallel direct sparse solver interface. `https://www.intel.com/content/www/us/en/develop/documentation/onemkl-developer-reference-fortran/top/sparse-solver-routines/onemkl-pardiso-parallel-direct-sparse-solver-iface.html`.

[88] Zhen Peng, Kheng Hwee Lim, and Jin Fa Lee. A discontinuous galerkin surface integral equation method for electromagnetic wave scattering from nonpenetrable targets. *IEEE Transactions on Antennas and Propagation*, 61(7):3617–3628, 2013.

[89] Zhen Peng, Ralf Hiptmair, Yang Shao, and Brian MacKie-Mason. Domain decomposition preconditioning for surface integral equations in solving challenging electromagnetic scattering problems. *IEEE Transactions on Antennas and Propagation*, 64(1):210–223, jan 2016.

[90] Gaobiao Xiao and Yibei Hou. Intuitive formulation of discontinuous galerkin surface integral equations for electromagnetic scattering problems. *IEEE Transactions on Antennas and Propagation*, 65(1):287–294, 2017.

[91] Yongpin Chen, Dongwei Li, Jun Hu, and Jin Fa Lee. A nonconformal surface integral equation for electromagnetic scattering by multiscale conducting objects. *IEEE Journal on Multiscale and Multiphysics Computational Techniques*, 3:225–234, 2018.

[92] Bei Bei Kong and Xin Qing Sheng. A Discontinuous Galerkin Surface Integral Equation Method for Scattering from Multiscale Homogeneous Objects. *IEEE Transactions on Antennas and Propagation*, 66(4):1937–1946, apr 2018.

[93] B. Cockburn, G. E. Karniadakis and C.-W. Shu. Discontinuous Galerkin methods: theory, computation and application. *Springer*, 2000.

[94] J. Hesthaven Warburton and T. Nodal Discontinuous Galerkin Methods. *Springer*, 2008.

[95] J. S. Hesthaven and T. Warburton. High-order accurate methods for time-domain electromagnetics. *CMES - Computer Modeling in Engineering and Sciences*, 5(5):395–407, 2004.

[96] Paul Houston, Ilaria Perugia, and Dominik Schötzau. Energy norm a posteriori error estimation for mixed discontinuous Galerkin approximations of the Maxwell operator. *Computer Methods in Applied Mechanics and Engineering*, 194(2-5 SPEC. ISS.):499–510, feb 2005.

[97] Stephen D. Gedney, John C. Young, Tyler C. Kramer, and J. Alan Roden. A discontinuous Galerkin finite element time-domain method modeling of dispersive

media. *IEEE Transactions on Antennas and Propagation*, 60(4):1969–1977, apr 2012.

[98] Xiao-Wei Huang and Xin-Qing Sheng. A discontinuous galerkin self-dual integral equation method for scattering from ibc objects. *IEEE Transactions on Antennas and Propagation*, 67(7):4708–4717, 2019.

[99] Beibei Kong, Pasi Ylä-Oijala, and Ari Sihvola. A discontinuous Galerkin surface integral equation method for scattering from IBC targets. *International Journal of Numerical Modelling: Electronic Networks, Devices and Fields*, 33(2):1937–1946, 2020.

[100] Eduard Ubeda and Juan M. Rius. Novel monopolar MFIE MoM-discretization for the scattering analysis of small objects. *IEEE Transactions on Antennas and Propagation*, 54(1):50–57, 2006.

[101] E. Ubeda, J. M. Rius, and A. Heldring. Nonconforming discretization of the electric-field integral equation for closed perfectly conducting objects. *IEEE Transactions on Antennas and Propagation*, 62(8):4171–4186, 2014.

[102] Eduard Ubeda, Juan M. Rius, Alex Heldring, and Ivan Sekulic. Volumetric Testing Parallel to the Boundary Surface for a Nonconforming Discretization of the Electric-Field Integral Equation. *IEEE Transactions on Antennas and Propagation*, 63(7):3286–3291, 2015.

[103] E. Ubeda, I. Sekulic, J. M. Rius, and A. Heldring. Tangential-normal surface testing for the nonconforming discretization of the electric-field integral equation. *IEEE Antennas and Wireless Propagation Letters*, 15:1581–1584, 2016.

[104] Ivan Sekulic, Dimitrios C. Tzarouchis, Pasi Ylä-Oijala, Eduard Ubeda, and Juan M. Rius. Enhanced discretization of surface integral equations for resonant scattering analysis of sharp-edged plasmonic nanoparticles. *Physical Review B*, 99(16):165417, 2019.

[105] Ivan Sekulic, Eduard Ubeda, and Juan M. Rius. Versatile and accurate schemes of discretization for the electromagnetic scattering analysis of arbitrarily shaped piecewise homogeneous objects. *Journal of Computational Physics*, 374:478–494, 2018.

[106] S Huang, G Xiao, Y Hu, and R Liu. Loop star functions including multibranch rao-wilton-glisson basis functions. *IEEE Transactions on Antennas and Propagation*, 70(5):3910–3915, 2022.

[107] J. M. Taboada. *Estudio de compatibilidad electromagnética e interferencia en sistemas radiantes a bordo de estructuras complejas.* PhD thesis, University of Vigo, 2001.

[108] Francesca Vipiana, Francesco P. Andriulli, and Giuseppe Vecchi. Two-tier non-simplex grid hierarchic basis for general 3d meshes. *Waves in Random and Complex Media*, 19(1):126–146, 2009.

[109] Francesca Vipiana and Giuseppe Vecchi. A novel, symmetrical solenoidal basis for the mom analysis of closed surfaces. *IEEE Transactions on Antennas and Propagation*, 57(4):1294–1299, 2009.

[110] Johannes Hendrik Cloete and Thomas Sickel. The planar dual-polarized cavity backed sinuous antenna - a design summary. In *2012 IEEE-APS Topical Conference on Antennas and Propagation in Wireless Communications (APWC)*, pages 1169–1172, 2012.

[111] Rohit Sammeta and Dejan S. Filipovic. Improved efficiency lens-loaded cavity-backed transmit sinuous antenna. *IEEE Transactions on Antennas and Propagation*, 62(12):6000–6009, 2014.

[112] R.A. Burberry and Institution of Electrical Engineers. *VHF and UHF Antennas*. IEE electromagnetic waves series. P. Peregrinus, 1992.

[113] W.L. Stutzman and G.A. Thiele. *Antenna Theory and Design*. Antenna Theory and Design. Wiley, 2012.

[114] Dietmar Leugner and Heinz-D. Bruns. Modeling antenna feeds by electric and magnetic current sheets in conjunction with the method of moments. In *2007 2nd International ITG Conference on Antennas*, pages 100–104, 2007.

[115] Jorge A. Tobon Vasquez, Zhen Peng, Jin-Fa Lee, Giuseppe Vecchi, and Francesca Vipiana. Automatic localized nonconformal mesh refinement for surface integral equations. *IEEE Transactions on Antennas and Propagation*, 68(2):967–975, 2020.

[116] Ramón A. Alvarez-Puebla, Ashish Agarwal, Pramit Manna, Bishnu P. Khanal, Paula Aldeanueva-Potel, Enrique Carbó-Argibay, Nicolas Pazos-Pérez, Leonid Vigderman, Eugene R. Zubarev, Nicholas A. Kotov, and Luis M. Liz-Marzán. Gold nanorods 3d-supercrystals as surface enhanced raman scattering spectroscopy substrates for the rapid detection of scrambled prions. *Proceedings of the National Academy of Sciences*, 108(20):8157–8161, 2011.

[117] Cyrille Hamon, Sergey M. Novikov, Leonardo Scarabelli, Diego M. Solís, Thomas Altantzis, Sara Bals, José M. Taboada, Fernando Obelleiro, and Luis M. Liz-Marzán. Collective plasmonic properties in few-layer gold nanorod supercrystals. *ACS Photonics*, 2(10):1482–1488, 2015.

[118] P. B. Johnson and R. W. Christy. Optical constants of the noble metals. *Phys. Rev. B*, 6:4370–4379, Dec 1972.

[119] Ana B. Serrano-Montes, Judith Langer, Malou Henriksen-Lacey, Dorleta Jimenez de Aberasturi, Diego M. Solís, José M. Taboada, Fernando Obelleiro, Kadir Sentosun, Sara Bals, Ahmet Bekdemir, Francesco Stellacci, and Luis M. Liz-Marzán. Gold nanostar-coated polystyrene beads as multifunctional nanoprobes for sers bioimaging. *The Journal of Physical Chemistry C*, 120(37):20860–20868, 2016.

[120] L. Novotny and B. Hecht. *Principles of Nano-Optics.* Cambridge University Press, 2006.

[121] Lukas Novotny and Bert Hecht. *Principles of Nano-Optics.* Cambridge University Press, 2 edition, 2012.

[122] H. Metiu. Surface enhanced spectroscopy. *Progress in Surface Science*, 17(3):153–320, 1984.

[123] Manzano M. F. Landesa L. Solis D. M. Serna, A. and J. M. Taboada. Fast and accurate electromagnetic solutions of finite periodic optical structures. *Optics express*, 25(15):18031–18039, 2017.

[124] Mao-Kun Li and Weng Cho Chew. Wave-field interaction with complex structures using equivalence principle algorithm. *IEEE Transactions on Antennas and Propagation*, 55(1):130–138, 2007.